

TABLE OF CONTENTS

	Page
Chapter 1: Introduction	1
1.1 Motivations for study of WDM	4
1.2 Experimental Generation of WDM	7
1.3 X-ray diagnostics of WDM	10
1.4 Dissertation Outline	19
Chapter 2: Physics of PENELOPE	20
2.1 Types of interactions	20
2.2 Inelastic scattering	25
2.3 Accuracy and useful regimes	30
2.4 Inelastic scattering	33
2.5 Dosimetry	34
Chapter 3: Nonlocal Heat Transport and Improved Target Design for X-ray Heating Studies at X-ray Free Electron Lasers	36
3.1 I. Introduction	37
3.2 II. Methods	40
3.3 III. Results and discussion	42
3.4 IV. Conclusion	45
Chapter 4: A Photometric Study of Energy-Dispersive X-ray Diffraction at a Laser Plasma Facility	52
4.1 I Introduction	53
4.2 II Methods	57
4.3 III Results and discussion	63
4.4 IV. Conclusions	77
4.5 Acknowledgements	77
4.6 References	79

Chapter 5: X-ray Free Electron Laser-Based Studies of WDM	80
5.1 X-ray Free Electron Lasers	80
5.2 HED physics at XFEL facilities	83
5.3 Scientific Directions	84
5.4 Design of an XFEL heating experiment	85
5.5 Experimental Work	86
Chapter 6: Finite-T Charge Transfer in MgO Under Extreme X-ray Heating: A Crystal of Hollow Atoms	94
Chapter 7: A Disposable X-ray Camera Based on Mass Produced CMOS Sensors and Single-Board Computers	95
7.1 Abstract	95
7.2 Introduction	95
7.3 Methods, Results, and Discussion	96
7.4 Conclusions	103
7.5 Acknowledgments	103
7.6 References	103
Chapter 8: A Color X-ray Camera for 2 – 6 keV Using a Mass-Produced CMOS Sensor	106
8.1 Abstract	106
8.2 Introduction	106
8.3 II. Experimental	108
8.4 III. Results and Discussion	110
8.5 IV. Conclusions and Future Directions	116
8.6 References	116
Chapter 9: Real-time analysis tools for the LCLS	117
9.1 Integration of Logging and Analysis	118
9.2 Interactive Distributed Computing	120
9.3 API features	121

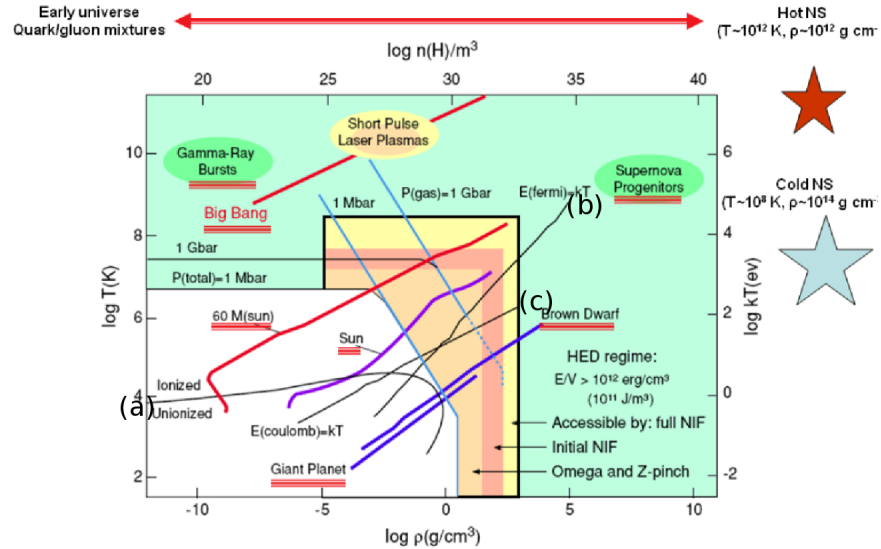
Chapter 1

INTRODUCTION

In this thesis I introduce the development of new techniques for the production of materials in the warm dense matter (WDM) regime, and for interrogation of the structure and thermodynamic state of such systems using x-ray diffraction and (to a lesser extent) spectroscopy. The main results include a scheme for single-shot determination of the static structure factors of WDM systems generated at laser plasma facilities; a technique for enhancing the density of deposited energy in WDM generated at fourth-generation X-ray sources such as the Linac Coherent Light Source (LCLS); and interpretation of experimental data that puts new constraints on the thermalization (both electronic and lattice) of a solid state material upon fs-scale XFEL heating. In addition to this thread of research I discuss some secondary work on the development of software and electronics for energy- and position-sensitive pixel detectors including current applications in the context of soft x-ray laboratory and possible future ones in XFEL, synchrotron, and laser plasma facility-based experiments.

Before proceeding it is useful to define WDM in terms of the microphysical context it occupies. Fig. (which figure) presents a map of thermodynamic parameter space, with the logarithm of density and temperature on the horizontal and vertical axes, respectively. A few bounding curves can be identified. First, ionization occurs at temperatures exceeding approximately 1 eV; this is denoted by curve (a), which forms a boundary between the plasma and condensed matter regimes. Second, curve (b) indicates the boundary at which the Fermi energy is approximately equal to the average thermal energy $k_B T$; i.e. where the electron degeneracy parameter, $E_f/k_B T$ is of order unity. Third, curve (c) corresponds to a value of 1 for the ratio of the Coulomb energy to the thermal to the thermal one, also called the plasma coupling parameter Γ .

Figure 1.1: The atlas of high-energy density physics (cite)



Above curves (a), (b) and (c) is the regime of classical plasma physics where, as a result of the weak interaction between neighboring ions ($\Gamma \ll 1$), collective interactions predominate over binary collisions and quantum statistics can be neglected ($\Lambda \ll 1$) except for the purpose of calculating blackbody spectra. In this regime continuous, classical modeling treatments are widely-used and fully validated (cites). Below curves (a), (b), and (c) is the low-temperature, intermediate-density realm of condensed matter physics, where the established theoretical framework is that of many-body quantum mechanics, wherein the potential landscape is built on the interaction between electrons and ion cores. In this framework finite-temperature effects are incorporated perturbatively. WDM occupies the transitional regime above curve (a) and near the intersection of curves (b) and (c), characterized by partial degeneracy and strong ion-ion coupling (Γ and Λ of order unity). As a result, treatments of plasma physics originating in the classical regime are not applicable to WDM. Solid state physics models similarly fail in the WDM regime due to large, non-perturbative effects of finite temperature on the structure and thermodynamics of WDM (cites).

Modeling of the ionization potential depression (IPD) in a plasma is a case in point of the difficulties that manifest themselves with theoretical treatments of WDM. Adequate descriptions of IPD are given the Debye-Hueckel approximation and ion sphere model, which cover opposite regimes of high temperature and low density, and low density and high temperature, respectively. We here briefly introduce both model, with focus on the assumptions and approximations that they adopt.

The Debye-Hueckel model applies to a weakly-coupled plasma in local thermal equilibrium. It identifies the electrostatic potential in the Poisson equation with the mean field generated by a population of Maxwell-Boltzmann-distributed ions or electrolytes. This results in the Poisson-Boltzmann equation which, when solved, gives the electrostatic potential produced by an arbitrary charge distribution. The condition for validity of the Debye-Hueckel model is for the Thomas-Fermi screening length (also called the Debye length) to be much larger than the mean inter-ion separation. This condition is satisfied at comparable temperatures, but lower densities, than those encompassed by the WDM regime. (check that this is right, and cite)

In the opposite limit, the ion-sphere model describes IPD in a high-density material with $\Gamma > 1$ (in the low-temperature context IPD is more commonly referred to as pressure ionization). The picture offered by the ion-sphere model is that of a plasma with highly-correlated ion positions and therefore no close encounters between ion pairs. Each ion is treated as a sphere whose potential is unaffected by the presence of neighboring ions. (cite Stewart-Pyatt). The sphere radius is $R_0 = (3/4\pi N_i)^{1/3}$, where N_i is ion number density, while the orbital radius of the ion sphere's n th principal energy level is approximately $r_n = (n^2/Z_n)(0.529\text{\AA})$. For the n th bound state to exist it is necessary that $r_n \leq R_0$; thus, IPD manifests itself as a reduction in the number of bound states as a function of the inter-ion distance R_0 . It should be noted that, although the ion-sphere model is a frequently-used heuristic in high-temperature plasmas with near-ambient densities, it is known to be incorrect in the high-density, moderate-temperature ($\Gamma \gg 1$) regime. Neaton et al. have done ab-initio (DFT) simulation of Li—a free electron-like material under ambient conditions—showing

that, contrary to intuitive expectations and the ion-sphere model, it becomes less free-electron like at high densities and additionally loses its common bcc crystal structure. (cite Neaton 1999) Due to overlap of core electrons, the treatment of electronic wavefunctions in this regime is necessarily strongly nonperturbative—again in conflict with the ion-sphere model’s assumptions.

Leaving aside, momentarily, the ion sphere model’s limitations, we might contemplate constructing a model of ionization potential depression that reduces to the ion sphere and Debye-Huekel models in their respective limits. Doing so is challenging because it allows none of the simplifying approximations invoked by the two limiting cases. One manifestation of uncertainty of the correct approach is the existence of two mutually-contradictory models for IPD in WDM, those of Stewart and Pyatt (cite) and Ecker and Kroll (cite). Though the Stewart-Pyatt model is more widely used and has the virtue of reproducing the ion-sphere and Debye-Hueckel behaviors (cite Crowley review article), its validity has been called into question by recent direct XFEL-measurements of IPD in Al heated to 180 eV (cite Cricosta paper). Such conflicts exemplify the persistent difficulty of constructing models with validity accross different sub-regimes of WDM.

1.1 Motivations for study of WDM

In addition to the basic physics questions intrinsic to the WDM regime, there are a number of points of contact between WDM and particular problems in other fields. This interaction has been bolstered in recent years by rapid development of laser plasma facilities and x-ray free electron lasers (XFELs) with unprecedeted experimental capability for producing WDM and probing its physical properties. This has brought many previously-intractable physical regimes into the scope of both empirical investigation and numerical simulation.

1.1.1 Astrophysical modeling

A large contribution to this growth in interest is the relevance of WDM theory as a microphysical basis on for models of various systems in planetary and stellar astrophysics. Here

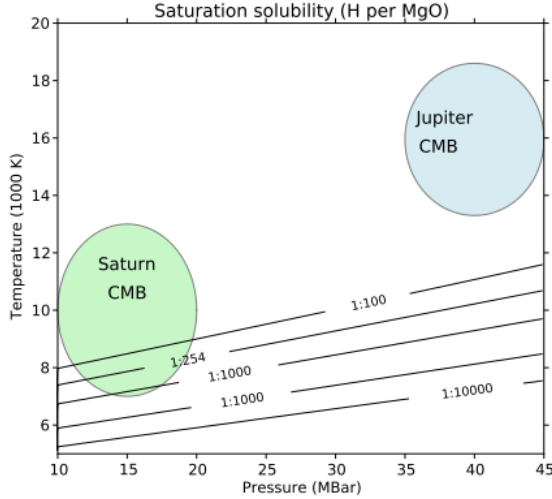
we introduce two examples in which this relationship is salient.

The interiors of both rocky and gas giant planets contain dense, and in some cases Fermi-degenerate, plasmas at 1 eV-scale temperatures. Examples include the iron under conditions of the earth's core (pressure = 3 Mbar; T = 6000 K), whose viscosity and equation of state (EOS) has consequences on convective heat transfer and the formation of earth's magnetic field. (cites) Similarly, modeling of the evolution and structure of gas giant planets depends on the EOS of H under the regime of gas giant interiors. The existence of metallic H caused by pressure ionization at Mbar-scale pressures has been experimentally demonstrated, but its onset is poorly understood at the level of theoretical models for the EOS: although a first-order dielectric-to-metal phase transition has been postulated, current approaches do not attempt to model pressure ionization, instead limiting themselves to interpolation between the better-understood atomic and fully ionized limits. (cites)

The solubility physics of two-component WDM mixtures containing H with other species found in rocky planetary bodies has direct consequences on mass transport across the core-mantle boundary in gas giant planets. It also has crucial importance in the modeling of gas giant formation, where the solubility of H with rocky elements bears on the plausibility of the planetesimal accretion hypothesis for gas giant genesis, which requires condensation of H and He around a rocky core. (cite Wilson MgO solubility paper).

Another case in which the material properties of warm dense matter determine the behavior of an astrophysical object is that of white dwarves, whose envelopes consist of a hot, partially Fermi-degenerate plasma. Modeling the cooling of white dwarves is a topic of interest (cites), especially in the context of the importance of type 1a supernovae as ‘standard candles’ for measuring distances to distant galaxies. Doing so, however, requires knowledge of stellar envelope opacities, equations of state (EOS), and transport properties, many of which properties are currently unknown to within factors of order unity. The absence of understanding of the simplest available system—the hydrogenic one-component plasma—underscores the difficulty of this thread of research.

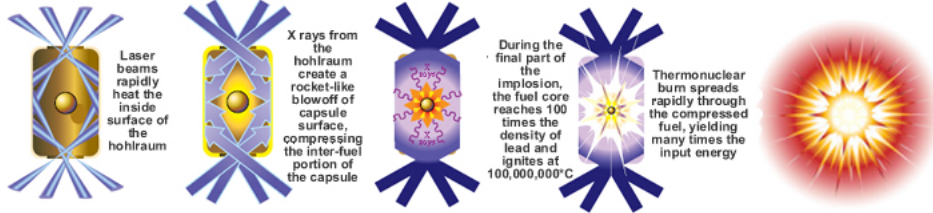
Figure 1.2: Saturation solubility of MgO in H as a function of pressure and temperature from *ab initio* calculation by Wilson et al. The temperature conditions of the core-mantle boundaries of Saturn and Jupiter are indicated. (cite Wilson)



1.1.2 Inertial Confinement Fusion

The effort to reach controlled fusion through implosion of deuterium-tritium fuel capsules—an approach termed inertial confinement fusion—has progressed significantly in the last decade due to completion of laboratory facilities capable of producing HED (definition?) plasmas with densities and temperatures approaching levels needed for ignition. Fig. (which figure) shows a schematic of an ignition technique called indirect drive. In this configuration the ICF target, which consists of a hollow spherical capsule of ablator material filled with deuterium-tritium fuel, is confined in a hollow capsule of a high-Z material (the Hohlraum). A multi-TW, ns-duration duration laser passes through apertures in the Hohlraum and heats the Hohlraum to blackbody temperatures on the order of several hundred eV. The resulting thermal spectrum of soft X rays isotropically heats and ablates the fuel capsule's surface, causing its interior to implode by conservation of momentum. Typical parameters of the plasma created at maximum compression include areal densities (capsule density \times radius) of 0.3 g/cm² and temperatures of the order 10 keV. (cite. see x-games pg 113)

Figure 1.3: Schematic of indirect-drive inertial confinement fusion shot. (cite)



Although its end state falls well within the regime of a classical plasma, the fuel capsule transitions through the WDM state during compression. The opacity and EOS of warm dense matter therefore has a strong influence on the development and propagation of shocks during ablation of the fuel capsule, which in turn affects the optimization of various experimental parameters, including fuel capsule geometry and temporal profile of the laser driver. Accurate modeling of the fuel capsule's transport properties under the WDM regime is equally important for understanding the development during compression of hydrodynamic instabilities, which are known to be a major obstacle to the efficient coupling of laser energy into fuel compression (cites).

1.2 Experimental Generation of WDM

WDM conditions may be generated using X-ray free electron lasers (XFELs) and several varieties of lasers, found both in large-scale facilities and laboratory-scale systems. Here we provide an overview of existing technologies.

1.2.1 Long-pulse lasers

Lasers with pulse durations on the order of nanoseconds and energies of 1 kJ or more are among the most versatile tools for producing high energy density states, including warm dense matter. In the most common use cases of long pulse lasers the target is a bulk material, and coupling of laser energy into it occurs in two stages. First, the laser rapidly (TODO how rapidly) generates a coronal plasma at the material's surface. Once the electron

density of this plasma exceeds the laser wavelength's critical density (TODO: equation) the laser becomes electromagnetically shielded from the material's interior and can no longer transfer energy to it. In the context of direct drive (where the material is a target to which laser energy is directly coupled), subsequent energy transfer occurs by thermal conduction of energy from the surface plasma to higher-density regions as well as by compression of the target resulting from ablation of its surface. In the case of indirect drive, the laser's energy is used to heat a surface (typically the interior of a Hohlraum) that provides a thermal bath which, in turn, couples to the target via its blackbody radiation.

The ns duration of long-pulse lasers matches the timescale on which mechanical and hydrodynamic processes occur on typical target scales. Long-pulse lasers are thus suited to generating ramp and shock compression, notably including for the application of ICF. The largest-scale laser plasma facilities—Omega EP at the Laboratory for Laser Energetics in Rochester, NY and the National Ignition Facility—are long-pulse laser systems targeted toward the ICF program.

1.2.2 Short-pulse lasers

Short pulse lasers are a second class of systems used to generate HED conditions. They are typically defined by pulse durations on the order of a picosecond or less, down to as little as ~ 1 fs.

Short-pulse laser systems arose after the development of chirped pulse amplification in the 1980s (cite) and have proliferated ever since (cites), especially with the recent advent of compact (university laboratory-scale) versions with tens of Joules of pulse energy, sufficient to generate scientifically interesting HED conditions. The largest-scale short pulse lasers have pulse powers up to 100 TW (check this number), with durations between 10 and 100 fs (check this as well).

Due to the smaller total energies of short-pulse lasers and the relatively slow cooling timescale of materials heated above ambient conditions *regardless* of the pump duration, short-pulse lasers are used to generate HED conditions under direct-drive configurations

alone. Energy is coupled into a target indirectly (as is the case with long-pulse systems) via ‘hot’ MeV-scale electrons generated in the laser’s interaction with plasma at the target surface. In the (typical) case where bulk heating is required, the target thickness is small compared to the hot electrons’ stopping range, causing them to reflux through the target once it acquires net positive charge. This process lasts on the order of one ps (check this, cite Nilson and maybe others) and thus sets the time resolution of experiments in which the short-pulse laser is used to both heat and probe the target.

1.2.3 X-Ray Free Electron Lasers

The advent of X-Ray Free Electron lasers is a major advance in capability for WDM research. Existing incarnations of these sources, notably the Linac Coherent Light Source (LCLS), provide 10^{14} photons in a ≥ 10 fs-duration monochromatic pulses with tunable energy. While the energies per pulse are smaller than those attainable with a short-pulse laser, they are largely sufficient to produce HED states with temperatures in excess of 100 eV (cite). Because XFELs can heat volumetrically, they are free of the primary deficiency of lasers with respect to the task of generating dense plasmas: namely, the latter can only heat bulk materials indirectly and over durations of 1 ps or longer, which exceeds the timescale for changes in WDM, preventing the study of short-lived transient states.

The ability to generate (and probe) WDM on truly inertial timescales, wherein atomic nuclei are effectively frozen, has been duly exploited in early pioneering studies at the LCLS. It forms the basis, for example, for a new thread of materials science research on nonthermal lattice and spin dynamics (cite Lee and others). Likely even more significantly, it is the enabling feature for macromolecular crystallography under the ‘diffract before destroy’ paradigm. (cites) The possibilities surrounding rapid generation of WDM is a topic to which I return in (which chapter?). (cite Vinko et al. and other early LCLS papers).

1.3 X-ray diagnostics of WDM

Experimental studies of WDM suffer from a substantial complication: the opacity of WDM to photons is large at energies up to the soft X ray regime. As mentioned in section 1.2.2, in the context of laser heating this is merely a frustration; for the purposes of measuring the conditions of a bulk WDM system, however, the need for direct detection of radiation originating from the target's interior makes optical probes wholly ineffective. Determination of the structure and thermodynamic state variables of a dense plasma therefore requires sufficiently penetrating radiation; for this reason, the large majority of WDM diagnostics are X ray photon-in photon-out measurements.

In the remainder of this section I provide an overview of the various available X-ray techniques.

1.3.1 Scattering

Elastic scattering and nonresonant inelastic X-ray scattering (NIXS) are among the most-frequently probed signals for inferring the structure, temperature and ionization state of WDM. In dense plasmas generated by long-pulse lasers, where LTE is commonly assumed, NIXS also serves as a probe of temperature.

For a given sample, the sum of scattering interactions is characterized by the double-differential scattering cross section (DDCS) $d^2\sigma/d\Omega d\omega$, which describes the probability of a photon to scatter into a solid angle increment $d\Omega$ within an energy loss interval $d\omega$. Within the independent-electron and first Born approximations the DDCS is given by

$$\frac{d^2\sigma}{d\Omega d\omega} = r_0^2 \left(\frac{\omega_2}{\omega_1} \right) |\epsilon_1 \times \epsilon_2^*|^2 S(\vec{q}, \omega), \quad (1.1)$$

where

$$S(\vec{q}, \omega) \equiv \sum_F \sum_j \langle F | \exp(i\vec{q} \cdot \vec{r}_j) | I \rangle |^2 \delta(E_F - E_I - \hbar\omega). \quad (1.2)$$

The first term in equation 1.3.1 is the Thomson cross section, which describes the interaction between a probe photon and a single electron; $S(\vec{q}, \omega)$ is referred to as the dynamic structure factor, and encapsulates all system-specific properties. I and F are initial and final states of the sample with energies E_I and E_F , respectively, and the second summation of 1.3.1 is over electrons in the scatterer.

Following Chihara (cite Chihara), the typical treatment of a dense plasma separates the dynamic structure factor into several components:

$$S(\vec{q}, \omega) = |f_I(q) + f_e(q)|^2 S_{ii}(q, \omega) + S_{ff}(q, \omega) + S_{bf}(q, \omega), \quad (1.3)$$

S_{ii} is the atomic/ionic structure factor, f_I and f_e are the form factors for the ion and a surrounding cloud of screening scharge. S_{ff} contains scattering from free, delocalized electrons, and S_{bf} represents Raman-type bound-free transitions resulting from scattering from tightly-bound core level electrons. Note that spherical symmetry has been assumed: all terms of the structure factor depend only on the magnitude of \vec{q} .

The first term corresponds to elastic ($\omega = 0$) scattering, and is connected to the dense plasma's pair distribution function by a Fourier transform. Though not a component of the NIXS signal, it must often be considered in simulations and analyses of NIXS data, wherein the Bethe sum rule (cite) and other conserved quantities consist of integrals over the entire energy-loss domain of the dynamic structure factor. Elastic scattering is a highly-useful probe of structure; we consider it separately in section 1.3.1.

The free-free contribution to $S(q, \omega)$ can be expressed in terms of the free-electron dielectric function $\epsilon(q, \omega)$ via the fluctuation-dissipation theorem (cite Kubo et al.):

$$S(q, \omega) = \frac{\epsilon_0 \hbar q^2}{\pi e^2 n_e} \frac{1}{1 - e^{\hbar \omega / k_B T_e}} \text{Im} \frac{1}{\epsilon(q, \omega)}, \quad (1.4)$$

The random phase approximation (RPA) (cite Bohm and Pines) is typically used as an approximation for $\epsilon(q, \omega)$, but more recent treatments incorporate a perturbative treatment of electron-ion interactions using the Born-Mermin Approximation (cite Mermin). As shown

in Fig. (which figure?), the scattering contribution of S_{ff} consists of a pair of Plasmon peaks with opposite, equal-magnitude energy offsets from the elastic scattering peak. Electron density is inferred from the magnitude of the Plasmon peak shifts while temperature is obtained from the ratio of intensities of the two peaks, following the principle of detailed balance (cite Glenzer 2007 and Lee 2009).

Although the connection of temperature and density to the free-free component of the dielectric function is well-founded, there are two obstacles to effective interpretation of collective scattering data from WDM systems; one is theoretical and the other experimental. First, the validity of established treatments of the dielectric function has been called into question, with recent plasmon spectrum calculations based on MD-DFT simulations showing a significant change in the plasmon profile compared to that predicted by the BMA. (cite Mattern thesis and Plagemann). Second, the plasmon peak suffers from poor signal to background and has a small separation from the elastic scattering peak under typical WDM electron densities, making it difficult to resolve. As a result only a handful of experiments to date have pursued this technique.

We finally turn our attention to the last term of 1.3.1, S_{bf} , whose contribution to the inelastic DDCS is often referred to as x-ray Thomson scattering (XRTS). Obtaining state variable information from a system's bound-free scattering contribution is dependent on the underlying model of electronic structure used; as a result, various treatments exist, including the Impulse Approximation (IA) of Eisenberger and Platzman, wherein the bound-free contribution to XRTS is equivalent to Doppler-broadened Compton scattering (cite Eisenberger and Platzman); the plane wave form factor approximation (PWFFA) of Schumacher (cite Schumacher), which attempts to extend the IA by incorporating electron binding energies; and calculation of matrix elements using a real space Green's function (RSGF) formalism applied to atomic clusters, as implemented in the atomic spectroscopy code FEFF (cite Mattern).

In current practice, measurement of the bound-free component of XRTS from WDM is performed in the large- q regime, where the Compton feature is broad and can be measured

using high-efficiency (but low-resolution) HOPG-based spectrometers (need cites for this). As such, single-particle bound-free scattering is more readily measured than collective excitation features. Since an early demonstration of the technique by Glenzer et al. (cite Glenzer 2003) it has been frequently implemented at both laser plasma and XFEL facilities (cite figures showing how these experiments are set up). Despite some fruitful outcomes (how so? need examples, cites), the large statistical uncertainties in XRTS spectra—particularly at laser plasma facilities, where single-shot measurements are photon-starved—make the inference of state variables difficult, and dependent on one’s choice of electronic structure model (check that this is right. do predictions heavily depend on the choice of model, or is it just that uncertainties are high, regardless of the choice?). Mattern et al. have demonstrated this concretely by comparing theoretical fits to XRTS data of shock-compressed Be, and argue that the lack of rigorous validation of electronic structure models for WDM models strongly undermines their validity for first-principles measurement of state variables. With this context as motivation, we revisit the topic of WDM thermometry in chapter (reference chapter).

1.3.2 Coherent Scattering

Coherent scattering is the zero-energy loss component of the double differential cross section. The inference of structural information from coherent scattering varies by material; two primary cases present themselves.

First, for amorphous materials, such as hot dense plasmas generated by ramp- or shock-compression and lacking long-range order, the scattering amplitude is isotropic and is characterized by the one-dimensional static structure factor, which is connected by a Fourier transform to the material’s pair correlation function. Inference of the full pair correlation function is in practice frustrated by the difficulty of inverting a limited momentum transfer range-sampling of the structure factor, but even in the most information-limited scenarios a density can nevertheless be recovered from the structure factor’s first correlation peak. Although coherent scattering measurements from dense plasmas have been demonstrated in

the context of long-pulse laser compression experiments, implementation difficulties unique to that environment prevent its adoption as a routine technique. We address these difficulties, and proposed solutions, in chapter (chapter reference). (cite Ma et al).

Second, in materials with long-range crystalline order, as typically found in XFEL-based experiments (whose timescales are shorter than the thermalization rate of electronic and ionic degrees of freedom), the coherent scattering amplitude is given by

$$F(\vec{q}) = \sum_n e^{i\vec{q} \cdot \vec{R}_n} \sum_j f_j(\vec{q}) e^{i\vec{q} \cdot \vec{r}_j}, \quad (1.5)$$

where the first summation is over all lattice vectors \vec{R}_n and the second, referred to as the *unit cell structure factor*, is over positions \vec{r}_j of atoms within the unit cell. By the convolution theorem, the crystal's scattering amplitude in reciprocal space is equal to the product of the lattice and unit cell structure factor. The coherent scattering signal is therefore a discrete sampling of the unit cell structure factor at individual Bragg peaks with momentum transfers corresponding to vectors of the reciprocal lattice.

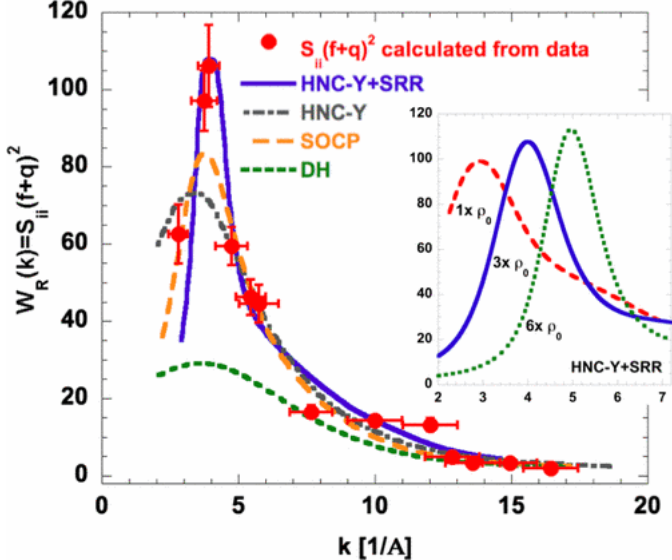
In the context of XRD from a material undergoing thermalization under fs XFEL heating, the crystal scattering amplitude's decomposition into lattice and unit cell components has a direct correspondence to interpretation of structural change. The onset of long-range lattice disorder is readily identifiable as a quenching in Bragg peaks roughly proportional to e^{-q^2} . Evolution of the unit cell structure factor, on the other hand, is dependent on the details of atomic level populations and the material's finite-temperature electronic structure, and can be used as a test of competing theoretical models of both.

(need cites and discussion of the existing literature on XRD of XFEL-heated WDM)

1.3.3 X-ray absorption

X-ray absorption spectroscopy (XAS) may be used to measure the structure and unoccupied electronic density of states of WDM systems. The information available by X-ray absorption near-edge spectroscopy (XANES) and X-ray absorption fine structure (XAES) is the same

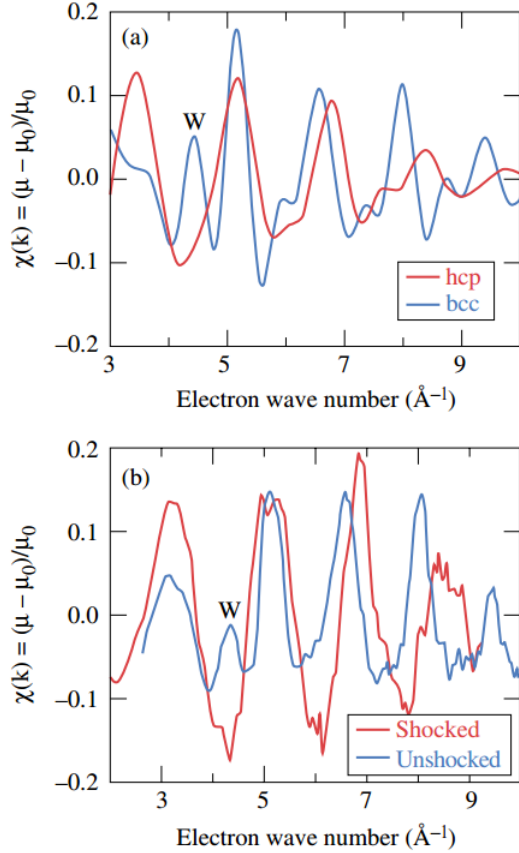
Figure 1.4: Experimental elastic scattering intensity of shock-compressed Al at OMEGA-60, compared to several hypernetted chain (HNC), Debye-Hueckel (DH), and screened one-component plasma (SOCP) models. (cite Ma et al.)



as in other scientific contexts, but the experimental implementation differs in a few respects. In all instances, the short duration of WDM states requires instantaneous collection of absorption spectra using a source with broad-band spectrum. At laser plasma facilities this is arranged using a spherical capsule of CH polymer imploded using a long-pulse laser (cite yaakobi 2003) that emits a thermal spectrum with a $\sqrt{1}$ MeV temperature (check this). This so-called broadband backscatter has been used to collect XAFS for the study of compression-induced phase transitions, such as that from bcc to hcp Fe driven by ns shock-compression (cite Yaakobi 2005).

XANES measurements on dense plasma have also been performed at laser plasma facilities. This requires narrower-band illumination compared with XAFS, which has been achieved using short pulse laser-driven multicomponent X-ray fluorescence backscatter. Levy et al., for example, have used this technique to demonstrate XANES-based thermometry based on measurement of the K-edge slope in Al isochorically heated to 3 eV. (cite Levy et

Figure 1.5: FEFF calculation of XAFS for hcp and bcc phases of Fe (a), compared to experimental data taken on ambient and shock-compressed Fe at the OMEGA laser (b). (cite Yaakobi)

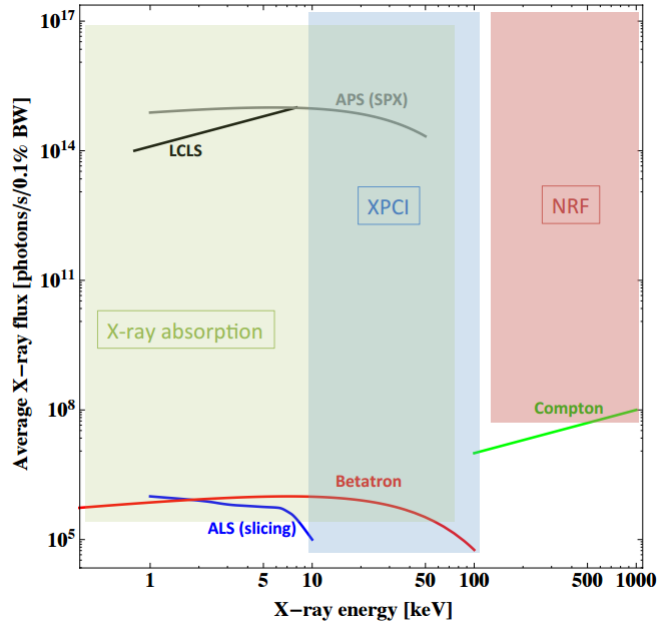


al).

Laser wakefield accelerator X-ray sources generate fs-duration broadband X-ray emission, affording time resolution that surpasses what is possible with laser-driven backscatterers. This makes wakefield accelerators especially well-suited to X-ray absorption spectroscopy of WDM generated at XFEL facilities (cite Albert). The combination of wakefield accelerators with XFELs promises the unprecedented possibility of XFEL pump-probe experiments with simultaneous fs-duration interrogation of the target using broad- and narrow-band hard X-rays. This combination also enables XAS measurements of low-Z materials, which is much

more challenging at laser plasma facilities as a result of the mismatch between the short penetration lengths of x-rays near the K-edges of low-Z species and the relatively large target thicknesses (tens of microns) needed for effective laser ablation.

Figure 1.6: Parameter spaces of several x-ray techniques (X-ray phase contrast imaging (XPCI), x-ray absorption, and nuclear resonance fluorescence (NRF)), overlaid with curves indicating the regions of parameter space accessible by various x-ray source technologies and individual facilities (cite Albert).

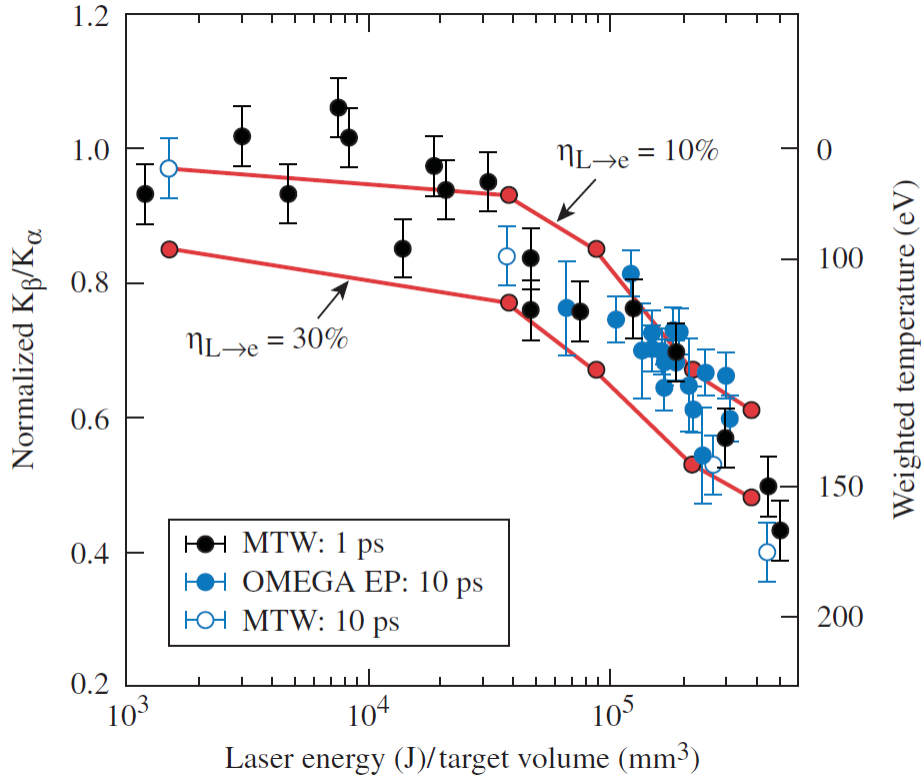


1.3.4 X-ray Emission and X-ray Fluorescence

X-ray fluorescence spectroscopy (XRF) is an extensively used probe in experiments studying the interaction of high-intensity lasers with solid targets. In short-pulse laser experiments involving mid-Z elements heated to temperatures comparable to or larger than M-shell binding energies the ratio of K_β to K_α emission is used as a measurement of temperature. Modeling the coupling efficiency between high-power laser and electrons in a solid-density target is of considerable significance to the effort to understand optical radiation-matter interactions

at high laser intensities ($> 10^{19} \text{ W/cm}^2$); in this context, inference of target heating using K_β/K_α branching ratios provides a useful consistency check in the application of models to experimental data. (cite Myatt et all 2007, Nilson).

Figure 1.7: Experimental K_α/K_β ratios of emission from Cu foil heated by short-pulse lasers, with inferred electron temperature on the right vertical axis. Model calculations are heating for hot electron coupling efficiencies η_e equal to 10% and 30% (cite Nilson)



X-ray emission spectroscopy (XES), the finer-grained cousin of XRF, provides more detailed information on the occupied density of states in a material and can be sensitive to valence-level excitations in the ‘tepid’ transitional regime between ambient and warm dense matter states (reference XES figure from the LD67, maybe get some cites). It has seen use primarily at XFEL facilities, where higher shot rates and probe intensities make the collection of datasets with satisfactory statistical quality easier. (cite photosystem 2 XES

papers). The advent of XFELs as the first high-intensity, monochromatic, and tunable WDM probes has also enabled resonant inelastic X-ray scattering (RIXS) measurements, which has made possible the direct measurement of ionization potential depression on a fs timescale, as demonstrated by Vinko et al. (cite Vinko, Cricosta.).

1.4 *Dissertation Outline*

The overarching theme in this thesis is the relationship, and frequent feedback, between scientific discovery and the development of new experimental technique. To begin, in chapter 2 I introduce a scheme for single-shot measurement of the static structure factors of disordered dense plasmas produced at large-scale laser facilities such as Omega and NIF. In Chapter 3 I present an experimental observation of nonlocal heat transport by keV-scale electrons in a nanophase material and consider the question of how this effect can be used to improve WDM experiments conducted at XFELs via optimized nanostructured target design. In chapter 4 I discuss experimental results of a recent experiment at the LCLS in which we established bounds on the timescales for thermalization of the lattice in XFEL-heated metal oxides and measured the consequences of XFEL heating on electronic charge density, with subsequent comparisons to different model predictions. In chapter 5 I describe an instrument-development effort toward a disposable CMOS-based X-ray camera for use in experimental environments hostile to electronics, particularly laser plasma facilities. Finally, in chapter 6 I introduce UW-XAP, a software tool for streamlined realtime data collection and analysis at the LCLS.

Chapter 2

PHYSICS OF PENELOPE

This chapter serves as background material for Chapter 3, in which we present the use of the Monte Carlo Code PENELOPE for the simulation of electron transport in nanostructured XFEL targets.

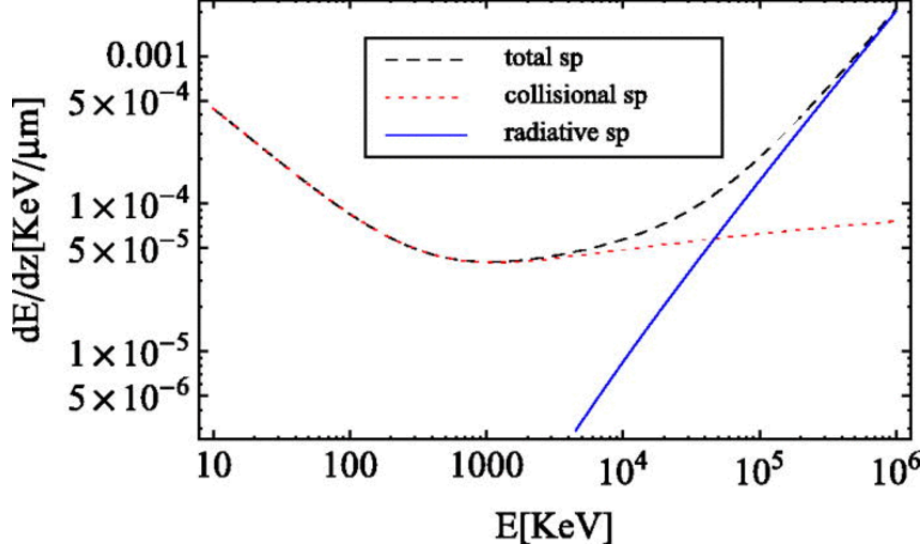
PENELOPE performs Monte Carlo simulations of coupled electron-photon transport in arbitrary materials in the energy range of 100 eV to 1 GeV. It uses a mixed simulation method that treats soft interactions (that is, those involving small angular deflections) with a multiple-scattering approach while individually simulating hard interactions. It is paired with a geometry-definition program, PENGEO, that allows defining samples with volumes of different material composition separated by arbitrary quartic surfaces.

2.1 Types of interactions

In this section we consider the interactions that must be simulated to accurately model the spatial distribution of energy in a nanostructured target material heated by x-ray photons with energy on the order of 10 keV. PENELOPE simulates the following interactions: electron scattering (elastic and inelastic), Bremsstrahlung emission, photon scattering (both elastic (Rayleigh) and inelastic (Compton)), photoelectric absorption and Auger emission, x-ray fluorescence, and pair production and annihilation. Figs. 2.1 and 2.2 show the energy dependence of the relative strengths of the above electron and photon interactions, respectively. Several of the processes have negligible or nonexistent roles on the < 10 keV energy scale considered in the current work, allowing us to limit our scope to the electron scattering and photoabsorption (with consequent fluorescence and Auger emission).

In what follows we introduce the physics of photoabsorption and elastic and inelastic scat-

Figure 2.1: Collisional and radiative electron stopping powers as a function of energy (cite)

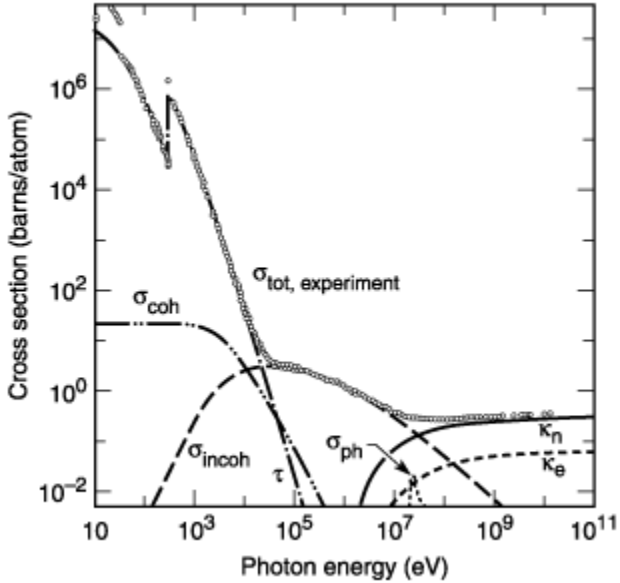


tering with attention to each process's contribution to the spatial distribution of deposited energy in a relaxation cascade beginning with photoionization by a hard x-ray photon. We discuss standard modeling approaches relevant to the 100 eV-10 keV regime, with a focus on the aspects of PENELOPE's treatments most relevant to our regime of interest.

2.1.1 *Fluorescence*

Fig 2.3 illustrates the photoionization of inner atomic shells and introduces the notation used to describe atomic energy levels and transitions between them. Both the photoelectric effect and secondary (Auger) emission resulting from high-energy atomic excitations can be accurately modeled using established treatments that combine theoretical calculation of atomic states via self-consistent modeling (cite Pratt et al. 1973) with experimental data. Associated quantities are compiled in existing public databases; PENELOPE uses tabulated ionization energies from Carlson (cite Carlson et al.) and photoelectric cross sections from the LLNL Evaluated Photon Data Library (EPDL). The EPDL additionally provides emission probabilities for fluorescence photons and Auger electrons in the relaxation of ionized atoms

Figure 2.2: Photon cross section components in C as a function of energy (cite LCL and Hubbell 1980)



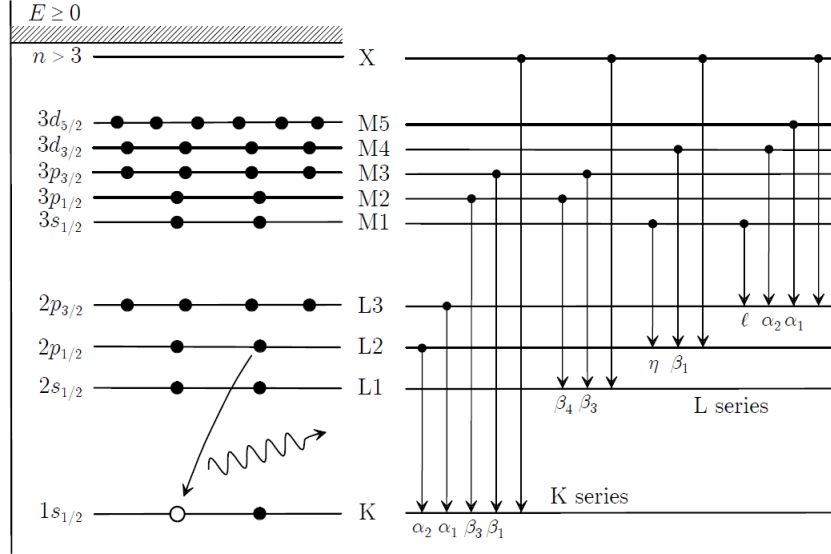
to the ground state.

Assumptions

The above data sources are known to be accurate to the 1% level above 1 keV, under the condition (assumed by PENELOPE) of low incident photon densities, such that only single-electron transitions occur (cite PENELOPE manual).

PENELOPE assumes that incident photons are unpolarized and consequently fails to reproduce the polarization-dependent angular distribution of emitted electrons. We note that it does incorporate the angular distribution from Sauter's (cite sauter 1931) treatment of relativistic photoelectron emission—which, however, reduces to isotropic emission in the nonrelativistic regime covered here.

Figure 2.3: Atomic energy levels of the first three principal quantum numbers (left) and corresponding allowed radiative transitions (right).



2.1.2 Elastic scattering

Elastic scattering of electrons refers to interactions that do not alter target atoms' states.

The simplest widely-used model for elastic scattering of electrons in a solid is the semi-classical approach of Wentzel and Lenz (cite Egerton p. 114), known as the Lenz model, which uses the Yukawa potential for the interaction between a fast electron and a target atom:

$$V(r) = \alpha^2 \frac{e^{-r/r_0}}{r} \quad (2.1)$$

The first Born approximation gives the amplitude for a particle's scattering off of a spherically symmetric potential as

$$f(\theta) \simeq -2 \frac{m}{\hbar^2 q} \int_0^\infty r V(r) \sin(qr) dr \quad (2.2)$$

Substituting (2.1) into (2.2) yields

$$f(\theta) \simeq -2 \frac{m\alpha^2}{\hbar^2 q} \int_0^\infty e^{-r/r_0} \sin(qr) dr = -\frac{2m\alpha^2}{\hbar^2(r_0^{-2} + q^2)}, \quad (2.3)$$

therefore giving the following differential scattering cross section:

$$\frac{d\sigma}{d\Omega} = |f(\theta)| = \frac{4Z^2}{a_0^2 k_0^4} \frac{1}{(\theta^2 + \theta_0^2)^2},$$

where $k_0 = m_0 v$ is the momentum of the incident electron, $\theta_0 = (k_0 r_0)^{-1}$ is the characteristic angle for elastic scattering and $a_0 = 4\pi\epsilon_0\hbar^2/m_0 e^2$ is the Bohr radius.

Using the Thomas-Fermi model, Wentzel and Lenz obtain $r_0 = a_0 Z^{-1/3}$ (cites). Doing this substitution and integrating over scattering angles gives

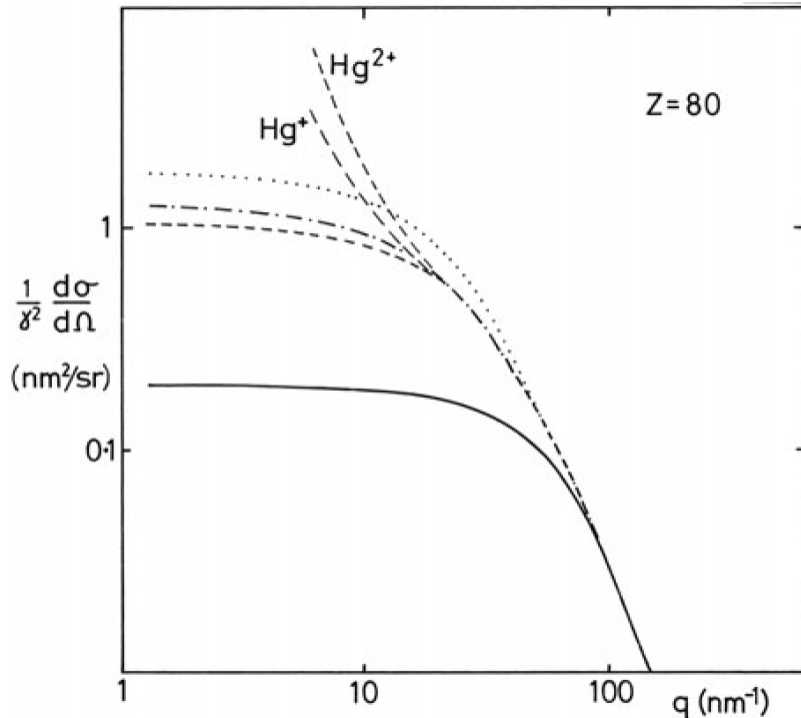
$$\sigma_e = \int_0^\pi \frac{d\sigma}{d\Omega} 2\pi \sin\theta d\theta = \frac{4\pi}{k_0^2} Z^{4/3} \quad (2.4)$$

We thus see that the angular deflections of elastic scattering decrease with increasing energy. For 10 keV electrons, $\theta_0 \simeq 0.1$ rad and $\sigma_e = 4.2 \times 10^{-20} \text{ m}^2$. The elastic mean free path, an alternate measure of the collision frequency, is equal to $\lambda_e = 1/(\sigma_e n)$, where n is atomic number density. As an example, inserting $\sigma_e = 39 \text{ \AA}^2$ and $n = 8.5 \times 10^{25}/\text{m}^3$ for Fe yields $\lambda_e = 300 \text{ \AA}$. The product of expected numbers of elastic collisions on typical transport length scales (whose values exceed 10 nm) and the characteristic scattering angle are therefore at least of order unity (in radians), demonstrating that elastic scattering has a substantial influence on the propagation of below-10 keV electrons.

Despite its simplicity, the Lenz model gives total cross sections to within 10 % for light elements (cite Geiger 1964). For heavier species it underestimates the small-angle differential cross section (Fig. 2.4) but correctly reproduces the large-angle DCS.

More accurate approaches use iterative (e.g. Hartree-Fock) solutions to the Schroedinger or Dirac equations to solve for the atomic potential. (cite Rez 1984 or Starostin). Additionally, partial wave approaches can be used to avoid the Born approximation in regimes for which it fails (low electron energy and high-Z species). PENELOPE combines the above techniques: it solves the partial-wave expanded Dirac equation with a potential based on the

Figure 2.4: Angular dependence of elastic DCS of 30 keV electrons from a Hg atom under the Lenz model using the Wentzel potential (solid), and based on Hartree-Fock (dotted), Hartree-Slater (dot-dashed) and Dirac-Slater (dashed) wavefunctions. ([Reference1](#))



Dirac-Fock electron density of Desclaux (1975, see citation on pg 102 of penelope manual) and exchange interaction of Furness and McCarthy (1973). We will elaborate on PENELOPE's modeling of elastic scattering only within the narrow concern of assessing its accuracy within the physical regimes that we simulate; for more detail the reader may refer to Chapter 3 of the PENELOPE manual.

2.2 Inelastic scattering

We now discuss the treatment of inelastic collisions, which are the dominant mechanism for energy loss of electrons up to above 10 keV (Fig. 2.2). In an atomic system, the differential cross section for a transition from initial state wavefunction ψ_0 to final state wavefunction

ψ_n is

$$\frac{d\sigma_n}{d\Omega} = \frac{m_0}{2\pi\hbar^2} \frac{k_1^2}{k_0} \left| \int V(r) \psi_0 \psi_n \exp(iqr) d\tau \right|^2 \quad (2.5)$$

where \mathbf{k}_0 and \mathbf{k}_1 are the wave vectors of the incident electron before and after scattering and $q = \hbar(\mathbf{k}_1 - \mathbf{k}_0)$ is the corresponding momentum transfer.

At nonrelativistic velocities the potential between electron and atom may be expressed as the following sum of Coulomb potentials of the nucleus and atomic electrons:

$$V(r) = \frac{Ze^2}{4\pi\epsilon_0 r} - \frac{1}{4\pi\epsilon_0} \sum_{j=1}^Z \frac{e^2}{|\mathbf{r} - \mathbf{r}_j|} \quad (2.6)$$

Substituting the second term of equation 2.6 into 2.5, we note that the nuclear potential is independent of the coordinates of the atomic electrons and can therefore be removed from the integral. The orthogonality of the wave functions ψ_n implies that the nuclear potential does not contribute to inelastic scattering; the expression for the differential cross section of inelastic scattering is therefore:

$$\frac{d\sigma_n}{d\Omega} = \left(\frac{4}{a_0^2 q^4} \right) \frac{k_1^2}{k_0} |\epsilon(q)|^2, \quad (2.7)$$

where

$$\epsilon_n = \int \psi_n \sum_j e^{iqr_j} \psi_0 d\tau. \quad (2.8)$$

The generalized oscillator strength is an important related quantity:

$$f_n(q) = \frac{E_n}{R} \frac{|\epsilon_n(q)|^2}{(qa_0)^2}, \quad (2.9)$$

where $R = (m_0 e^4 / 2)(4\pi\epsilon_0\hbar)^{-2}$, the Rydberg energy, and E_n is the energy change of the transition.

The GOS is in general continuous and therefore better expressed as a density with dimensions 1/energy, i.e. $df(q, E)/dE$. This allows us to re-express the double-differential cross

section of inelastic scattering as follows:

$$\frac{d^2\sigma}{d\Omega dE} = 4REq^2 \frac{k_1}{k_0} \frac{df}{dE}(q, E). \quad (2.10)$$

2.2.1 Dielectric function

While this formulation makes it possible to calculate the GOS and associated quantities starting from atomic models, in solid state systems the scattering cross section of outer-shell electrons is influenced by collective effects and chemical bonding. It's therefore preferable to describe the inelastic scattering of an electron from a solid using the solid's dielectric response function, $\epsilon(q, E)$.

Ritchie (cite Ritche 1957) showed, using Poisson's equation and fourier transforms, that an electron moving in the z-direction in an infinite medium experiences a force of the following magnitude opposite its direction of motion:

$$\frac{dE}{dz} = \frac{2\hbar^2}{\pi a_0 m_0 v^2} \int \int \frac{q_y \omega Im[-1/\epsilon(q, \omega)]}{q_y^2 + (\omega/v)^2}, \quad (2.11)$$

where q_y is the component of the momentum transfer vector perpendicular to v and $\omega = E/\hbar$ is an angular frequency. This quantity is referred to as the stopping power. It can be expressed in terms of the previously-defined DDCS:

$$\frac{dE}{dz} = \int \int nE \frac{d^2\sigma}{d\Omega dE} d\Omega dE, \quad (2.12)$$

where E is energy loss and Ω is solid angle. By equating equations 2.11 and 2.12 in the small-angle limit it can be shown, by comparison with the atomic treatment (cite), that

$$\frac{df}{dE}(q, E) = \frac{2E}{\pi E_a^2} Im\left[\frac{-1}{\epsilon(q, E)}\right],$$

thus demonstrating the equivalence of the atomic and dielectric approaches.

Note, finally, that the GOS fully determines the the value of equation 2.10 within the first Born approximation. As such, given the potential of equation 2.5 all modeling of the inelastic

scattering of electrons at intermediate energies (1 keV - 300 keV) reduces to construction of a GOS model.

2.2.2 Modeling the generalized oscillator strength

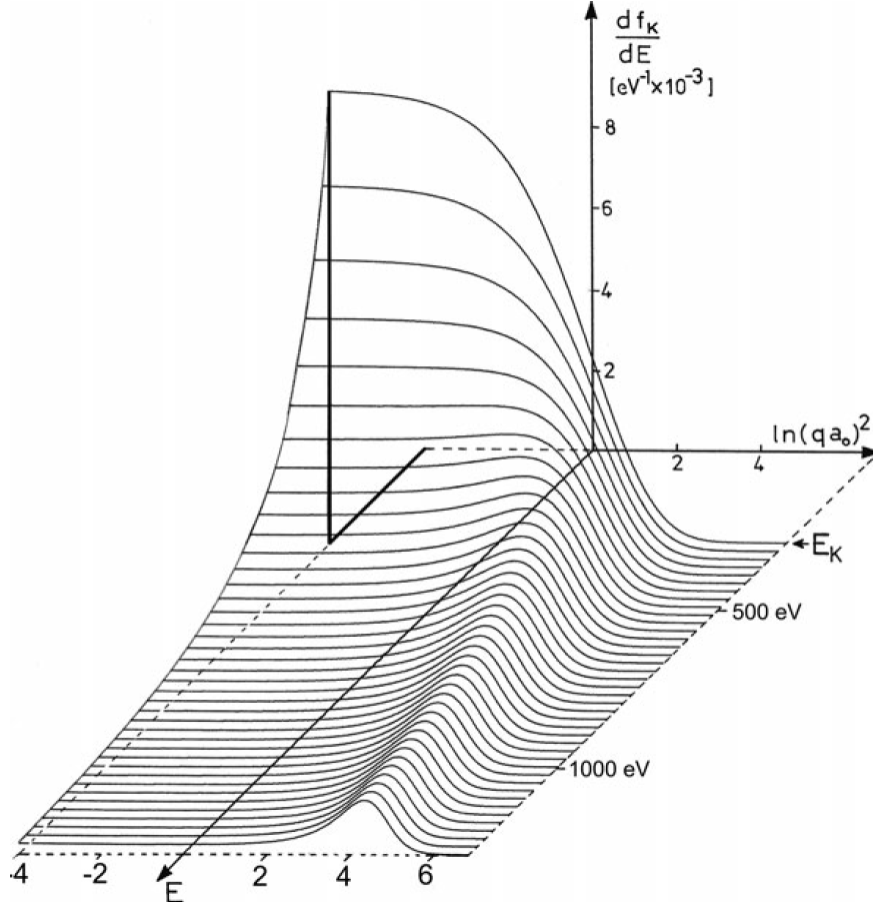
Analytical expressions for the GOS are known for only the two simple cases of the free electron gas and hydrogen atom. In practice, however, it has been shown that the physics of inelastic scattering is mostly determined by a few global features of the GOS (cite Salvat and Fernandez-Varea, 1992) and that relatively simple models are therefore adequate in most situations.

The GOS is conventionally represented as a two-dimensional surface plot called the Bethe surface (Fig. 2.5). We identify two constraints on the behavior of the Bethe surface which any GOS model must reproduce. First, in the limit $Q \rightarrow 0$, the GOS of the dielectric formulation becomes proportional to the optical oscillator strength $\text{Im}[-1/\epsilon(0, E)]$, which is experimentally constrained by x-ray emission measurements. Second, in the limit of large momentum transfer the most probable energy loss is equal to the kinematically-determined value for collision between two free electrons, $E = q^2/2$. (cite Sorini). The corresponding trace in energy and momentum is a feature of the Bethe surface known as the Bethe ridge.

As in Compton scattering, the shape of cuts through the Bethe surface (i.e. spectra of scattered intensity as a function of energy at fixed momentum transfer) is determined by the momentum distribution of atomic electrons. Certain models, such as that of Sorini et al (cite sorini 2006), derive a value for the width of the Bethe ridge from Fermi velocity calculations. PENELOPE adopts a simpler form based on the ‘ δ -oscillator’ model of Liljequist (cite Liljequist 1983) which splits the GOS into contributions from generalized ‘shells’ (each corresponding to either an atomic shell or a collective excitation). The total GOS under this model is a sum over indices k of the shells:

$$\frac{df(q, E)}{dE} = \sum f_k [\delta(E - E_k)\Theta(q_k - q) + \delta(E - q)\Theta(q - q_k)],$$

Figure 2.5: Bethe surface for ionization of the K shell in C, based on a hydrogenic GOS model. (cite Egerton 1979)



where for the k th shell f_k is the shell's number of electrons, q_k is the cutoff recoil energy, and E_k is the shell's resonance energy. Q_k is equal to the shell's binding energy U_k (excluding the conduction band, for which it is set to 0), and E_k is computed from U_k and the material's mean electron density, following Sternheimer (cite Sternheimer 1952). Within this model the GOS is fully determined by the shells' occupations and cutoff (binding) energies U_k , which PENELOPE obtains from Carlson (cite Carlson 1975). It is possible, optionally, to direct PENELOPE to fit its GOS model to experimental stopping power data provided in material input files. It performs this fit through reweighting of the GOS model's oscillators .

Substantial additional detail on the construction and interpretation of PENELOPE's GOS model can be found in its manual.

2.3 Accuracy and useful regimes

In the context of simulation of nanostructured materials, errors in PENELOPE's DCSs for electron scattering originate from both (1) the limited range of validity of PENELOPE's physical models with respect to the bulk properties PENELOPE seeks to reproduce, and (2) the difference between scattering DCSs of ambient-condition bulk materials on the one hand and high-temperature nanostructured materials on the other. We address these two issues in combination.

As mentioned previously, a material's inelastic scattering DCS is fully determined by its loss function, the imaginary component of the dielectric function. Any difference between the responses of bulk and nanophases arises from the contribution to the loss function of collective electronic excitations, i.e. plasmons. Plasmon modes in nanostructured materials form a large research topic on their own (find and cite review article on surface plasmons in nano-materials), but there has been little (no?) (cites) prior work in the context of high-temperature dense matter. The study of heated nanophase materials thus manifests itself as both a problem and an opportunity. On the one hand, the lack of experimental data and accurate modeling makes it impossible to fully quantify the inaccuracy of simulations of ambient, bulk materials. On the other hand, XFEL heating experiments could be used to discriminate between computed dielectric response functions and their underlying finite-temperature electronic strucure theory—to the extent that alternative models generate experimentally measureable differences in inelastic DDCSs. We thus suggest that XFEL heating of nanostrucured materials could enable a joint modeling/experimental program to validate WDM electronic structure theory.

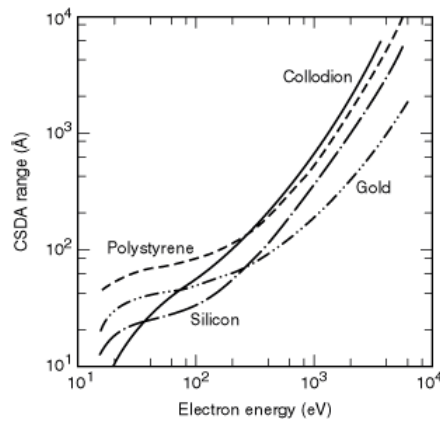
2.3.1 Low-energy loss DCS

In the current situation, wherein the plasmon contribution to the loss function is not known, we can take advantage of the fact that plasmon resonance are confined to energy losses smaller than approximately 100 eV. The influence of the low-energy region of the loss function on the spatial distribution of deposited energy can therefore be bounded using the continuous slowing down approximation (CSDA) of 100 eV electrons. The CSDA for electrons of energy E_0 is the following integral over stopping power:

$$l_{CSDA} = \int_{E_{final}}^{E_0} \left(\frac{dE}{dz} \right)^{-1},$$

where E_{final} , the final energy of the electron, is usually taken to be 10 eV. For elements heavier than boron, $l_{CSDA} < 10$ nm for $E = 100$ eV. We therefore conclude that inaccuracy in treatments of collective excitations affect the spatial distribution of energy deposited by electrons on a length scale below 10 nm (Fig. 2.6)

Figure 2.6: CSDA range as a function of energy for several materials, based on stopping powers of..... (cite)



2.3.2 Energy cutoffs

PENELOPE stops simulation of an electron's motion once its energy drops below a prescribed cutoff value; at the endpoint of an electron's simulated track all of the electron's final energy is deposited at its final position. The resulting distortion in the spatial distribution of deposited energy can be bounded, as above, using the CSDA. PENELOPE's cutoff energy can be set as low as 50 eV. Assuming this value is chosen, the resulting error is much smaller than the bound from section 2.3.1 on the error attributed to inaccuracy in the low-energy dielectric function. Simulation error due to PENELOPE's energy cutoff can therefore be safely neglected.

2.3.3 Elastic scattering

PENELOPE's use of the static field approximation in its elastic scattering model introduces a low-energy error in the DCS due to the effect of the polarizability of atomic charge (cite Salvat 2003). The size of this error is 20% at 1 keV and 50% at 100 eV (PENELOPE manual, pg. 102). The CSDA range at 1 keV, where uncertainty at the DCS level is considerable, ranges from 10 nm for high-Z elements to over 100 nm for low-Z ones. Because the results of the PENELOPE simulations discussed in chapter (which chapter?) are sensitive to errors on the 10 nm - 100 nm length scale, the CSDA does not usefully constrain the elastic DCS model's contribution to uncertainty in the spatial distribution of deposited energy.

A crude estimate taking into account the magnitude of uncertainty in the elastic DCS may be obtained by considering elastic scattering of an electron as a correlated random walk. Given a mean free path λ_e and characteristic scattering angle θ_0 , the number of steps after which the electron's direction of motion becomes uncorrelated with its initial direction is of the order $n = \pi/\theta_0\lambda_e$. The number of elastic scattering events an electron experiences as it slows from an energy of 1 keV to 100 eV (the previously-established-but arbitrary-cutoff below which the treatment of section 2.3.1 applies) is

sketch: basically I have to calculate the number of scattering events, and associated

dephasing of the electron's direction, for several ‘bins’ of energy between 100 eV and 1 keV. For each bin we calculate the equivalent number of steps under an uncorrelated random walk. This yields an expected displacement proportional to the square root of the number of steps in the uncorrelated random walk, which we can multiply by the elastic DCS uncertainty in order to get an associated displacement uncertainty. All displacement uncertainties can then be added in quadrature, yielding a final uncertainty.

2.4 Inelastic scattering

Inelastic scattering has much smaller characteristic angles than elastic scattering scattering but comparable total cross sections. As a result the influence of angular deflections by inelastic scattering on the propagation of electrons is relatively small. The effect of uncertainties in the inelastic scattering DDCS can thus be neglected, and we confine our attention to uncertainty at the level of the stopping power, a more coarse-grained quantity.

Fig 2.7 compares PENELOPE’s computed stopping powers and inelastic mean free paths (for what???) to several experimental datasets. The level of disagreement between different datasets is of the order 2 in the 1 keV - 10 keV energy loss range; the discrepancy between PENELOPE’s modeled stopping power and the experimental datasets is also of this order. Because all transport lengths are proportional to stopping power we must thus contend with a factor of 2 uncertainty in the length scale of computed spatial distributions—far larger than any of the other uncertainties we have considered until now.

The conclusions of chapter (WHICH CHAPTER?) can nevertheless be conserved, with one modification, if we consider PENELOPE’s error in modeling the 1 - 10 keV stopping power as an unknown constant-factor scaling in stopping power. Such an uncertainty corresponds to an unknown scaling of both (1) the length scale of spatial distributions of deposited energy and (2) the flux magnitude of nonlocally-transported energy crossing a given material interface. To give a simple illustration, consider a one-dimensional configuration consisting of an infinite extent of source material from $x = -\infty$ to $x = \infty$. When the sample receives x ray illumination of magnitude unity at position x_0 the density distribution $\rho(x)$ of deposited

energy is given by a response function $f(x)$ (fully determined by the sample material's stopping power and incident x-ray spectrum): $\rho(x) = f(x - x_0)$. If the material is uniformly illuminated by x rays in the region spanning $x = 0$ to $x = \infty$ then (in arbitrary units):

$$\rho(x) = \int_0^\infty f(x - x')dx'.$$

Under the substitution $f(x) \rightarrow g(x) = f(cx)$ (equivalent to scaling $dE/dz \rightarrow (1/c)dE/dz$ of the stopping power), and maintaining normalization of the response function, the distribution becomes:

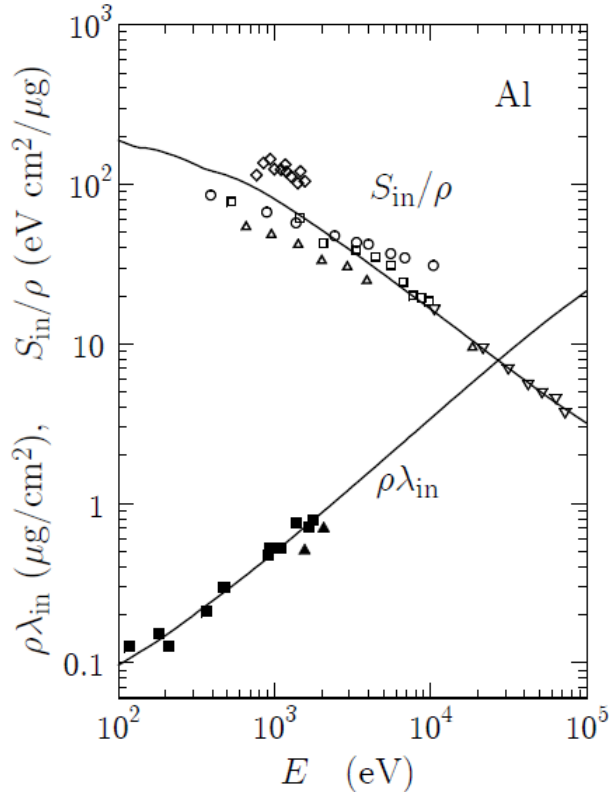
$$\rho'(x) = \int_0^\infty cf((c(x - x')))dx = \int_{cx}^\infty f((u))u.$$

Therefore constant-factor scaling of the stopping power is equivalent to a change in units of length, implying that, under our assumed form of the uncertainty in dE/dz , and adding the assumption that the unknown scaling factor c is equal for all materials, the simulated spatial distributions of deposited energy density are correct up to a uniform scaling of the sample geometry.

2.5 Dosimetry

PENELOPE's dosimetry includes both linear energy transfer from radiation to matter and the contribution of particle track ends, as mentioned in section 2.3.2. At the energy scales of interest the former contribution may be neglected, and the distribution of energy deposited by a particle shower is entirely dependent on simulated inelastic scattering events. PENELOPE's dosimetry calculation is tied to the termination of electron tracks: when an electron's energy drops below the (previously-defined) cutoff value its simulation ceases, and its entire energy is deposited at the track's endpoint. Similarly, the energy loss of soft inelastic collisions (ones having energy loss greater than the cutoff energy W_{cc}) is deposited locally (whereas hard inelastic collisions generate secondary electrons that are individually tracked).

Figure 2.7: Stopping power and inelastic mean free path for electrons as a function of energy in Al..... (cite)



Coarse-graining of the dose distribution is done by dividing the simulation volume into a three-dimensional grid of cells, in each of which PENELOPE calculates the total dose of deposited energy. This grid is defined by the parameters GRIDX, GRIDY, GRIZ and GRIDBN in PENELOPE's input.

Chapter 3

NONLOCAL HEAT TRANSPORT AND IMPROVED TARGET DESIGN FOR X-RAY HEATING STUDIES AT X-RAY FREE ELECTRON LASERS

Oliver Hoidn and Gerald T. Seidler^(*)

Physics Department, University of Washington, Seattle WA

(*) seidler@uw.edu

The extremely high power densities and short durations of single pulses of x-ray free electron lasers (XFELs) have opened new opportunities in atomic physics, where complex excitation-relaxation chains allow for high ionization states in atomic and molecular systems, and in dense plasma physics, where XFEL heating of solid-density targets can create unique dense states of matter having temperatures on the order of the Fermi energy. We focus here on the latter phenomena, with special emphasis on the problem of optimum target design to achieve high x-ray heating into the warm dense matter (WDM) state. We report fully three-dimensional simulations of the incident x-ray pulse and the resulting multielectron relaxation cascade to model the spatial energy density deposition in multicomponent targets, with particular focus on the effects of nonlocal heat transport due to the motion of high energy photoelectrons and Auger electrons. We find that nanoscale high-Z/low-Z multicomponent targets can give much improved energy density deposition in lower-Z materials, with enhancements reaching a factor of 100. This has three important benefits. First, it greatly enlarges the thermodynamic parameter space in XFEL x-ray heating studies of lower-Z materials. Second, it allows the use of higher probe photon energies, enabling higher-information content X-ray diffraction (XRD) measurements such as in two-color XFEL operations. Third, while this is merely one step toward optimization of x-ray heating target design, the demon-

stration of the importance of nonlocal heat transport establishes important common ground between XFEL-based x-ray heating studies and more traditional laser plasma methods.

Submitted April 2017 Physical Review B

3.1 I. Introduction

Dense matter under extreme conditions of pressure (P), temperature (T), or both, is a topic of classic and growing interest across multiple subfields of contemporary science. [1-5] We focus here on the very specific case of femtosecond-scale x-ray heating of crystalline matter, in which there is growing evidence that the lattice often has limited opportunity to structurally relax during the incident x-ray pulses [6-8] and that the loss of crystallinity during the x-ray pulse may have only modest scientific impact. [9] Such studies hold a significant and, we propose, unique position for discovery, because they encompass the case in which the consequences that traditional condensed phase electronic structure theory has on the structure of partially-ionized plasmas will be strongest and most easily interrogated. Hence, the study of crystalline matter at ambient density but highly elevated electronic temperature holds high potential for directly testing foundational issues in finite-T density functional theory, especially including the proper treatment of T-dependent functionals. [10-12]

This point has recently been made by Valenza and Seidler [12], who demonstrated that finite-T DFT makes strong, initially counter-intuitive predictions about the evolution of the absolute and relative Bragg peak intensities in x-ray diffraction (XRD) from crystalline matter as a function of electronic temperature on the 1 – 50 eV scale. The key point is that XRD provides a more detailed interrogation of the population of electronic states for crystalline matter than it does for the more amorphous states interrogated after, e.g., laser shock heating. Furthermore, it is this temperature dependence that is a key *microscopic observable* of all finite-T DFT approaches: the central quantity calculated in DFT is, after all, the spatial distribution of electron density. Therefore, careful characterization of the real-space charge density at elevated electronic temperatures in a cool lattice gives a direct

path to evaluating different DFT implementations. This is particularly significant as regards the temperature-dependent exchange functional, which is essential to predictions of bulk thermodynamic and elastic properties [10,11,13].

However, in such a research program there is a confounding detail. The most effective heating by x-rays will occur with lower-energy photons (that are more strongly absorbed) whereas any detailed interrogation of the real-space charge distribution by XRD requires the use of higher energy x-rays to obtain information over a wide momentum transfer range. [12] This dilemma raises a question that is new in the XFEL community but old in the broader plasma physics community: *Given the incident pulse characteristics and the desired sample material, how does one design a target to achieve optimal energy density deposition?*

The most comprehensive treatment of this question would include a fully spatio-temporal treatment of radiative transport as well as electronic dynamics and electron-atom interactions wherein, again because of the short time scales, lattice relaxation can be ignored or at least is secondary. Within this framework, the temporal evolution of electron-electron and electron-atom interaction includes several stages. First, the atomic physics of the core levels gives rise to an initial population of high-energy Auger electrons and photoelectrons that decay into low-energy (< 50 eV) electronic excitations (both collective and single-particle) on the scale of a few femtoseconds. The resulting collective excitations decay by generating electron-hole pairs on the time scale of tens of femtoseconds. Subsequent electron-electron thermalization occurs on the scale of 100 fs – 1 ps for ambient matter [14-17], but in general has a strong eV-scale temperature dependence, thus requiring a self-consistent treatment at high incident flux levels.[15]

Here, we take a simpler approach with the goal of identifying and illustrating the most important contributors to x-ray heating and how their spatial extent strongly influences optimum x-ray heating target design, in the limited sense of optimizing the deposited net energy density in the desired sample phase. Specifically, we address the key questions surrounding nonlocal energy transport by hot electrons. This topic has a long history in plasma physics, especially for inertial confinement fusion target design, but enters here with typically lower-

energy electrons, i.e., keV-scale, than are important in ICF and in direct-drive laser-heating studies. This causes the energy deposition length of the hot electrons to decrease from the 100-1000 m scale for MeV electrons in laser experiments to instead only \sim 50-200 nm, depending on the atomic number of the species present in the XFEL x-ray heating target.

It is this much shorter length scale that brings us to consider multicomponent nanoscale targets for x-ray heating so that the influence of nonlocal energy transport by the hot electrons can be usefully engineered. While the importance of nanoscale energy transport has not previously been discussed in the context of XFEL heating target design, it has been studied and exploited in other experimental contexts. For example, there exists a significant body of literature in the medical physics community concerned with using gold nanoparticles for dose enhancement in radiotherapy treatment. [18,19] A contrasting application of nonlocal energy transport is found in the macromolecular crystallography community, where there is interest in the use of submicron incident x-ray beams so that a large fraction of high-energy electrons escape the beam spot before slowing down, thus reducing radiation damage in the probed sample volume. [20-24]

With the above context established, we consider here a nanostructured target design that enhances energy deposition in a sample material using nonlocal heat transport from a more strongly x-ray absorbing material in contact with the sample – we refer to this second material as a ‘cladding’ as a matter of convenience, for closer contact to the terminology of laser-shock target design, even when the geometry may not strictly be cladded. Fig. 3.1 sketches several corresponding geometries, but in the current paper we concentrate on the particularly simple one of Fig. 3.1 (c), consisting of a single thin film of sample material clad with Au. We use the Monte Carlo code PENELOPE to simulate three-dimensional electron-photon transport and the corresponding spatial distributions of deposited energy to demonstrate two benefits to the design: first, it significantly enhances in-sample energy deposition, and second, it relaxes constraints on XFEL pump photon energy in a way that substantially increases the information content of XRD measurements in certain experimental contexts.

We proceed as follows. In section II, we describe the methods used to simulate pho-

to ionization and electron transport in a nanostructured target and discuss the simplifying approximations on which we rely. In section III, we present and discuss simulation results of multilayer targets consisting of sample material clad on one or two sides with gold. We find that such a cladding configuration significantly increases deposited energy density in a sample material, with the largest enhancement in low-Z samples. We argue that this enhanced effect in low-Z samples opens the door to wide-angle x-ray diffraction (wide-angle XRD), with significant utility for studying the time dynamics of the energy relaxation cascade for both electronic and lattice/ion degrees of freedom in such materials. These observations are particularly relevant in the context of two-color x-ray pump x-ray probe experiments at XFELs[25-29], but also serve more generally to establish the importance of nanoscale nonlocal heat transport in high-intensity XFEL studies. Finally, in section IV we conclude.

3.2 II. Methods

The simulation of electron transport in condensed matter is an area of ongoing research. In addition to continuing development of well-established codes in the high-energy experimental particle physics community [30,31], new developments include incorporation of *ab initio* band structure calculations in order to accurately model the electron mean free paths of interband transitions and plasmon excitations from relativistic energies down to a few eV. [32,33]

In the regime relevant to the present study, calculation of the spatial distribution of deposited energy caused by absorption of a hard x ray requires accurate treatment of the processes that describe scattering of photo- and Auger electrons at the 100 eV to 10 keV scale (generation of secondary x-ray photons, though present, plays a negligible role in energy transport). The simplest atomic treatments of elastic and inelastic scattering demonstrate that, for mid- and high-Z elements, the ratio of elastic to inelastic total cross sections is of order unity and that characteristic elastic scattering angles are sufficiently large (for instance, of order 1 rad for \sim 1 keV electrons) to influence deposited energy distributions. [34] Both components, therefore, must receive accurate treatments to adequately model spatial energy deposition distributions in a nanostructured target.

The spatial distribution of deposited energy is determined by the electron stopping power $\frac{dE}{dz}$, which in a classical treatment is related to a material's dielectric function $\varepsilon(q, \omega)$ by

$$\frac{dE}{dz} = \frac{2^2}{\pi a_0 m_0 v^2} \iint \frac{q_y \omega \operatorname{Im}[\frac{-1}{\varepsilon(q_y, \omega)}]}{q_y^2 + (\frac{\omega}{v})^2} dq_y d\omega, \quad (1)$$

where ω is angular frequency, q is momentum transfer (with q_y the magnitude of the component for momentum transfer perpendicular to the z-direction), a_0 is the Bohr radius, m_0 is the electron mass, and v is the electron velocity. [34] In the case of electron showers generated by 5-10 keV photons, the electron stopping power's dependence on v causes nonlocal energy transport to be dominated by the highest-energy Auger and photoelectrons. Though the slower time evolution of the subsequent electronic and lattice dynamics may be neglected in the present context of simulating fsec-scale energy transport, the possibility of interrogating it by time-resolved XFEL pump-probe measurement is an interesting topic in its own right.[25,26]

To model the above physics we used the code PENELOPE, which implements particle-tracking Monte Carlo simulations of electron showers generated by x-ray photoionization.[31] PENELOPE uses total and differential cross sections based on several physical models. Briefly, it derives elastic and inner-shell inelastic cross sections from strictly atomic wave functions, while the valence contribution to the inelastic double differential cross section is based on the Born approximation and generalized oscillator strength model of Liljequist [35,36], with an energy loss-dependent normalization that allows the model to replicate empirical stopping power data (provided as program input). Although the inelastic scattering cross section is dominated by low-energy loss collisions, inner shells contribute the majority of the stopping power for several-keV electrons, which account for the longest-range energy transport. For electrons of those energies the stopping power of a compound may be approximated within five percent by a stoichiometric sum based on atomic treatments of its constituents (an observation referred to as Bragg's rule). [37] Consequently we employed material data files generated by the PENELOPE 2011 program MATERIAL, which applies

this approximation to infer stopping powers of arbitrary compounds using data from the NIST ESTAR database. [31,38]

3.3 III. Results and discussion

We now present results for several realizations of our nanostructured target design, all of which consist of thin films clad with Au on one or both sides. The heating of an Fe thin film via nonlocal heat transport by hot electrons is illustrated in Fig. 3.2, which shows a two-dimensional projection of electron trajectory traces in an Au-Fe-Au trilayer stimulated with 7 keV incident photons. The color-coding of the tracks shows that, due to the much larger number of photoexcitations in the Au cladding compared to Fe inclusion, most hot electrons propagating in the Fe are part of a photoionization relaxation cascade originating in the cladding. Inelastic scattering of these hot electrons is the dominant contribution to energy deposition in the central Fe region, as quantified by Fig. 3.3, which compares the linear energy deposition of several Au-Fe-Au trilayer configurations to that in bare Fe.

Photoionization by 7 keV photons yields mean energy deposition lengths l of 15.0 nm and 35.3 nm, respectively, in simulated bare Fe and bare Au targets, where $l = \int_{z=0}^{\infty} z(\vec{r}) \rho(\vec{r}) d^3\vec{r}$, with $\rho(\vec{r})$ the volume density of deposited energy and z the magnitude of the projection of \vec{r} onto a fixed, arbitrary unit vector. Consistent with the above characteristic lengths, we found that absorbed energy density in the Fe inclusion saturates beyond an Au cladding thickness of 50 nm. Fig. 3.3 (a) shows the deposited energy distribution in a bare Fe_3O_4 target and in several Au- Fe_3O_4 -Au trilayers with varying thicknesses of the Fe_3O_4 inclusion. An interior layer thickness of 50 nm results in a factor of five enhancement in deposited energy density relative to the bare Fe_3O_4 target. The increase in deposited energy density in a clad sample compared to a bare one is significantly larger for lower-Z materials, reaching a factor of 100 for an Au-C-Au target of the same geometry (Fig. 3.4).

These enhancements in energy deposition increase the accessible thermodynamic parameter space in all XFEL heating experiments, which is particularly significant for experimental diagnostics that require deviation from optimal pump pulse characteristics and are therefore

normally incompatible with heating studies, for instance XRD. We illustrate this in Fig. 3.5, which compares the energy deposition in Au-Fe-Au and Au- Fe_3O_4 -Au targets stimulated with photons below the K -edge of Fe to that in a bare Fe target heated by photons above the edge. Nonlocal heating of the former samples compensates for the reduction in sample heating caused by lowering the incident photon energy below the Fe K -edge; the multicomponent targets thus allow improving the ratio of signal to (fluorescence) background while—in the more favorable case of Fe_3O_4 —maintaining an energy deposition density comparable to the highest level possible with an equivalent monolithic target. However, Fig. 3.6 also demonstrates a tradeoff of the cladding’s presence: the diffracted signal from Au is stronger than that from the sample, making the described reduction in background worthwhile only assuming sufficient separation between Bragg peaks of the sample and cladding.

Low-Z sample materials provide a separate, independently interesting, case for the use of structured target design in XRD studies. In such materials, nonlocal heat transport is effective over a much wider range of incident photon energies compared to direct x-ray absorption. Until now, x-ray heating studies of low-Z materials, such as graphite, have required incident photon energies below 3 keV to reach HED conditions ($> \sim 1$ eV temperatures) due to these materials’ small photoelectric cross sections in the hard X ray (photon energy > 5 keV) regime. This restriction limits the kinematically accessible range of momentum transfers in XRD, which correspondingly reduces available information on real-space charge density.

This creates an experimental dilemma with scientific consequences. For example, Hau-Riege *et al.*[39] showed evidence for ultrafast melting of graphite during a 40 fs-long XFEL pulse but were limited, for the reason described above, to using 2 keV incident photons, yielding diffraction from only the 002 Bragg reflection of graphite. The authors interpreted quenching upon heating of the 002 peak as evidence of nonthermal lattice melting. However, Valenza *et al.*[12] questioned this conclusion based on simulated diffraction using frozen-core finite-T DFT calculations, which predicted strong quenching of the graphite 002 reflection due to purely electronic reorganization in crystalline graphite at 10 eV electronic temperature. In graphite and other low-Z systems, the only means of unambiguously separating

lattice disorder from electronic heating in the XRD signal is to probe several Bragg peaks, including the lowest-order reflections and their harmonics. [12]

It is therefore interesting to ask whether high energy-densities can be achieved in graphite when using photons suitable for wide-angle scattering. In Fig. 3.4 we show the deposited energy densities in Au-C-Au trilayers of several interior thicknesses, once again using 7 keV incident photons (sufficient to probe the 006 reflection of graphite). The deposited energy density in the interior layer is at least a factor of 100 greater compared to an unclad sample with the same incident photon energy, and a factor of two greater compared to an unclad sample stimulated with 2 keV photons. Indirect heating via high-Z cladding thus eliminates the constraint of selecting incident photon energies near a low-Z material's small core binding energies, making wide-angle XRD possible. In the context of carbon, the weakness of the XRD from C compared to Au can be uniquely compensated with a highly-oriented pyrolytic graphite (HOPG) sample, whose high-reflectivity $00l$ peaks yield much higher signal to background ratios than the powder-like Bragg and thermal diffuse scattering of polycrystalline Au. Similar configurations exploiting mosaic or single-crystal samples may enhance wide-angle XRD on a variety of low-Z systems, offering a much-improved ability to experimentally test predictions of finite-T DFT-based modeling of electronic structure in low-Z condensed matter, where finite-T effects are easiest to identify because of the relatively large valence-electron contribution to the XRD signal.[12]

The simulations presented in this paper constitute a first demonstration of a particularly simple implementation of structured target design. One can imagine several improved designs that achieve the same level of nonlocal sample heating while averting some of the disadvantages of our multilayer approach. For example, a uniform mixture of small (< 50 nm diameter) sample and heater nanoparticles would show similar mean deposited energy densities to a multilayer target and can be prepared by, e.g., spin coating or drop-casting. Such targets would have more homogeneous heating and would additionally allow preparation of much thicker targets and give much higher scattered intensities. A similar result may be possible using electrochemical or vapor deposition to embed sample materials inside porous

high-Z metal substrates.[40,41] Two-color XFEL experiments may also lend themselves to lithographically patterned designs with concentric cylindrical volumes of (inner) sample and (outer) cladding materials, wherein the more tightly-focused probe pulse would be inscribed in a volume free of cladding material. Such a configuration would have the intention of reducing (cladding) background relative to signal, which would be particularly useful for weakly-diffracting low-Z samples.

3.4 IV. Conclusion

We model the spatial distribution of deposited energy in nanostructured targets for hard x-ray XFEL heating experiments using the Monte Carlo code PENELOPE. We find that two-component targets consisting of a sample material and high-Z cladding achieve substantial nonlocal heating of the sample via the relaxation cascade following transport of multi-keV Auger and photoelectrons. We argue that this target design approach will bring substantial benefits to XFEL heating experiments in the following ways: first, by enlarging their accessible thermodynamic parameter space and second, by improving the capability of x-ray diffraction diagnostics to characterize finite-temperature electronic structure and to distinguish between thermalization of the electronic and lattice degrees of freedom in crystalline warm dense matter systems.

3.4.1 Acknowledgements

We thank Joshua Kas for useful discussions. This work was supported by the United States Department of Energy, Basic Energy Sciences, under grant DE-SC00008580 and by the Joint Plasma Physics Program of the National Science Foundation and the Department of Energy under grant DE-SC0016251.

References

- [1] R. P. Drake, *High-Energy-Density Physics: Fundamentals, Inertial Fusion, and Experimental Astrophysics* (Springer, 2006), Shock Wave and High Pressure Phenomena.

- [2] S. Krishnan, S. Ansell, J. J. Felten, K. J. Volin, and D. L. Price, Physical Review Letters **81**, 586 (1998).
- [3] J. J. Fortney, S. H. Glenzer, M. Koenig, B. Militzer, D. Saumon, and D. Valencia, Physics of Plasmas **16**, 041003 (2009).
- [4] S. Glenzer and R. Redmer, Review of Modern Physics **81**, 1625 (2009).
- [5] R. C. Davidson, National Research Council of the National Academies, *Frontiers in High Energy Density Physics: The X-Games of Contemporary Science* 2003.
- [6] S. P. Hau-Riege, Physical Review E **87**, 4, 053102 (2013).
- [7] S. Boutet *et al.*, Science **337**, 362 (2012).
- [8] H. N. Chapman *et al.*, Nature **470**, 73 (2011).
- [9] C. Caleman, N. Timneanu, A. V. Martin, H. O. Jonsson, A. Aquila, A. Barty, H. A. Scott, T. A. White, and H. N. Chapman, Optics Express **23**, 1213 (2015).
- [10] V. V. Karasiev, T. Sjostrom, and S. B. Trickey, Physical Review B **86**, 115101 (2012).
- [11] V. V. Karasiev, T. Sjostrom, and S. B. Trickey, Physical Review E **86**, 056704 (2012).
- [12] R. A. Valenza and G. T. Seidler, Physical Review B **93**, 115135 (2016).
- [13] T. Bredow and A. R. Gerson, Physical Review B **61**, 5194 (2000).
- [14] W. S. Fann, R. Storz, H. W. K. Tom, and J. Bokor, Physical Review B **46**, 13592 (1992).
- [15] J. Faure *et al.*, Physical Review B **88**, 075120 (2013).
- [16] M. Lisowski, P. A. Loukakos, U. Bovensiepen, J. Sthler, C. Gahl, and M. Wolf, Applied Physics A **78**, 165 (2004).
- [17] I. Timrov, T. Kampfrath, J. Faure, N. Vast, C. R. Ast, C. Frischkorn, M. Wolf, P. Gava, and L. Perfetti, Physical Review B **85**, 155139 (2012).
- [18] C. Lee, N. N. Cheng, R. A. Davidson, and T. Guo, The Journal of Physical Chemistry C **116**, 11292 (2012).
- [19] M. K. K. Leung, J. C. L. Chow, B. D. Chithrani, M. J. G. Lee, B. Oms, and D. A. Jaffray, Medical Physics **38**, 624 (2011).

- [20] E. A. Stern, Y. Yacoby, G. T. Seidler, K. P. Nagle, M. P. Prange, A. P. Sorini, J. J. Rehr, and A. Joachimiak, *Acta Crystallographica Section D-Biological Crystallography* **65**, 366 (2009).
- [21] Y. Z. Finfrock, E. A. Stern, R. W. Alkire, J. J. Kas, K. Evans-Lutterodt, A. Stein, N. Duke, K. Lazarski, and A. Joachimiak, *Acta Crystallographica Section D-Biological Crystallography* **69**, 1463 (2013).
- [22] Y. Z. Finfrock, E. A. Stern, Y. Yacoby, R. W. Alkire, K. Evans-Lutterodt, A. Stein, A. F. Isakovic, J. J. Kas, and A. Joachimiak, *Acta Crystallographica Section D-Biological Crystallography* **66**, 1287 (2010).
- [23] C. Nave and M. A. Hill, *Journal of Synchrotron Radiation* **12**, 299 (2005).
- [24] R. Sanishvili *et al.*, *Proceedings of the National Academy of Sciences of the United States of America* **108**, 6127 (2011).
- [25] A. A. Lutman, R. Coffee, Y. Ding, Z. Huang, J. Krzywinski, T. Maxwell, M. Messerschmidt, and H. D. Nuhn, *Physical Review Letters* **110**, 134801, 134801 (2013).
- [26] A. Marinelli, A. A. Lutman, J. Wu, Y. Ding, J. Krzywinski, H. D. Nuhn, Y. Feng, R. N. Coffee, and C. Pellegrini, *Physical Review Letters* **111**, 134801, 134801 (2013).
- [27] I. Inoue *et al.*, *Proceedings of the National Academy of Sciences* **113**, 1492 (2016).
- [28] P. J. Ho, E. Kanter, and L. Young, *Physical Review A* **92**, 063430 (2015).
- [29] E. Allaria *et al.*, *Nature Communications* **4**, 2476 (2013).
- [30] S. Agostinelli *et al.*, *Nuclear Instruments and Methods in Physics Research Section A: Accelerators, Spectrometers, Detectors and Associated Equipment* **506**, 250 (2003).
- [31] F. Salvat, J. M. Fernández-Varea, and J. Sempau, *PENELOPE-2006: A code system for Monte Carlo simulation of electron and photon transport* (OECD Publishing, Paris, 2006).
- [32] F. Gao, Y. Xie, Z. G. Wang, S. Kerisit, D. X. Wu, L. W. Campbell, R. M. Van Ginhoven, and M. Prange, *Journal of Applied Physics* **114**, 173512 (2013).
- [33] M. Prange, D. Wu, Y. Xie, L. W. Campbell, F. Gao, and S. Kerisit, *Radiation response of inorganic scintillators: insights from Monte Carlo simulations* (SPIE, 2014),

92130L.

- [34] R. F. Egerton, *Electron energy-loss spectroscopy in the electron microscope* (Springer Science & Business Media, 2011).
- [35] J. M. Fernández-Varea, R. Mayol, D. Liljequist, and F. Salvat, *Journal of Physics: Condensed Matter* **5**, 3593 (1993).
- [36] D. Liljequist, *Journal of Physics D: Applied Physics* **16**, 1567 (1983).
- [37] G. D. Zeiss, W. J. Meath, J. C. F. MacDonald, and D. J. Dawson, *Radiation Research* **70**, 284 (1977).
- [38] M. J. Berger, NIST, *ESTAR, PSTAR, and ASTAR: Computer programs for calculating stopping-power and range tables for electrons, protons, and helium ions*, 1992.
- [39] S. P. Hau-Riege *et al.*, *Physical Review Letters* **108**, 217402 (2012).
- [40] C. H. Bak, K. Kim, K. Jung, J.-B. Kim, and J.-H. Jang, *Journal of Materials Chemistry A* **2**, 17249 (2014).
- [41] M. Bagge-Hansen *et al.*, *The Journal of Physical Chemistry C* **118**, 4078 (2014).

Figure 3.1: Representations of three types of multicomponent targets composed of sample material (green) and heater cladding (yellow). (a): A porous substrate filled with sample material; (b): a mixture of cladding and sample nanoparticles embedded in a solid matrix; (c): a multilayer film.

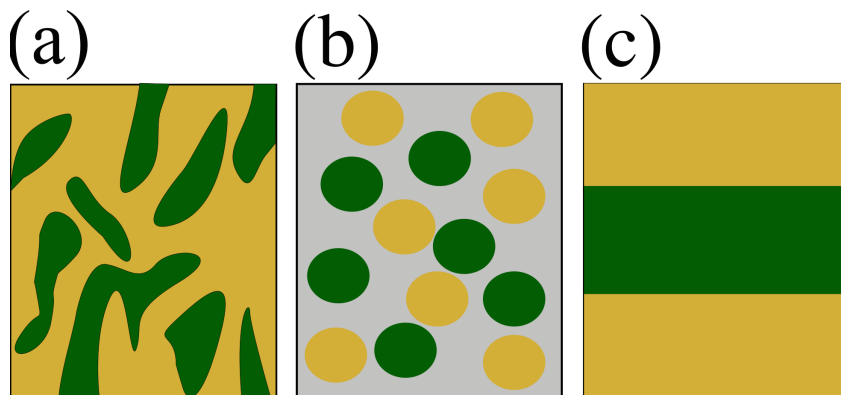


Figure 3.2: Visualization of a 3-D Monte Carlo simulation of electron transport in an Au-Fe-Au target heated by 7 keV photons, incident normally from the top of the page. Electron tracks are projected onto the plane of the page; showers resulting from photoexcitation of Au and Fe atoms are red and blue, respectively. Note that most of the electron tracks in the Fe are due to absorption events in the Au.

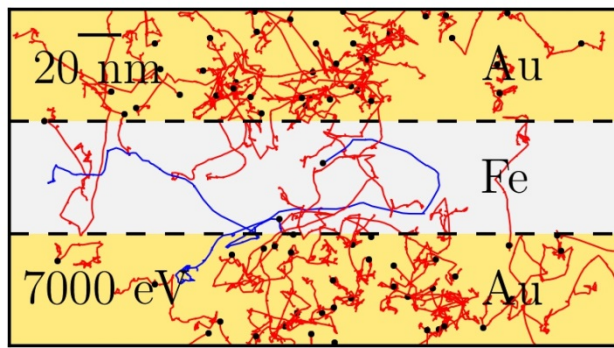


Figure 3.3: (a) Linear energy deposition density generated by 7 keV photons incident on an Au- Fe_3O_4 -Au target, displayed for several thicknesses of the central Fe_3O_4 layer and a fixed Au cladding thickness of 50nm. (b) Histograms of energy deposition density in volume elements of the Fe_3O_4 inclusions in Au- Fe_3O_4 -Au targets, displayed for several thicknesses of the Au cladding and a fixed Fe_3O_4 layer thickness of 50 nm.

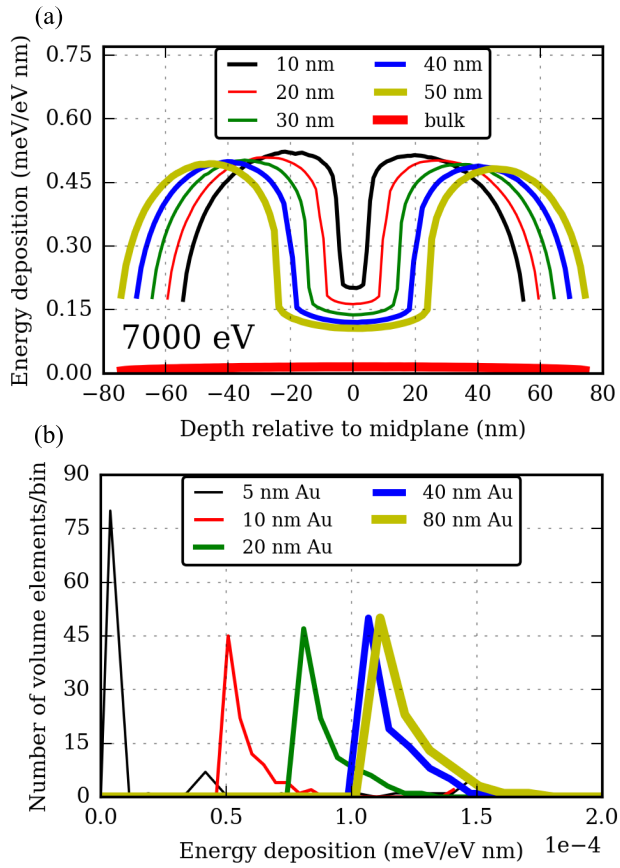


Figure 3.4: Linear energy deposition due to 7 keV photons incident on an Au-C-Au target displayed for several thicknesses of the central C layer and a fixed outer cladding thickness of 50nm.

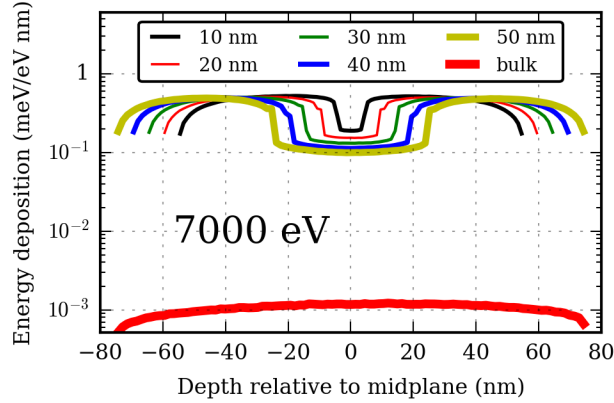


Figure 3.5: Linear energy deposition in layered Au-Fe-Au and Au- Fe_3O_4 -Au targets of 150 nm total thickness stimulated by 7 keV photons. Dashed lines indicate energy deposition in bulk Fe_3O_4 and Fe at photon energies of 7.12 keV (above the iron K-edge) and 7 keV (below the edge). The multilayer configuration sufficiently enhances energy deposition so as to partially compensate for the difference between pre- and above-edge x-ray photoelectric cross sections. The benefit is particularly pronounced in Fe_3O_4 due to its much lower density and photoelectric cross-section.

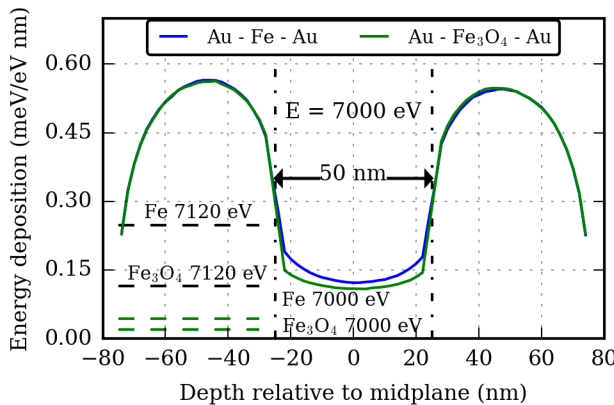
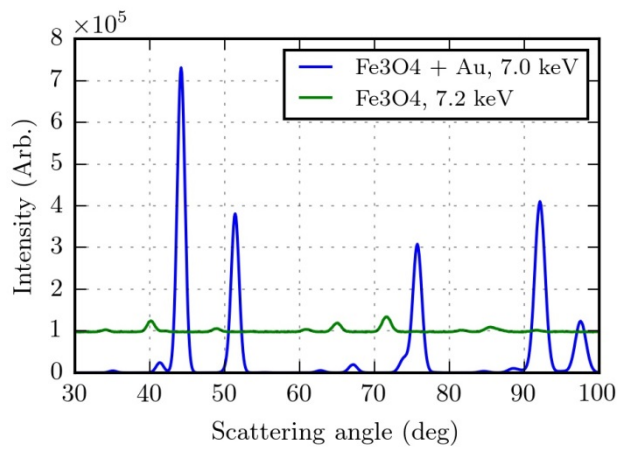


Figure 3.6: Simulated powder diffraction of 50 nm Au-50 nm Fe_3O_4 -50 nm Au stimulated by X-rays below the Fe K-edge (blue) compared to that resulting from photons above the edge incident on bare Fe_3O_4 , including fluorescence background(green).



Chapter 4

A PHOTOMETRIC STUDY OF ENERGY-DISPERSIVE X-RAY DIFFRACTION AT A LASER PLASMA FACILITY

O.R. Hoidn and G.T. Seidler^(*)

Physics Department

University of Washington

Seattle WA 98195-1560

Abstract

The low repetition rates and possible shot-to-shot variations in laser-plasma studies place a high value on single-shot diagnostics. For example, white-beam scattering methods based on broadband backlighter x-ray sources are used to determine changes in the structure of laser-shocked crystalline materials by the evolution of coincidences of reciprocal lattice vectors and kinematically-allowed momentum transfers. Here, we demonstrate that white-beam techniques can be extended to strongly-disordered dense plasma and warm dense matter (WDM) systems where reciprocal space is only weakly structured and spectroscopic detection is consequently needed to determine the static structure factor and thus the ion-ion radial distribution function. Specifically, we report a photometric study of energy-dispersive diffraction (ED-XRD) for structural measurement of high energy density systems at large-scale laser facilities such as OMEGA and the National Ignition Facility. We find that structural information can be obtained in single-shot ED-XRD experiments using established backlighter and spectrometer technologies.

(*) Corresponding author: *seidler@uw.edu*

4.1 I Introduction

In addition to their centrality for inertial confinement fusion studies,^{1, 2} laser-shock experiments play a growing role at the interface between plasma physics and condensed matter physics, geosciences, and laboratory astrophysics.³⁻¹⁴ However, for experiments reaching the highest energy density states the technical challenges extend beyond the creation of such states: the low repetition rates, limited facility access, and significant shot-to-shot variations each place a special emphasis on single-shot x-ray diagnostics of the structural and electronic properties of the compressed, heated target.¹⁵⁻²⁴ An important case-in-point is provided by the determination of the ion-ion radial distribution function, $g_{ii}(\vec{r})$, or equivalently the static structure factor $S(\vec{k})$. Knowledge of $g_{ii}(\vec{r})$ fulfills an interesting variety of roles. First, it is necessary, if only at the level of mean density and average ionization state, for investigation of any equations of state (EOS) and of molecular dynamics simulations or other structural calculations performed in support of EOS calculations. Second, it is also a critical input parameter to any fine treatment of electronic structure. The electronic structure of dense crystalline systems and plasmas, in turn, is a quantity of fundamental interest but also of a certain pragmatic interest: some sufficient knowledge of electronic structure is needed for reliable determination of the target temperature and ionization state in dense plasma and warm dense matter (WDM) experiments^{25, 26}, and this capability is in turn needed for campaigns to experimentally measure the EOS in the WDM regime²⁷⁻²⁹.

For targets that retain substantial medium- or long-range order upon shock compression, broadband backlighter x-ray sources enable white-beam angle-dispersive x-ray diffraction (AD-XRD) in which substantial structural detail can be inferred from Kossel rings³⁰ and other fine scattering patterns dictated by the coincidence of reciprocal lattice vectors and kinematically-allowed momentum transfers^{31, 32}. However, white-beam AD-XRD is only applicable to systems that are substantially single crystalline: any statistically isotropic system, whether a polycrystalline fine-powder sample or a dense, partially ionized plasma, when illuminated by a broad-band source will show an angularly-featureless signal when

observed on, *e.g.*, an image plate. For high atomic number (Z) systems, single-shot white-beam extended x-ray absorption fine structure (EXAFS) has seen some applications³³; the situation has proven more challenging for lower- Z WDM and dense plasmas, as a result of the mutually-exclusive target thickness requirements of the x-ray measurement (soft x-ray penetration lengths of order 1 micron or less) and laser ablation (necessary thicknesses of tens of microns)³⁴. Consequently, the first determination of $g_{ii}(r)$ for disordered, dense lower- Z plasma systems³⁵ instead used multi-shot, quasi-monochromatic AD-XRD, *i.e.*, ‘traditional’ XRD.

Here, we investigate whether single-shot, white-beam XRD can be performed on *strongly disordered*, laser-shocked solids and WDM using spectral information at the detector location to parameterize the momentum transfer of the quasielastic scattering event, *i.e.*, we consider purely energy-dispersive x-ray diffraction (ED-XRD). Some context is needed to fully define this term and to distinguish it from XRD methods already in use in the laser-plasma community. The differential scattering cross section per atom for coherent scattering of x rays (ordinary diffraction of incoherent incident photons) from an isotropically disordered, elemental material such as a powder sample, liquid, or dense laser-shock heated plasma of a single atomic species is

$$\frac{d\sigma_{coh}}{d} (k) = \sigma_t S(k) f(k)^2 \quad (1)$$

where σ_t is the Thomson cross section, $S(k)$ is the directionally-averaged structure factor and $f(k)$ is the spherically averaged atomic form factor. The structure factor $S(k)$ is simply related by a sine transform to $g_{ii}(r)$,

$$S(k) = 1 + (4 \pi \rho/k) \int_0^\infty dr r [g_{ii}(r) - 1] \sin(kr). \quad (2)$$

These well-known expressions establish the close connection between XRD and $g_{ii}(r)$ while also demonstrating the need to measure the differential scattering cross-section (and hence $S(k)$) at many different momentum transfers if any significant constraint on the form of $g_{ii}(r)$ is to be obtained.

The k -dependence of $d\sigma_{coh}/d\Omega$ can in principle be measured with any suitable combinations of scattering angle 2θ and photon energies spanning the needed momentum trans-

fers: k is chosen by the combined effect of these two experimentally-selectable parameters, $k = (2E/c)\sin 2\theta$. In practice, however, XRD is measured in only two modes: angle-resolved XRD (henceforth ‘AR-XRD’) and energy-dispersive XRD (henceforth ‘ED-XRD’). Their distinction is best introduced kinematically. As illustrated in Fig. 4.1, any measurement of $S(k)$ must follow a curve in E - 2θ space which crosses many of the shown contours of constant k . The parameter space probed by a typical AR-XRD experiment using ~ 8 keV monochromatic incident photons is represented by the vertical curve in the figure. Experimentally, the necessary apparatus will include a monochromatic source and either an angle-scanning detector or a position sensitive detector (PSD), which we show schematically in Fig. 4.3 (a) and (b). On the other hand, a typical ED-XRD experiment instead resides on the horizontal curve in Fig. 4.1, *i.e.*, at a fixed scattering angle of 135 degrees but requiring both a broad incident source spectrum and an energy-resolving detector. An experimental schematic for ED-XRD is presented in Fig. 4.3(c). We note that ED-XRD has a long history in laboratory and synchrotron XRD studies, and plays an important role in high-pressure diamond anvil cell research where the limited angular access to the sample space substantially complicates AD-XRD.³⁶⁻⁴⁰ There is then an obvious commonality with experiments at large-scale laser facilities; angular access at such facilities is strongly constrained by the beam paths of the laser light itself.

AD-XRD from laser-shock compressed, disordered Al has recently been reported by Ma, *et al.*,³⁵ and this first such study illustrates both the scientific benefits and technical drawbacks of AD-XRD for large-scale laser facilities. Specifically, concerning the latter, a few high-resolution spectrometers must be moved between different scattering angles for different shots so as to obtain a complete characterization of $S(k)$ by pooling the results of many shots after suitable normalization or other characterization of shot-to-shot variations in the source or target. While the study of Ma, *et al.*,³⁵ has overcome these challenges and provides an interesting comparison of experiment to modern theoretical treatments of the structure of dense plasmas, it is still important to note that the use of a multi-shot technique has, at a minimum, decreased the range of phase space that can be studied subject to the strong

constraints that exist on facility access. A single-shot alternative could therefore have high scientific impact and is likely the only way that $S(k)$ will be measured on disordered dense plasmas at the National Ignition Facility, where the number of shots per scientific study is especially limited.

Consequently, with the above context established, we report here a photometric analysis of ED-XRD for laser-shock experiments illuminated by broad-band backlighter sources. This analysis makes use of known results for the spectrum of a broad-band backlighter, representative experimental results for $S(k)$ for disordered systems, and representative, established technical characteristics of spectrally-resolving detectors available at large-scale laser facilities. We find significant benefits to ED-XRD for disordered systems, including single-shot determination of $S(k)$, and we propose that ED-XRD should become a standard diagnostic at large-scale facilities such as OMEGA and the National Ignition Facility.

We continue as follows. In section 2 we describe the methods used in the photometric analysis, including the reference target, modeled experimental geometry, and any assumptions about detector or spectrometer performance. In section 3 we present and discuss our results for ED-XRD using each of two different experimental configurations. These are, first, an x-ray CCD detector operating in single-photon mode as an energy-resolving solid-state detector and, second, a wavelength-dispersive spectrometer using a highly-oriented pyrolytic graphite (HOPG) mosaic crystal as the diffractive element. The CCD configuration is viable, but has some drawbacks associated with saturation and double-counting that require special care. We find that the HOPG-based spectrometer quite easily resolves the energy spectrum of the diffraction with excellent counting statistics for a broad-band backlighter that has been fielded at OMEGA, with the caveat that a single HOPG crystal analyzer covers a narrower energy range, and hence a more restricted k -range, than a CCD detector. Finally, in section IV we conclude.

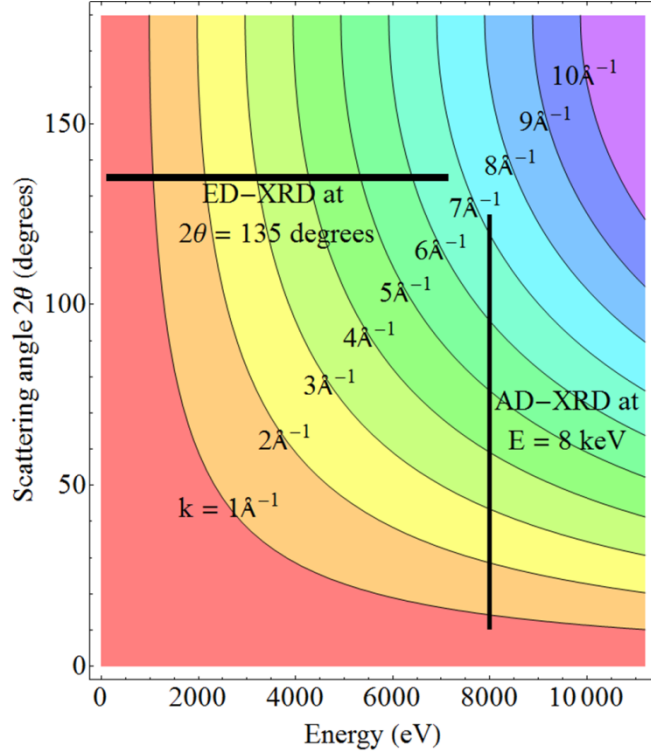
4.2 II Methods

4.2.1 II.A. Source and target

One readily available broadband source in laser shock experiments is the thermal spectrum from a laser-imploded polymer shell, usually filled with H₂-D₂ gas^{41, 42}. In Fig. 4.7 we show a typical spectrum collected at OMEGA⁴³. Because of the spectrum's supra-exponential decay, an ED-XRD experiment with this source is preferentially conducted at low energy, between 2 and 6 keV, as shown in the ED-XRD curve at a scattering angle of 135 degrees in Fig. 4.1. Also shown in Fig. 4.7 is the spectrum for a typical narrow band backscatterer source at OMEGA, where these sources have seen extensive use in x-ray scattering studies, both elastic (XRD)³⁵ and inelastic (usually called 'x-ray Thomson scattering')²⁵. The narrow-band spectrum is obtained by scaling the spectrum of a Cu *K* target driven by a 10 J, 10 ps laser pulse at the MTW laser facility to a 2.5 kJ, 10 ps laser pulse at OMEGA, using a typical *K* photon yield of $4 \cdot 10^{10}$ photons per J of laser energy^{44, 45}.

We consider two target systems where experimental $S(k)$ are available: liquid boron at ambient pressure and shock-compressed aluminum. For liquid boron we use the experimental results of Krishnan *et al.*^{46, 47}, the data for which were taken at a synchrotron light source using hydrodynamically-levitated boron heated to 2400K by continuous illumination from infrared lasers. While this is not a WDM system *per se*, it is a reasonable surrogate. As shown in Fig. 4.2.1 (a), note the presence of a few broad peaks in $S(k)$, representative of a system with only limited, short-range information in $g_{ii}(r)$. For clarity in our photometric analysis, we will use a smoothed $S(k)$ where the sharp (nonphysical) noise in the experimental $S(k)$ has been filtered. On the other hand, $S(k)$ for shock-compressed aluminum ($n_e = 5.4 \cdot 10^{23} \text{ cm}^{-3}$; $T_e = 10 \text{ eV}$) is based on results from Ma *et al.*³⁵, who have recently reported the first AD-XRD measurement of a shock-compressed, disordered WDM system. $S(k)$ was recovered from Ma *et al.*'s theoretical calculation of an elastic scattering profile for triply-ionized shock-compressed aluminum, to which they fit their data. We note that only an approximate atomic form factor, that of ambient aluminum, was used to calculate $S(k)$ from

Figure 4.1: Contours of equal momentum transfer k (labeled in units of \AA^{-1}) in energy and scattering angle. Angle-dispersive x-ray diffraction (AD-XRD) and energy-dispersive x-ray diffraction (ED-XRD) take vertical and horizontal cuts, respectively, to achieve broad coverage in k and thus obtain information about the radial distribution function.



the scattering profile; however, the resulting error in $S(k)$ is expected to be negligible above $k = 3\text{\AA}^{-1}$, and hence does not affect the location of any coordination peaks. As shown in Fig. 4.2.1 (b), note again that the presence of only short-range order in the target results in a simple form for $S(k)$. In this case, the information content is largely limited to the location and intensity of the obvious first coordination peak.

4.2.2 II.B. Photon-electron interactions and numerical modeling

For the targets considered here, the experiment is conducted in an energy region far above any atomic fluorescence from the targets and also far above any soft x-ray blackbody radi-

ation from the surface or bulk of the target, each of which is easily attenuated in practice with a thin plastic or Be shield. Consequently, we need only consider the coherent and incoherent scattering of the x-rays as direct contributors to the measured scattering signal; the photoelectric interaction appears only in its contribution to absorption coefficient in the energy range of interest. Note that by coherent here we refer to the quasielastic scattering process itself, *i.e.* “ordinary” diffraction, with no expectation of coherence of the incident beam (such as is used in diffraction experiments at XFEL facilities).

Given a backlighter source with fluence $I_{\text{source}}(E)$ (units of photons/eV, integrated over 4 steradian) at a distance d_{source} from the target, the areal flux incident in the target is $I_{\text{incident}}(E) = I_{\text{source}}(E) / 4\pi d_{\text{source}}^2$. The contribution of coherent scattering to the measured energy spectrum at a scattering angle 2θ is then

$$I_{\text{coh}}(E, 2\theta) = I_{\text{incident}}(E) \frac{d\sigma_{\text{coh}}}{d}(k) d\Omega_{\text{det}} \eta_{\text{det}}(E) \tau_{\text{coh}}(E, 2\theta), \quad (3)$$

where k is implicitly determined by E and 2θ , $d\Omega_{\text{det}}$ is the solid angle subtended by the detector, $\eta_{\text{det}}(E)$ is the net efficiency of detection of photons of energy E that arrive in $d\Omega_{\text{det}}$, and $\tau_{\text{coh}}(E, 2\theta)$ includes the necessary corrections to the measured XRD due to the target’s geometry and energy-dependent absorption coefficient³⁴. When operating near to a backscattering geometry, for example, $\tau_{\text{sample}}(E, 2\theta) \sim \rho A(1 - e^{-2\mu(E)d})/2\mu(E)$ where ρ is atomic (number) density, A is the cross-sectional area of the portion of the backlighter beam that illuminates the target region of interest, d is the target thickness, and $\mu(E)$ is the x-ray absorption coefficient. For present purposes, $d\sigma_{\text{coh}}/d\Omega$ includes all elastic and quasielastic scattering; it integrates over all ion-ion correlation dynamics⁴⁸.

The incoherent contribution to the measured signal is somewhat more complex to model. The microscopic physics of the incoherent scattering processes, wherein one must address both momentum transfer (k) and energy transfer (ω), results in the need for a double differential cross-section $d^2\sigma_{\text{incoh}} \frac{(k, \omega)}{dd} \Omega$. The detected intensity from incoherent scattering is then

$$I_{\text{incoh}}(E, 2\theta) = d\Omega_{\text{det}} N_{\text{atoms}} \frac{d\sigma_t}{d\Omega} \int_0^\infty dE' I_{\text{incident}}(E') S_{\text{incoh}}(k, \omega) \tau_{\text{incoh}}(E', E, 2\theta) \quad (4),$$

where N_{atoms} is the number of atoms in the target, k is again implicitly determined by E ,

E' , and 2θ and $\tau_{\text{incoh}}(E', E, 2\theta)$ includes the influence of attenuation for an incident photon of energy E' that scatters through an angle 2θ and departs the incoherent interaction with energy E . In the first Born approximation, $d^2\sigma_{\text{incoh}}/d\omega d\Omega = (d\sigma_t/d\Omega) S_{\text{incoh}}(k, \omega)$, where $d\sigma_t/d\Omega$ is the Thomson differential scattering cross section and $S_{\text{incoh}}(k, \omega)$ is the inelastic component of the dynamic structure factor. In the independent-electron approximation^{49, 50}, $S_{\text{incoh}}(k, \omega)$ may be expressed as a sum over electrons and matrix elements between the initial and final states of the system:

$$S_{\text{incoh}}(k, \omega) = \sum_j \sum_{f \neq i} \left| \langle i | e^{i \mathbf{q} \bullet \mathbf{r}_j} | f \rangle \right|^2 \delta(E_f - E_i - \omega). \quad (5)$$

At sufficiently high k , $S_{\text{incoh}}(k, \omega)$ is peaked at the Compton shift $\Delta E = ^2 k^2 / 2 m$. In the high- k (non-collective) scattering regime the total inelastic portion of the dynamic structure factor is constructed using equation (5) evaluated as a sum over individual valence and core electrons. In our modeling procedure this consists of truncated valence and core Compton profiles generated in the impulse approximation^{50, 51} where $S_{\text{incoh}}(k, \omega)$ depends only on the ground state electronic density and kinematics of the scattering process. The first moment of $S_{\text{incoh}}(k, \omega)$ was normalized after truncation according to the Bethe f -sum rule⁵². For boron our approximation yields incoherent scattering cross sections which exceed experimental values by up to 30 percent, making our approximate treatment of the incoherent background conservative. In the relevant range of momentum transfers the Compton shift is sufficiently small that we substitute $\tau_{\text{coh}}(E, 2\theta)$ for $\tau_{\text{incoh}}(E, E', 2\theta)$ without introducing appreciable systematic error, allowing τ to be factored out of the integrand in equation (4). Similarly, the FWHM of $S_{\text{incoh}}(k, \omega)$ (which, in the impulse approximation, is directly related to the width of the momentum distribution of the electronic ground state) is small compared to our required energy resolution, such that we can define a Compton-shifted energy variable $E^* = E + \Delta E$ and re-express (4) in approximate form:

$$I_{\text{incoh}}(E, 2\theta) = d\Omega_{\text{det}} N_{\text{atoms}} \frac{d\sigma_t}{d\Omega} \tau_{\text{coh}}(E, 2\theta) I_{\text{incident}}(E^*) \int_0^\infty dE' S_{\text{incoh}}(k, \omega). \quad (6)$$

The total scattered intensity, in units of photons/sr, is then

$$I_{total}(E) = d\Omega_t N_{atoms} \tau(E, 2\theta) \frac{d\sigma_t}{d\Omega} [I_{incident}(E) f(k)^2 S(k) + I_{incident}(E) \int_0^{\infty} dE' S_{incoh}(k, \omega)]. \quad (4.1)$$

Note that $\int_0^{\infty} dE' S_{incoh}(k, \omega) = N$ (the atomic number of the scattering species) in the high- k limit of the impulse approximation⁵¹ and takes on smaller values at lower momentum transfers; by comparison, $f(0)^2 = N^2$, and $S(k)$ is of order unity. Therefore the first (coherent) term in $I_{total}(E)$ dominates for heavier elements or for sufficiently small momentum transfers. In Fig. 4.6 (a) and (b) we compare $f(k)^2$ to the incoherent background scattering for the above-described model. These results lead us to expect that the background in an ED-XRD experiment will not substantially limit the ability to observe the desired coherent scattering.

4.2.3 II.C. Spectrometers for detection of ED-XRD

We now consider two different detection options. As shown in the schematic of Fig. 4.3, one or both of an x-ray CCD and a HOPG-based spectrometer may be used as energy-sensitive detectors. Simulated spectra for both follow in section III. Throughout the remainder of the paper the following experimental parameters are used: $d_{source} = 1$ cm; target dimensions (for both B and Al): 0.25 mm 0.25 mm 0.1 mm; scattering angle $2\theta = 135$ degrees. These choices will be motivated below.

The modeled CCD has a 2-dimensional square grid of 2200 x 2200 pixels, with a pixel edge length of 13.5 microns. A quantum efficiency of 1 is assumed. The optimal distance between the detector and the target is determined by the competing demands of high signal collection and high rejection of two-photon events on single pixels. We find it reasonable to balance these demands by selecting a single photon-hit regime with an expectation value p of 0.1 photon hits per pixel. At a given scattering angle and in the absence of addition of any special absorbers between the target and the CCD other than a Be filter for low-energy photon rejection, p is determined by the working distance of the CCD and the scattered

intensity off the target. The working distance is not a highly-constrained parameter; it must merely be sufficiently large that backgrounds from the high neutron flux and other stray radiations are likely to be substantially suppressed. An upper bound on target intensity arises from signal broadening due to the finite angular size subtended by the target relative to the backlighter. We require this geometrical broadening in momentum transfer, k , to satisfy $\Delta k/k < 0.05$, such that it is sufficiently small compared to the intrinsic scale of structure in $S(k)$. We label the angle subtended by the target $\Delta\theta_t$ and express the geometrical broadening in terms of it: $\Delta k/k = \cot \theta_t$. At $2\theta = 135$ degrees the maximal $\Delta\theta_t$ is approximately 0.1 radians, which corresponds to a sample length of 1 mm.

The task of presenting a modeled HOPG spectrum in a non-configuration-specific manner is complicated by the significant dependence of the spectrometer's energy range on several geometric parameters. Using the labeling of Fig. 4.4 and, as an example, the spectrometer geometry described by Fig. 4.5 (a), the differential in k for scattering from the target is

$$dk = \frac{k}{E} dE + \frac{k}{\delta(2\theta)} d(2\theta) = \frac{E}{c} (\sin(\theta) \cot \theta_B - \cos(\theta)) d\theta_B. \quad (9)$$

As a crystal of length l located a distance F from the target subtends an angle of approximately $(l/F) \sin \theta_B$, we can directly use (9) to calculate the range k covered by an analyzer crystal as a function of k , 2θ , and the choice of HOPG reflection. Fig. 4.5 illustrates this. Salient features of $\Delta k(k, 2\theta)$ are that it is asymptotically linear in k and depends weakly on 2θ everywhere except at low k .

That said, we can choose a typical configuration for an HOPG spectrometer and generate a detected spectrum that spans the entire range of k with which we are concerned. Conceptually, this is done by repeatedly rotating the crystal to different central θ_B to acquire narrow spectra in different ranges of k and then stitching together the resulting spectra. This spectrum, which is henceforth referred to as the “HOPG source spectrum”, does not represent a realistic data set, since acquiring it in a single shot would require prohibitively many analyzer crystals, but it does serve as a convenient compilation of the ensemble of possible experimental configurations; the exact choice of spectrometer configuration for a given experiment depends on some prior knowledge of the desired k range, as we discuss

below.

The modeled HOPG spectrometer is qualitatively similar to several instruments that have previously been fielded for x-ray Thomson scattering studies at OMEGA ⁵³⁻⁵⁵. For our modeled instrument, the HOPG diffractive element operates on the 002 reflection, has a mosaic spread of 0.3 degrees, is taken to be a flat square with side length $l = 12$ cm, and is located at a distance $F = 25$ cm from the target. The energy-dependent integral reflectivity of the HOPG is based on computed reflectivity curves ⁵⁶ for an HOPG crystal having a mosaic spread of 0.3 degrees. Denoting r as the peak reflectivity and ω as the FWHM of the reflectivity curve, the angular integral reflectivity, $\Delta\theta_B$, is approximately r ; equivalently, the integral reflectivity in energy units is $\Delta E = E \cot \theta_B \Delta\theta_B$. We define E_{\max} and E_{\min} as the maximum and minimum energies diffracted by the crystal. For isotropically-scattered photons with a fixed energy E between E_{\max} and E_{\min} the probability of reflection is $\eta = \Omega_0 \Delta E / (4 \pi (E_{\max} - E_{\min}))$, where $\Omega_0 = (l/F)^2 \sin \theta_B$ is the solid angle subtended by the crystal relative to the source (units of sr). Correspondingly, the detected spectrum resulting from I_{incident} on the target is $I_d(E) = 4\pi\eta dI_{\text{incident}}(E)/d\Omega = \Delta\theta_B(l/F)dI_{\text{incident}}(E)/d\Omega$. For reference, $\Delta\theta_B l/F = 7 \times 10^{-4}$ at 4 keV. It will be seen in the next section that the resulting net collection efficiency in a given achievable energy band is several orders of magnitude higher than that of the CCD.

4.3 III Results and discussion

There is good reason to believe, heuristically, that the above-described experimental configurations for ED-XRD should determine $S(k)$ with adequate statistics. Numerous past x-ray Thomson scattering experiments at laser plasma facilities have measured the inelastic portion of $S(k, \omega)$ using narrow pulse backlighters for illumination ^{25, 27, 28, 57-60}. Above 2 keV, a broad-band thermal backlighter has approximately 100 times the photon conversion efficiency of a short-pulse Cu K backlighter (Fig. 4.7); additionally, the elastic scattering cross section is typically larger than the Compton cross section, as discussed in section II and shown in Fig. 4.6 (a) and 5 (b). Thus, ED-XRD should offer vastly higher signal intensity

than (quasi-monochromatic) x-ray Thomson scattering using a metal-foil backlighter, and therefore better statistics.

Figure 4.2: (a): Liquid structure factor of B at 2400K. The original data (red) of Krishnan *et al.*⁴⁶ contains sharp unphysical noise; we therefore use the filtered interpolation (blue) of the data for $S(k)$ throughout this paper. (b): Equivalent theoretical curve for shock-compressed Al at electron density $n_e = 5.4 \cdot 10^{23} \text{ cm}^{-3}$ and temperature $T_e = 10 \text{ eV}$ based on Ma *et al.*³⁵ The curve is based on an approximate treatment of this system's atomic form factor (see the text for details).

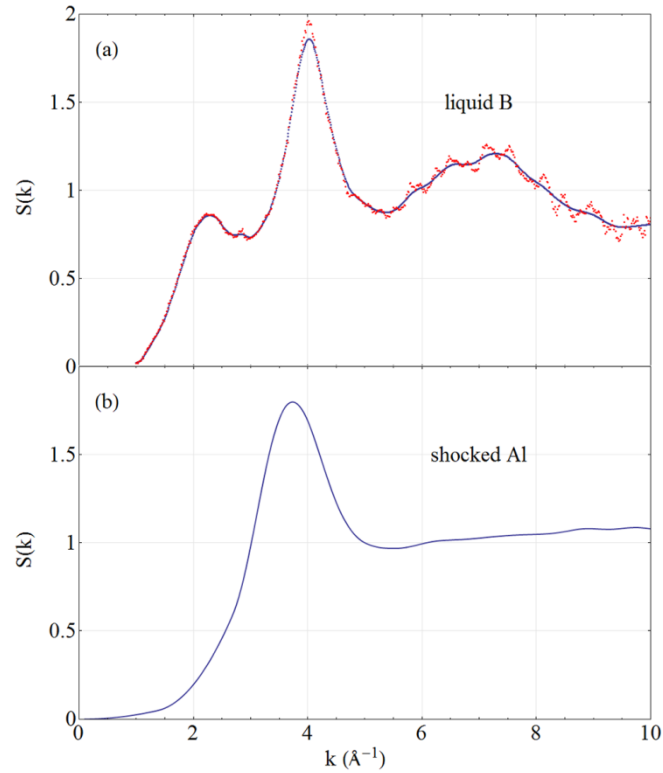


Figure 4.3: Schematic representations of (a) and (b) angle-dispersive x-ray diffraction, compared to (c) energy-dispersive x-ray diffraction (ED-XRD).

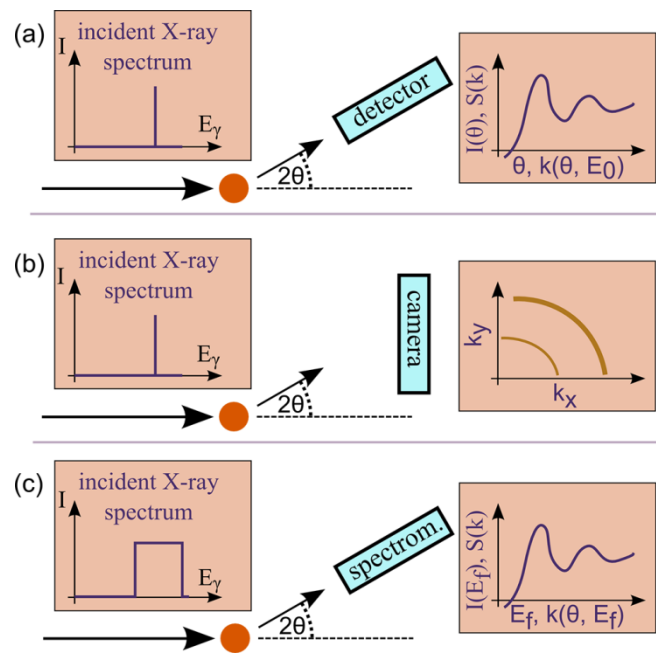


Figure 4.4: Experimental configuration for ED-XRD at a laser shock facility. A long pulse-driven CH capsule emits a broad thermal spectrum. Scattering from the target is observed using an HOPG spectrometer or a CCD in the single-photon hit regime.

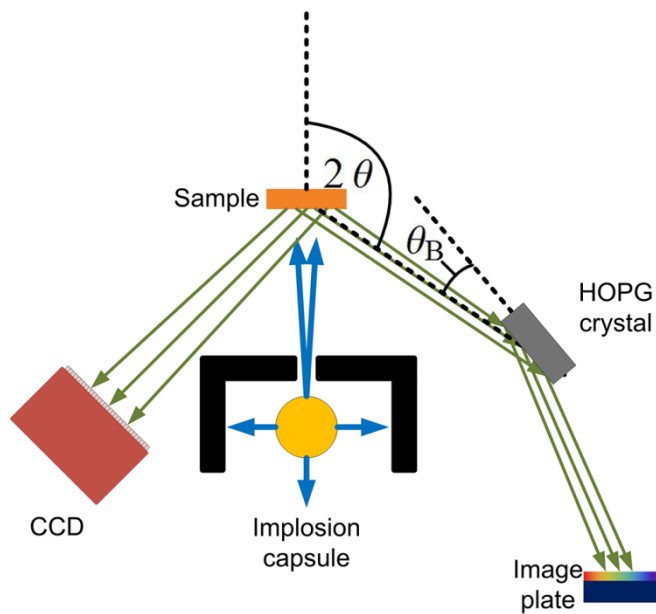


Figure 4.5: Range k in momentum transfer of scattering off the target probed by a small HOPG crystal per degree of its maximum subtended angle, θ_{\max} , for three spectrometer geometries that involve the same position (but different rotations) of the HOPG crystal: (a) the detector located in the target scattering plane and away from the axis passing through the backlighter and target, (b) the detector located in the target scattering plane and near the axis passing through the backlighter and target, and (c) the detector located such that it, the target, and the HOPG crystal define a plane perpendicular to the scattering plane. θ_{\max} denotes the maximum possible subtended angle of the HOPG crystal given a fixed spectrometer working distance F ; *i.e.*, for a crystal of length l , the maximum subtended angle is $\theta_{\max} = l/F$.

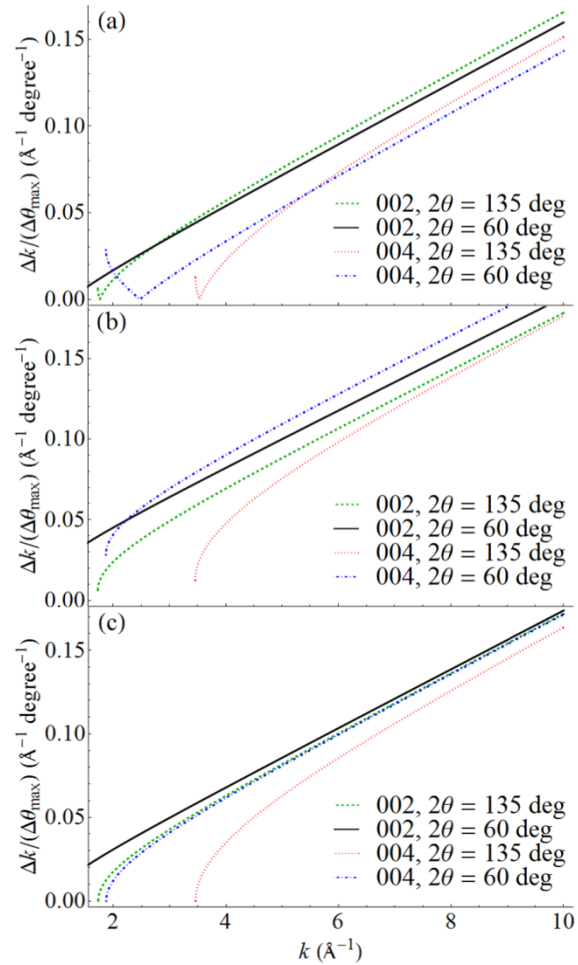


Figure 4.6: Elastic and inelastic contributions to the differential cross section of (a) boron and (b) aluminum. The elastic cross sections are based on tabulated values of $f(k)$. The inelastic differential cross sections, defined by $N_{\text{incoh}}(k) = \int_0^\infty dE' S(k, \omega')$, are based on $S(k, \omega')$ generated from f -summed, truncated Compton profiles in the impulse approximation. See the text for further details.

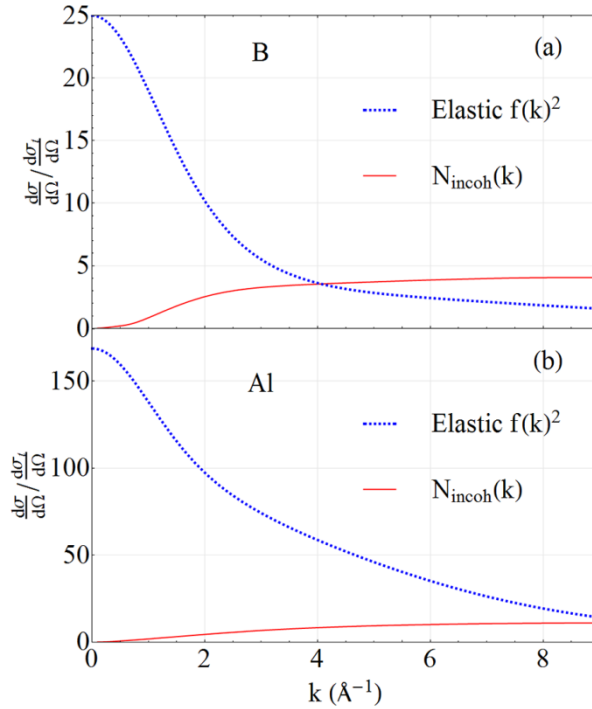
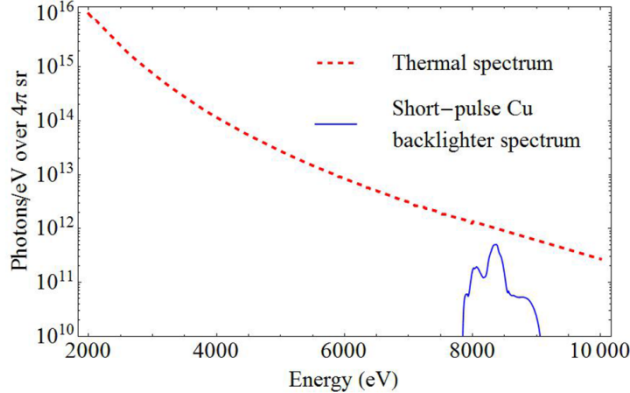


Figure 4.7: Red: experimental thermal backlighter spectrum from OMEGA ⁴³. Blue: a short-pulse Cu K backlighter spectrum, based on scaling of results from a lower energy laser system to a 2.5 kJ, 10 ps laser shot at OMEGA ^{44, 45}.



In Fig. 4.9 we present $I_d(E)$ defined in section II, filtered by a 20 m Be foil (to reject low-energy photons) for liquid boron acquired on a CCD alongside the equivalent HOPG source spectrum. The highlighted region of the HOPG source spectrum shows the energy range covered by a specific configuration: a 12-cm long HOPG crystal at distance $F = 25$ cm from the target, oriented such that the detected spectrum is centered on the main correlation peak in $S(k)$. This crystal size results in a solid angle subtended by the crystal similar to that in existing high-efficiency HOPG spectrometers ^{43, 61}. Figure 4.8 shows the CCD and HOPG spectra for shock-compressed Al in this same format. $S(k)$ reconstructed for B and Al is presented in Figs. 4.10 and 11, respectively. In both these figures the k -range probed by the specific spectrometer configuration is highlighted. All reconstructed $S(k)$ curves, including those without background subtraction, show a well-defined correlation peak. Note that the uncorrected curves overshoot the experimental $S(k)$ at large k ; this is a result of the monotonically-increasing Compton background (as well as double-counts, for the CCD). This background decreases relative to the XRD signal for larger atomic numbers, as seen by comparison of Figs. 4.10 and 11. The HOPG source spectrum exhibits excellent statistics (error bars < 2 percent) relative to the CCD over the entire plotted energy range. While

deteriorating at high energy, the CCD spectrum also has good statistics (error bars < 5 percent) below 4.5 keV.

The relative merits of the two detectors are dictated by particular features of the ED-XRD configuration and the spectrum probed. Despite the substantially better energy resolution of an HOPG spectrometer compared to a Fano-noise limited CCD, energy resolution is a poor criterion for comparison: at 135 degrees scattering angle, the k -width of features in $S(k)$ corresponds to a width in energy greater than 500 eV, substantially larger than the resolution of both the CCD and the HOPG spectrometer. Instead, the leading limitation on data quality is shot noise at high k due to the sharp decay of the source spectrum intensity with increasing energy.

The latter limitation is severe only for the CCD, (1) because of vastly lower overall counts and especially (2) because the intense low-energy portion of the incident spectrum is ‘echoed’ as double-counts at higher energy. In simulated CCD spectra the double-count contribution to the detected spectrum outweighed the single-count contribution above 5 keV. This double-count noise cannot be reduced by varying p : in the single photon-hit regime, the number of double-hits on single pixels scales as p^2 ; the associated Poisson noise scales as p . Single photon counts also scale as p ; as a result, above 5 keV varying p has little effect on the signal-to-noise (*i.e.* single-to-double-count) ratio. It is instead highly preferable to carry out an ED-XRD experiment in near-backscatter geometry, such that the range of k in which $S(k)$ has structure is probed by a lower-energy region of the backscatter spectrum. In fact, the only means of significantly improving data quality on a single hit CCD are (1) using a detector with more pixels to improve statistics, and (2) moving the detector closer to backscatter.

The two spectrometer types offer a variety of configurations adapted to experimental situations in which different k -ranges need to be probed. If the goal is to locate the main correlation peak in $S(k)$, a single-HOPG crystal spectrometer is a viable option (illustrated, as mentioned above, in Figs. 4.10 and 4.11). On the other hand, if the scientific goal requires a significantly wider k -range, then a CCD detector in single photon counting mode, multiple

HOPG analyzer crystals, or both are necessary. Despite the CCD's relatively poor signal to noise ratio, there is substantial motivation for performing ED-XRD using both spectrometer types if the full k range is desired. In such a dual configuration the CCD would provide low-noise data up to approximately 4.5 keV with one or more HOPG spectrometers covering the remainder of the energy spectrum, corresponding to a reduced range of θ_B from 21 to 49 degrees, for which a modest number of analyzer crystals would be required.

The above results establish single-shot ED-XRD as a viable method for use at OMEGA, even for systems with only liquid-like, isotropic short-range order; this observation clearly extends to fine, isotropic polycrystalline systems where the structure in $S(k)$ can only be sharper. We note that pump laser energy is 30 times larger at NIF than at OMEGA and that the ratio of backlighter fluences exceeds that factor due to the higher backlighter electron temperature at NIF⁴¹. Consequently, ED-XRD is also viable at NIF where the higher backlighter fluence may allow a substantial reduction in solid angle subtended by an HOPG spectrometer, compared to present calculations. This would in turn allow incorporating a larger number of spectrometers in a single diagnostic module. CCD-based studies at NIF are also, in principle, viable but may run into technical difficulties related to neutron backgrounds or difficulty in shielding from electromagnetic pulses.

Figure 4.8: Photon-energy histograms on CCD and HOPG spectrometers for shock-compressed Al at electron density $n_e = 5.4 \cdot 10^{23} \text{ cm}^{-3}$ and temperature $T_e = 10 \text{ eV}$, using Ma *et al.*'s best-fitting theoretical model to their experimental results for $f(k)^2 S(k)^{35}$, and assuming $f(k)$ of ambient Al. The expectation value of photon counts/pixel on the CCD is $p = 0.1$. The energy range of a specific HOPG configuration using a 12-cm long HOPG analyzer is denoted by the shaded region, the width of which corresponds to the spectrometer configuration of Fig. 7 (a). The spectrometer's focal length is 25 cm, and the length of the crystal in the non-energy dispersive orientation is 12 cm; both spectrometers are positioned at $2\theta = 135 \text{ deg}$. A 20-m thick Be foil is used to reject low-energy photons. Error bars in the HOPG histogram are smaller than 1% (not shown).

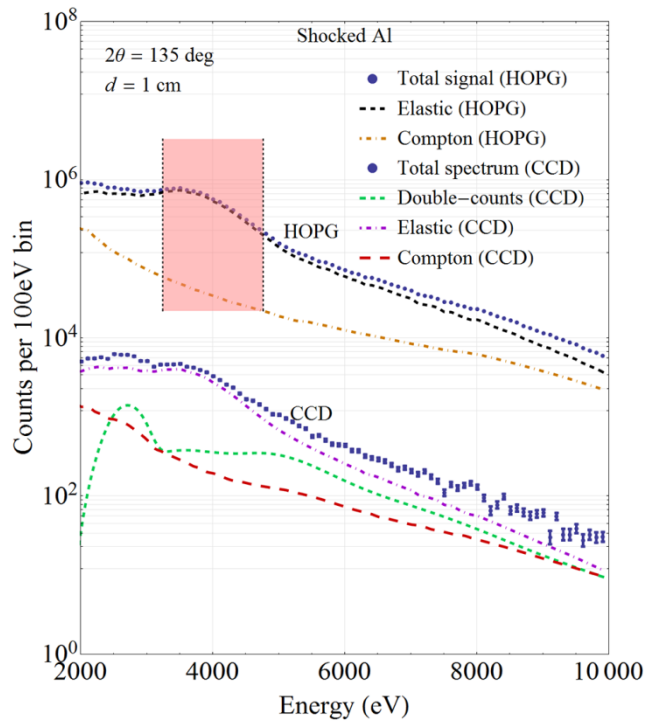


Figure 4.9: Photon-energy histograms for energy-dispersive diffraction spectra of liquid boron on CCD and HOPG spectrometers. The expectation value of photon counts/pixel on the CCD is $p = 0.1$. The energy range of a specific HOPG configuration using a 12-cm long HOPG analyzer is denoted by the shaded region, the width of which corresponds to the spectrometer configuration of Fig. 7 (a). The spectrometer's focal length is 25 cm, and the length of the crystal in the non-energy dispersive orientation is 12 cm; both spectrometers are positioned at $2\theta = 135$ deg. A 20-m thick Be foil is used to reject low-energy photons. Error bars in the HOPG histogram are smaller than the size of the symbols.

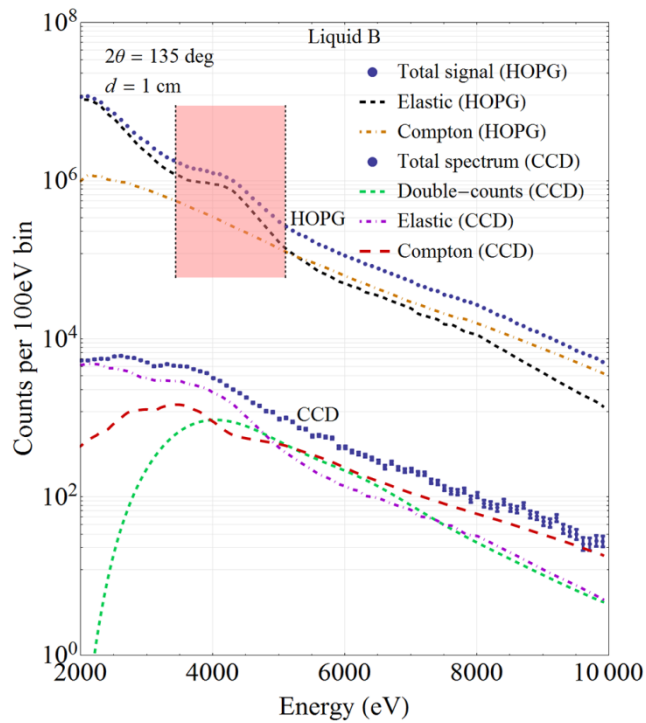


Figure 4.10: $S(k)$ for liquid boron reconstructed from simulated energy-dispersive spectra of Fig. 8 for (a) an HOPG spectrometer and (b) a CCD, with and without subtraction of Compton background and photon double-counts. Data bin size is 100 eV. The shaded k -range in the HOPG spectrum corresponds to the spectrometer configuration described in the text, and is centered about the main correlation peak in $S(k)$.

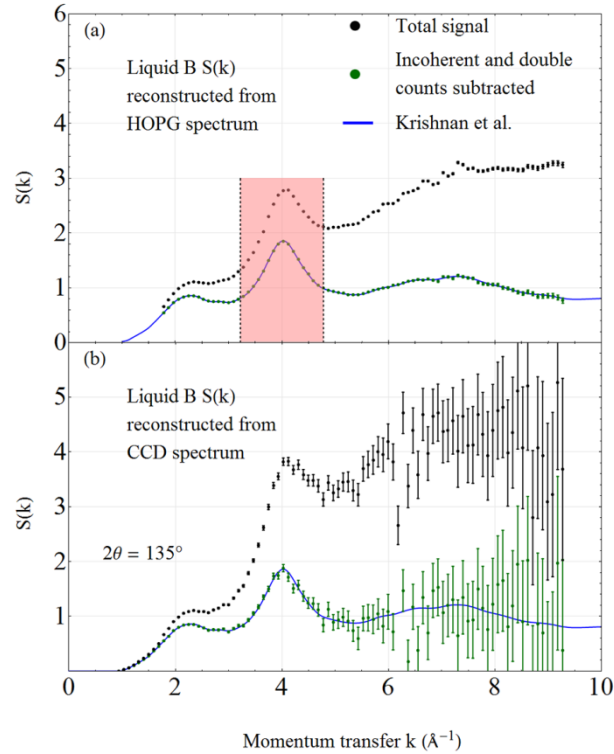
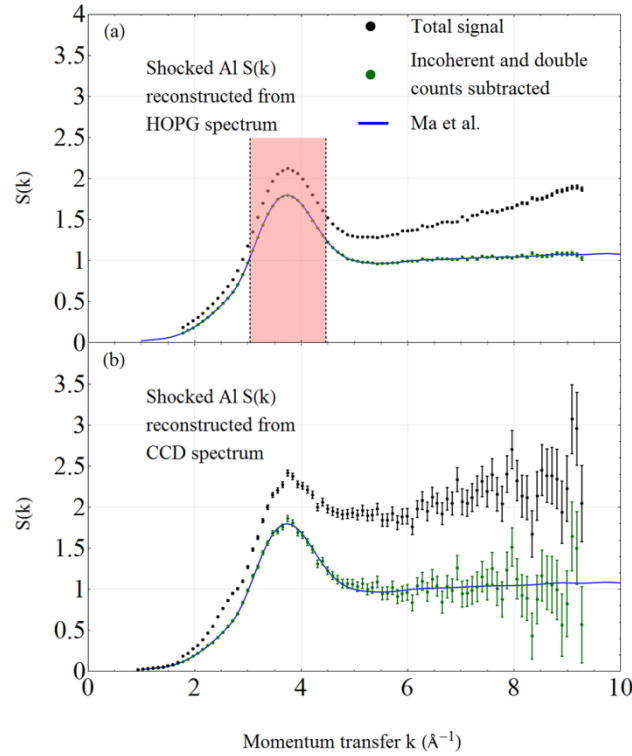


Figure 4.11: In blue: X-ray structure factor $S(k)$ for shock-compressed Al computed from Ma, *et al.*³⁵. Overlaid with $S(k)$ reconstructed from the spectra of Fig. 9 for (a) an HOPG spectrometer and (b) a CCD. The data bin size is 100 eV. The shaded k -range in the HOPG spectrum corresponds to the spectrometer configuration described in the text and is centered about the main correlation peak in $S(k)$.



4.4 IV. Conclusions

We report a photometric study of the viability of single-shot investigation of the isotropic static structure factor $S(k)$ in experiments using a broadband x-ray backlighter as the source for energy-dispersive x-ray diffraction (ED-XRD). The results are extremely favorable, and indicate that single-shot ED-XRD can be used at OMEGA or NIF. A standard scientific-grade x-ray CCD camera operating in single-photon counting mode suffices for many studies, but exhibits degraded performance at high momentum transfers due to the rapid decrease of incident flux at higher photon energy. On the other hand, a typical HOPG-based wavelength dispersive spectrometer has exceptional count rates in any selected k range, but its limited energy range may require either the use of multiple spectrometers or of a single compound spectrometer having multiple analyzer crystals.

4.5 Acknowledgements

We thank Brian Mattern, Tilo Doeppner, Philip Nilson, Barukh Yaakobi, Christian Stoeckl, Yuan Ping, Justin Wark, and Andrew Higginbotham for helpful discussions. This work was supported by the US Department of Energy, Office of Science, Fusion Energy Sciences and the National Nuclear Security Administration, through grant DE-SC0008580.

4.6 References

- 4.6.1 ¹ J. D. Lindl, P. Amendt, R. L. Berger, S. G. Glendinning, S. H. Glenzer, S. W. Haan, R. L. Kauffman, O. L. Landen, and L. J. Suter, *Physics of Plasmas* 11, 339 (2004).
- 4.6.2 ² E. I. Moses, *Nuclear Fusion* 49, 104022 (2009).
- 4.6.3 ³ F. Langenhorst, M. Boustie, A. Migault, and J. P. Romain, *Earth and Planetary Science Letters* 173, 333 (1999).
- 4.6.4 ⁴ J. Gattacceca, M. Boustie, E. Lima, B. P. Weiss, T. de Reseguier, and J. P. Cuq-Lelandais, *Physics of the Earth and Planetary Interiors* 182, 42 (2010).
- 4.6.5 ⁵ H. Takabe, et al., *Plasma Physics and Controlled Fusion* 50, 124057 (2008).
- 4.6.6 ⁶ L. O. Silva, M. Marti, J. R. Davies, R. A. Fonseca, C. Ren, F. S. Tsung, and W. B. Mori, *Physical Review Letters* 92, 015002 (2004).
- 4.6.7 ⁷ B. A. Remington, R. P. Drake, H. Takabe, and D. Arnett, *Physics of Plasmas* 7, 1641 (2000).
- 4.6.8 ⁸ H.-S. Park, et al., *High Energy Density Physics* 8, 38 (2012).
- 4.6.9 ⁹ M. Koenig, et al., *Physics of Plasmas* 13, 056504 (2006).
- 4.6.10 ¹⁰ A. Macchi, M. Borghesi, and M. Passoni, *Reviews of Modern Physics* 85, 751 (2013).
- 4.6.11 ¹¹ G. Gregori, et al., *Nature* 481, 480 (2012).
- 4.6.12 ¹² F. Fiuzza, R. A. Fonseca, J. Tonge, W. B. Mori, and L. O. Silva, *Physical Review Letters* 108, 235004 (2012).
- 4.6.13 ¹³ F. Dollar, et al., *Physical Review Letters* 110, 175002 (2013).
- 4.6.14 ¹⁴ K. U. Akli, et al., *Physical Review Letters* 100, 165002 (2008).
- 4.6.15 ¹⁵ B. K. F. Young, et al., *Review of Scientific Instruments* 69, 4049 (1998).
- 4.6.16 ¹⁶ K. Oades, A. Evans, G. Slark, J. Foster, R. Eagleton, and E. Clark, *Review of*

Chapter 5

X-RAY FREE ELECTRON LASER-BASED STUDIES OF WDM

5.1 X-ray Free Electron Lasers

XFELs produce radiation of unprecedented brilliance (10 orders of magnitude higher than undulator radiation from third-generation synchrotron sources), full transverse coherence, pulse durations as short as 10 fs. This combination of capability far exceeds that possible with third-generation light sources and opens new frontiers in imaging and the interrogation of ultrafast processes in materials science and biology (cites). In this section we give an overview of the technology and its range of applications in the study of HED states of matter.

5.1.1 Physics of XFELs

To describe the FEL interaction, we first consider the generic case of radiation emission from undulators, the type of insertion device used in both XFELs and the highest-brilliance beamlines at third-generation synchrotron light sources.

A simple time-of-flight argument may be used to obtain an intuitve understanding of radiation by a single electron in an undulator. A radiation wavefront co-propagating with an electron undergoing forced transverse undultion with a (longitudinal) period λ_u will move ahead of the electron. Constructive interference of the radiation field produced by successive undulationso of the electron will occur at discrete values of the electromagnetic wavelength, λ_n , satisfying $\lambda_n = \lambda_1/n$, where λ_1 is defined as the fundamental resonant wavelength. The time t taken for an electron to propagate one undulator period λ_u at speed v_z ($t = \lambda_u/v_z$) is equal to that needed for a resonant wavefront travel the distance $\lambda_u + n\lambda_n$. Equating the propagation times for the wavefront and electron yields the relation (cite McNeil et al.)

$$\lambda_n = \frac{\lambda_u}{n} \left(\frac{1 - v_z/c}{v_z/c} \right). \quad (5.1)$$

More detailed treatment shows that, in the case of a helical undulator, only the fundamental mode has strong on-axis emission. (cites)

This describes the narrow spectral width of undulator radiation and the coherent addition of radiated wave amplitudes by a single electron over the length of an undulator. This constructive interference accounts for the much higher brilliance of radiation produced by an undulator, compared to a wiggler or bending magnet.

At a synchrotron light source electrons in a bunch have uncorrelated positions, and the undulator spectrum is therefore a simple incoherent sum of the emission of all individual electrons passing through it. An XFEL improves on this by creating a positional ordering electrons into ‘micro-bunches’ separated from one another by the radiation field wavelength. The coherent emission from multiple micro-bunches with N_b electrons each would be equivalent, in an idealized case where the micro-bunch dimension were much smaller than the x-ray wavelength, to that from point-like charges of magnitude eN_b , with a resulting factor of N_b^2 enhancement in brilliance relative to that from an incoherently-emmitting electron bunch. (cite)

Electrons in an undulator experience a longitudinal force from the radiation field that is modulated by its period. The consequent bunching of electrons with a period equal to the X-ray wavelength is a self-reinforcing process referred to as self amplified stimulated emission (SASE) (cites). Crucially, the occurrence of SASE requires a sufficiently strong initial radiation field, which third-generation synchrotron storage rings—having 100 ps-duration electron bunches—are not capable of producing. The key feature of an XFEL is its use of a linear accelerator to produce very compact electron bunches with sufficient electron density to bootstrap SASE.

5.1.2 XFELs and WDM generation

Maximum single-shot flux densities available at XFELs exceed 10^4 J/cm^2 , sufficient to produce HED states with per atom energy deposition over 100 eV with uniform, volumetric heating. (TODO: how about better-focusing optics?). Because XFEL radiation is monochromatic it can be used as a probe for nearly all X-ray diagnostics useful for determination of the state variables of WDM, with the notable exception of XAS. Taken together, these characteristics make XFELs ideal for both producing and probing short-timescale dynamics of HED matter. (cites)

One of the most significant recent advances in XFEL technology is the generation of two-color pairs of hard X-ray pulses. This is done by production of time-delayed twin electron bunches (achieved either by illuminating the source cathode with a train of two laser pulses, or using an emittance spoiler) (cite Marinelli et al., Lutman et al.) and the addition of magnetic chicanes that introduce a time-energy correlation in the electron beam before the bunches' entry into the undulator. At the LCLS, two color X-ray pulse energies up to the mJ level—approaching the values of single-pulse SASE—have been demonstrated. X-ray arrival time delays are variable between 30 and 125 fs, and maximum color separations of up to 1.9 % of the photon energy have been demonstrated (cite Lutman).

Operating an XFEL in two-color mode opens up significant possibilities for truly time-resolved probes of WDM. In single-pulse operation the time evolution of an XFEL-heated target can, to some extent, be studied by variation of pulse duration. However, such a study yields a signal that, for each XFEL configuration, is a convolution over all states the target transitioned as it heated throughout each pulse's duration. In contrast, two-color operation offers two advantages:

- Temporal resolution: by choosing pulse energies that straddle an absorption edge of a chemical filter (in the case of an XRD probe), or of the target itself (in the case of an XES probe), signal from the pump pulse can be rejected. Varying pump-probe delay thus allows measuring the sample's temporal response to the pump.

- Uniformity of probed state: By additionally reducing the intensity of the probe relative to the pump, one can ensure that the probe is only a weak perturbation to the heated state generated by the pump.

The possibility of clean time-resolved studies of XFEL-generated WDM is quite attractive, given that the electronic relaxation cascade in a heated solid consists of several partially-overlapping stages of uncertain durations: i.e. collisional ionization by hot electrons; stimulation of long-wavelength collective excitations; and damping of large-q excitations through production of electron-hole pairs. Lack of prior information in the physics under scrutiny emphasizes the need for the highest-information diagnostics available.

5.2 HED physics at XFEL facilities

5.2.1 Early experiments

Initial efforts at FLASH and LCLS, the first free electron lasers operating at short wavelengths, have been focused on the creation of exotic states and the exploration of interactions of high-intensity hard X rays with matter. Thomas et al. and others have studied the Coulomb explosion of noble gas clusters, including the dynamics of nanoplasma formation (cite Thomas et al.). Using intense XFEL radiation Young et al. demonstrated the production of fully-stripped Ne atoms as well as induced X-ray transparency in ‘hollow’ atoms, a manifestation of ‘beating’ the Auger clock though ionization rates faster than the recombination times of core electrons. Their modeling of X-ray/atom interactions using a rate-equation based approach yielded predictions of atomic populations consistent with electron spectroscopy, providing an early validation of the applicaton of population kinetics codes such as SCFLY to the simulation of XFEL-matter interactions. (cite Young, maybe cite SCFLY paper and check that it wasn’t originally written with XFEL simulation in mind).

Nagler et al. have similarly demonstrated saturable absorption of an L-shell transition in Al, where the long lifetime of 2p vacancies allowed complete depopulation within a single XFEL pulse at incident intensities on the order of 10^{16} W/cm² and 92 eV photon energy.

(cite Nagler). This experiment was the first demonstration of a bulk, crystalline material in a high-energy density (and highly non-thermal) electronic configuration. (check that this is true).

5.3 Scientific Directions

5.3.1 Time dynamics of WDM states

The ability of XFELs to produce such transient HED states invites basic questions about the creation of these states and their temporal evolution. Population kinetics codes such as SCFLY are a well-established tool to simulate the electronic evolution of an XFEL-heated material, but such codes are based on atomic physics treatments and cannot be all-encompassing, as they omit solid-state electronic structure as well as the interaction of electrons with the lattice of a solid-density system. Hau Riege et al. have examined electron-ion dynamics during heating by a single XFEL pulse, using comparison of Bragg diffraction from heated graphite with molecular dynamics simulation to quantify perturbation of the atomic lattice. They have identified melting of the graphite lattice within 40 fs pulses—far shorter in duration than the ps-timescale of electron-phonon coupling indicating an ultrafast phase transition. We revisit Hau-Riege’s conclusions in a different light in section (which section?), but their work pertinently demonstrates that the characterization of even coarse-grained quantities such as lattice thermalization timescales gives insight into the new physical regimes that XFELs are capable of producing and probing.

Similar observations apply to electron-electron thermalization in a solid, where damped collective excitations (ie. plasmons) may play a significant role as a bottleneck stage between absorption of XFEL photons and eventual thermalization of atomic electrons (cite Egerton, Sorini, maybe dig up cites from HEF paper).

As alluded to above, two-color XFEL operation is a promising potential means of addressing these questions.

5.3.2 Tests of Finite- T electronic structure

The output quantity of a density functional theory (DFT) simulation is real-space charge density. At the same time, the real-space charge distribution of a crystalline XFEL target material can be interrogated via X-ray diffraction, which samples the unit cell structure factor at momentum transfers corresponding to vectors of the reciprocal lattice. Because a material's lattice typically does not have sufficient time to respond to the changing electronic configuration over the duration of an XFEL pulse, XRD from WDM states produced by an XFEL can be directly compared to predictions of frozen-lattice finite-temperature DFT calculations.

This observation has led Valenza et al. to generate predictions of the consequences of XFEL heating on the intensities of Bragg peaks in several materials using DFT calculations in VASP (cite Valenza et al.). They have shown that the information in the XRD signal is sufficient for discrimination between competing theoretical predictions, provided the XRD measurement is performed over a sufficiently wide range of momentum transfers. Valenza et al. demonstrate strong testable signatures of condensed-phase effects in each of LiF, graphite, diamond, and Be as a result of heating to temperatures on the order of 10 eV. A summary of their results is reproduced in Fig. ??.

The capability to test predictions of finite-temperature electronic structure models is a unique feature of XFEL-based experiments. We will explore the topic in some more detail in section (reference section), where we have the opportunity to apply it to experimental data.

5.4 Design of an XFEL heating experiment

One can identify several experimental desirata shared by the majority of XFEL-based studies of WDM wherein the primary probe is X-ray diffraction:

- Maximization of information in the XRD signal
- Effective target heating so as to maximize the accessible range of energy densities

- Time resolution

Each of these can be achieved in one or more ways. Respectively:

- As alluded to in section (reference section), better-constrained estimates of real space charge density can be obtained by sampling a larger number of Bragg reflections. This requires probing a large momentum transfer range, made possible by using a high incident photon energy.
- In bulk samples, a high density of deposited energy requires matching the incident photon energy to a value at which the photoelectric absorption cross section is large. In section (reference section) we will introduce an alternate approach based on the design of structured targets that relaxes this constraint on incident photon energy.
- Wherever a single XFEL pulse is used to both heat and probe a sample, a limited degree of sensitivity to the time-evolution of transient states can be had by varying time duration. Two-color XFEL operation, however, is much more attractive. However, it suffers from tradeoffs: most notably experimental complexity and reduced signal, due to the need for attenuation of the probe pulse relative to the pump.

These goals, and the tradeoffs that accompany them, are important context for both the experimental work described in the next section and the modeling-based exploration of experimental technique discussed in section (reference section).

5.5 Experimental Work

In the following I describe several experimental results arising from two beam runs at the Matter of Extreme Conditions (MEC) endstation at the Linac Coherent Light Source (LCLS) in June of 2014 and January of 2016. The studies conducted addressed questions about the relative magnitudes, and time scales, of lattice and electronic heating in various solids, mainly

metal oxides. The primary diagnostic was XRD, with which we measured changes in electronic charge distribution as a function of incident flux, with the eventual goal of comparison to finite-T condensed matter electronic structure theory, as described in (reference section). The secondary diagnostic—used in a subset of the studies—was a von Hamos X-ray emission spectrometer with a highly annealed pyrolytic graphite (HAPG) analyzer crystal and 9 eV energy resolution, with which heating-induced line shifts and changes in valence-level emission were measured.

Throughout these measurements the XFEL beam was brought to a focus at the sample location using a stack of Be lenses. Flux incident on-sample was altered through a combination of beam attenuation and variation of the focal spot diameter between minimum and maximum values of 2 and 58 microns. XRD data was collected on a quad CSPAD solid state detector downstream from the sample (cite CSPAD paper).

In samples wherein the signal was weak compared to time variations in the area detector pedestal values, additional processing was performed in order to reconstruct signal incident on the detector. This is described in more detail in section (reference section), which details analysis and modeling of electronic heating based on an XRD dataset of XFEL-heated MgO.

5.5.1 Testing Lattice Thermalization in XFEL-heated Solid State Systems

Fig. 5.4 (a, b) displays the progression of Bragg peak intensities as a function of incident flux for two different Fe_3O_4 targets heated by 45 fs XFEL pulses. It demonstrates monotonic declines in the intensities of all Bragg peaks as a function of flux density, with the exception of the 222 peak, which rises to a maximum at the second-lowest flux density point before declining.

It is straightforward to evaluate the relative contributions of thermalization of electronic and lattice degrees of freedom to the XRD signal’s evolution as a function of heating. The main distinguishing feature between these two components is that the latter causes Debye-Waller quenching of Bragg peak intensities that is approximately proportional to $e^{-q^2\langle u^2 \rangle}$, where q is momentum transfer and u is atomic displacement. Fig. 5.5 compares the experi-

mental data to this Debye-Waller progression for several different values of RMS atomic displacement. The experimental data shows a complete lack of Debye-Waller-like q -dependence in Bragg peak intensities at high levels of heating, signifying that the XRD response is strongly dominated by reorganization of electronic charge density within a unit cell.

The electronic response of Fe_3O_4 to XFEL heating can be further interpreted through comparison of the data to a simple atomic form factor-based model of ionization (the model is described more specifically in section (reference section)). We find that the model reproduces the anomalous rise in intensity of the 222 reflection (reference figure) via a loss of destructive interference between the valence wavefunctions of O and Fe as both are simultaneously ionized. (cite paper in preparation).

5.5.2 Observation of Nonlocal Heat Transport in Nanophase Fe_3O_4

5.5.3 XES Signatures of Valence Electron Delocalization in XFEL-heated Fe_3O_4

Note to readers of thesis draft: The above two sections belong to a manuscript currently in preparation, and will be added later, reorganized into a separate chapter.

Figure 5.1: Operation of an x-ray free electron laser (cite McNeil). Electrons enter the undulator with random phases and originally emit uncoherent radiation at the undulator's resonant wavelength. As the electrons propagate, random fluctuations in the radiation field causes them to bunch at the resonant wavelength and emit coherently.

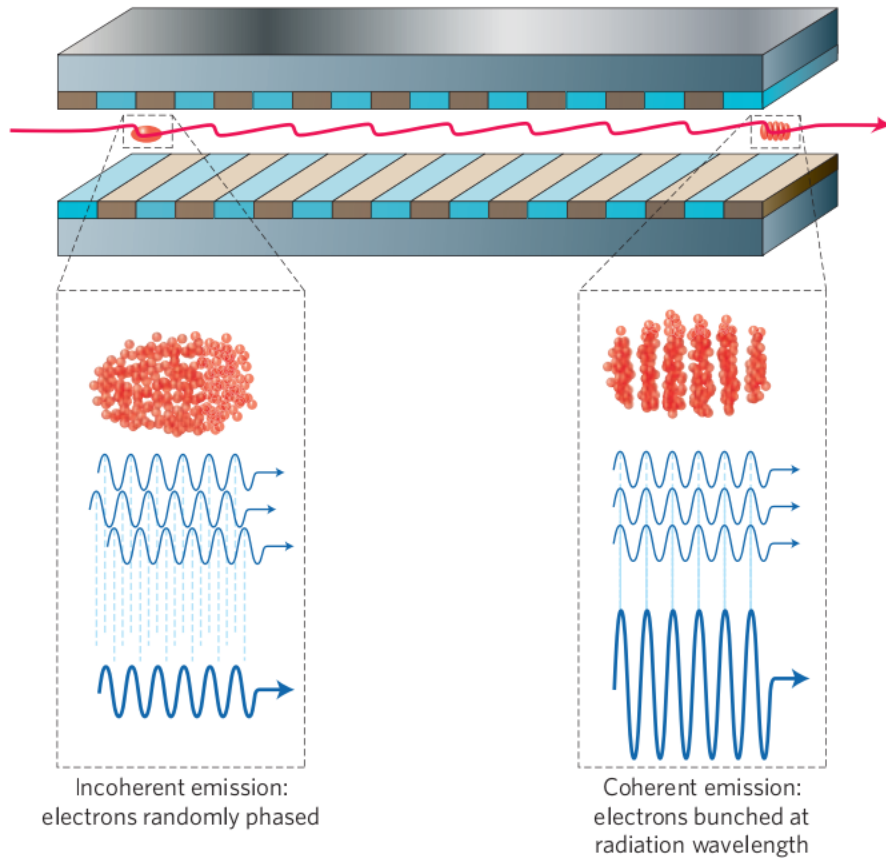


Figure 5.2: Schmematic representation of a two-color XFEL x-ray diffraction measurement wherein a chemical filter is used to reject pump photons.

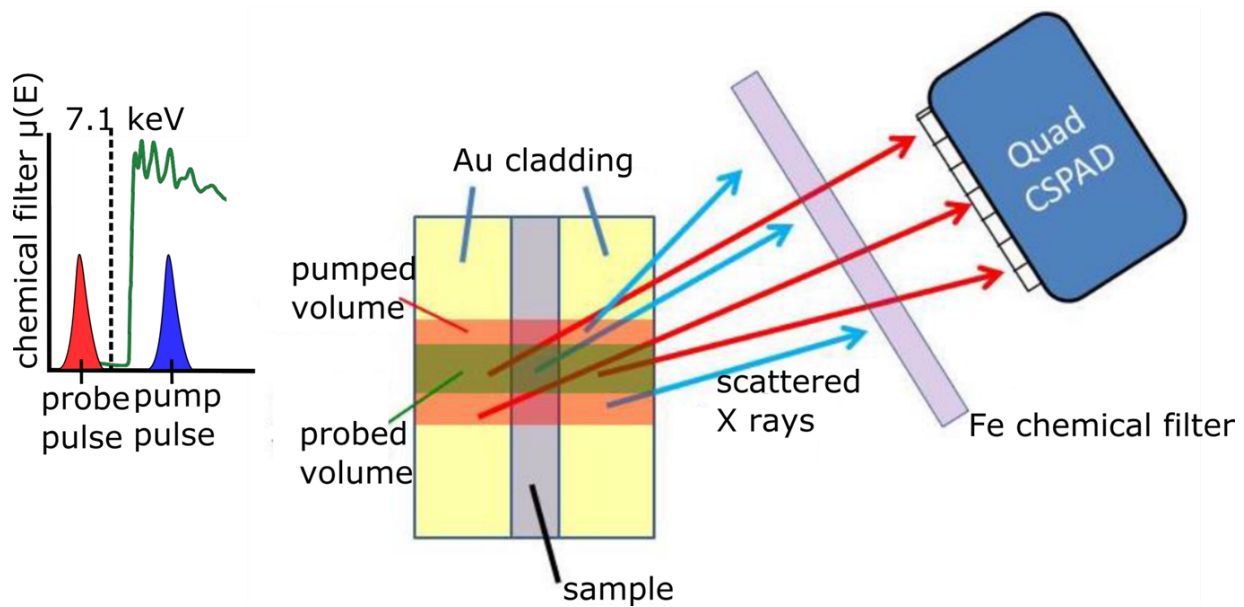


Figure 5.3: Left: intensity of diffraction peaks as a function of temperature, using finite-temperature DFT calculations in VASP; right: intensity of diffraction peaks as a function of ionization, using an atomic form factor-based model of ionization. The four simulated compounds are (from top to bottom) LiF, diamond, graphite, and Be. Taken from Valenza et al. (cite Valenza et al.)

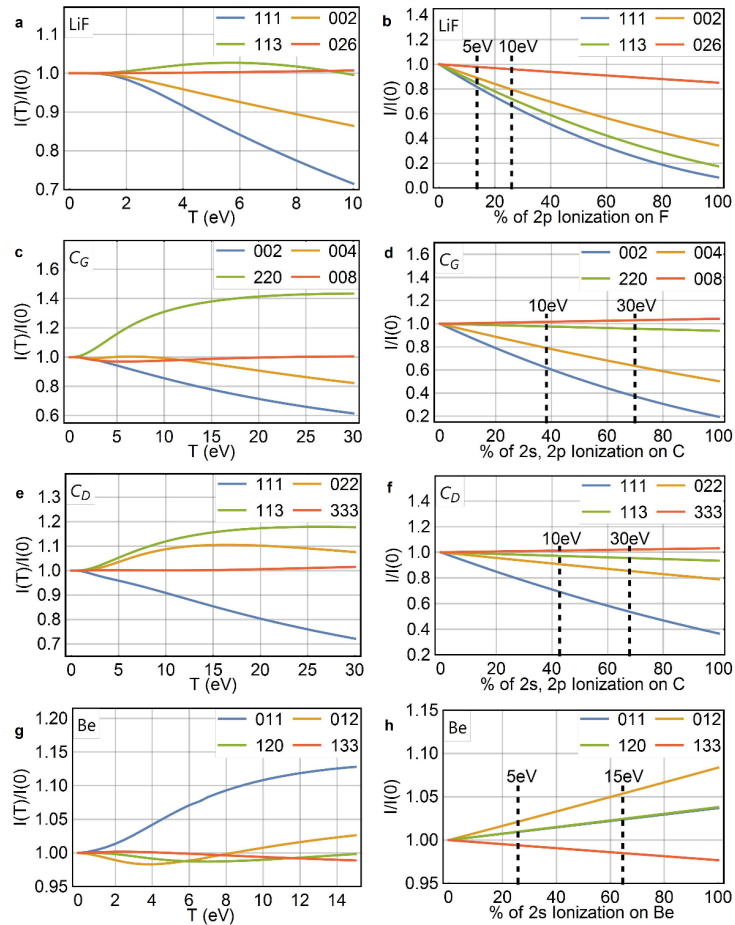


Figure 5.4: Progression of Bragg peak intensities as a function of incident x-ray flux density for (a) microphase and (b) nanophase Fe_3O_4 , normalized to the intensity of the lowest-flux density point. (c) displays the progression of Bragg peak intensities as a function of electron ionization in an atomic form-factor based model wherein the Fe 3d and O2p electrons are first ionized, followed by the more tightly-bound Fe 4s and 3p, and O 2s electrons. (cite Fe_3O_4 paper in preparation)

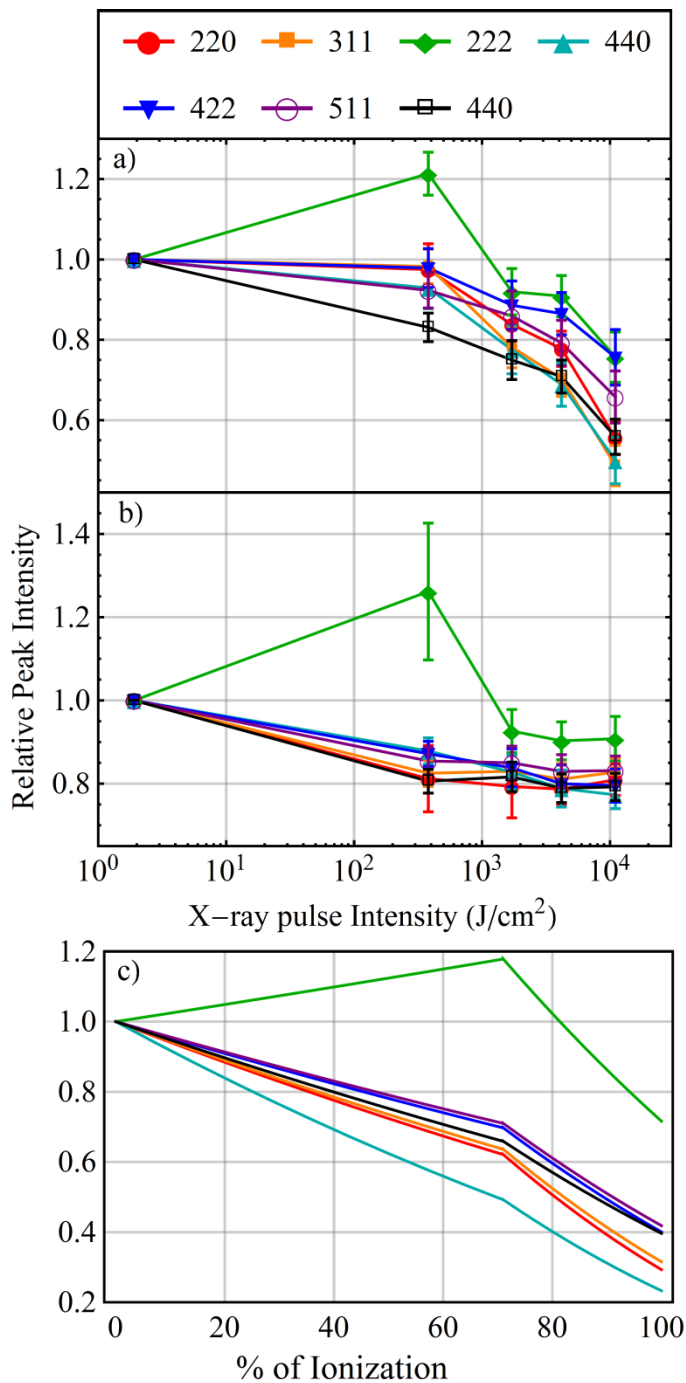
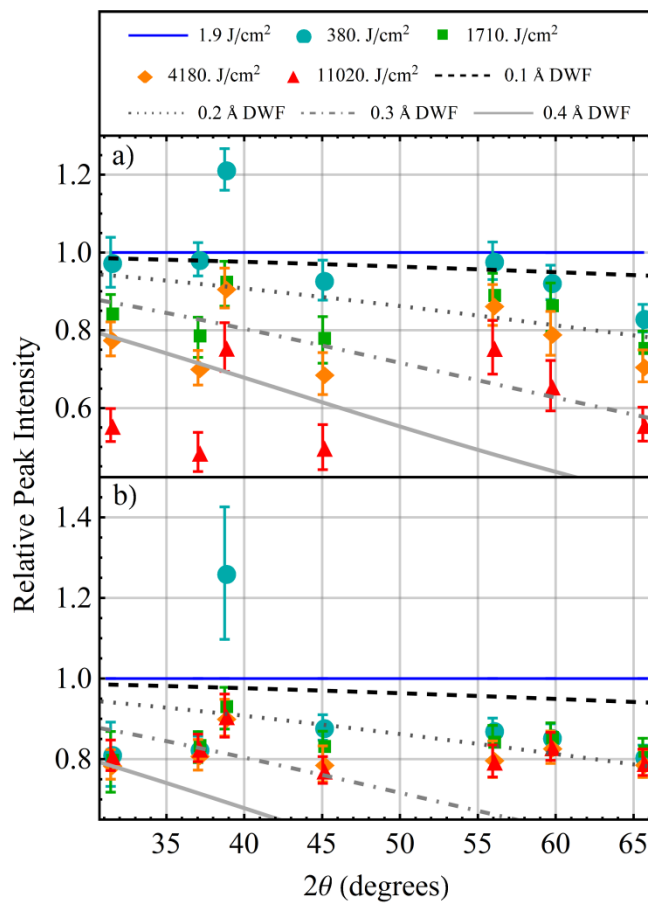


Figure 5.5: Same data as Fig. 5.4 plotted against Bragg angle and compared with the Debye-Waller factor for several values of RMS atomic displacement. (cite fe3o4 paper in preparation)



Chapter 6

FINITE-T CHARGE TRANSFER IN MGO UNDER EXTREME X-RAY HEATING: A CRYSTAL OF HOLLOW ATOMS

Note to readers of thesis draft: This chapter belong to a manuscript currently in preparation, and will be added later.

Chapter 7

A DISPOSABLE X-RAY CAMERA BASED ON MASS PRODUCED CMOS SENSORS AND SINGLE-BOARD COMPUTERS

Oliver R. Hoidn and Gerald T. Seidler

Physics Department, University of Washington, Seattle WA 98195

7.1 Abstract

We have integrated mass-produced commercial complementary metal-oxide-semiconductor (CMOS) image sensors and off-the-shelf single-board computers into an x-ray camera platform optimized for acquisition of x-ray spectra and radiographs at energies of 2 - 6 keV. The CMOS sensor and single-board computer are complemented by custom mounting and interface hardware that can be easily acquired from rapid prototyping services. For single-pixel detection events, i.e., events where the deposited energy from one photon is substantially localized in a single pixel, we establish $\sim 20\%$ quantum efficiency at 2.6 keV with ~ 190 eV resolution and a 100 kHz maximum detection rate. The detector platform's useful intrinsic energy resolution, 5-m pixel size, ease of use, and obvious potential for parallelization make it a promising candidate for many applications at synchrotron facilities, in laser-heating plasma physics studies, and in laboratory-based x-ray spectrometry.

7.2 Introduction

The performance of a wide range of contemporary applications of x-ray methods are contingent upon the capabilities of x-ray imaging sensors. Examples include radiographic imaging across the full span of spatial resolutions in addition to both energy-dispersive

and wavelength-dispersive spectroscopy in astrophysics¹⁻³, plasma physics⁴⁻⁶, synchrotron science⁷⁻¹¹, and laboratory-based x-ray spectroscopies¹². The growing centrality of imaging detectors, especially those with significant single-pixel energy resolution, has led to a steady increase in commercial products and also niche-specific research efforts.

Here, we are most interested in a particular endpoint of these efforts, the possibility of mass-production of disposable x-ray spectroscopic cameras, i.e., those where each pixel has some significant energy resolution, having good performance for 2 – 6 keV photon energies. The ready availability of such sensors would be beneficial in several of the fields mentioned above while also serving as an easy test platform for new applications and as a convenient tool in education. We are not the first to consider these issues, and recent work in this subfield has demonstrated tantalizing potential for spectroscopic cameras based on standard, consumer-grade monochrome complementary metal-oxide semiconductor (CMOS) pixel arrays,¹³⁻¹⁵ such as regularly used in security cameras and other low-end imaging applications. This prior work establishes the viability of CMOS pixel arrays as spectroscopic imaging detectors of hard x rays and explores a host of performance characteristics, including linearity, radiation-hardness, and spatial response to single-photon interactions. The use of CMOS sensors, instead of charge-coupled devices (CCDs), is motivated by their lower cost due to chip-level integration of all sensor functions and the mature state of CMOS fabrication technology, as well as their typically much higher radiation hardness¹⁶. These considerations are in some ways representative of other efforts where admittedly much more advanced and specialized CMOS sensors are making growing inroads.¹⁷

7.3 Methods, Results, and Discussion

Unlike prior work, here we investigate sensor performance below 6 keV photon energy. Our sensor platform design is driven by the goals of: (1) achieving a high saturation count rate, (2) generating single-photon spectra in real time, (3) ease of operation for new wavelength-dispersive spectrometer development in the laboratory setting¹⁸ and (4) developing simple sensor exchange to make the camera viable as a disposable detector for use in plasma physics

experiments where experimental diagnostics are exposed to large electromagnetic pulses and to hazards from shrapnel from the laser-target interaction.

We consequently avoid commercial camera bodies and sensor evaluation boards, instead using a mass-produced CMOS sensor that can be easily and inexpensively replaced if damaged, a general-purpose single-board computer (SBC) having fast and flexible GPI/O capability as the principal hardware component, and a custom sensor board that has been designed in-house and fabricated by a rapid-prototyping printed circuit board service. To be specific, the sensor is an Aptina MT9M001 monochrome CMOS device with 1280 x 1024 resolution and a pixel size of 5.2 x 5.2 m². The sensor was chosen primarily because of its high near-infrared sensitivity, which indicates a relatively thick active layer. Before the chip's installation its protective glass cover was removed, as it strongly absorbs x rays. The SBC is similarly a mass-produced component (BeagleBone Black SBC, Texas Instruments). The SBC is based on the AM3358 system on a chip, which contains an ARM Cortex A8 processor and a PRU-ICSS (Programmable Real-Time Unit Subsystem and Industrial Communication SubSystem) subsystem with two Programmable Realtime Unit (PRU) coprocessors. The SBC's software interface to the sensor board consists of two PRU programs (implemented in PRU assembler) that perform the readout and communicate with a Linux user space program (implemented in C) that concurrently processes the resulting data stream (see Fig. 1). The PRUs operate at 200 million instructions per second (MIPS) and are configured for single-clock access to the GPI/O pins on the SBC that interface with the sensor PCB. This is sufficient for readout at 30 frames per second (fps), near the MT9M001's maximum data rate. Our current implementation suffers from a memory bandwidth bottleneck that restricts frame rate to 10 fps, but this limitation can be removed by improving the PRU Linux kernel driver's allocation and management of the ARM/PRU DDR buffer so that it exploits the ARM core's CPU cache.

Figure 7.1: Block diagram of the CMOS camera design.

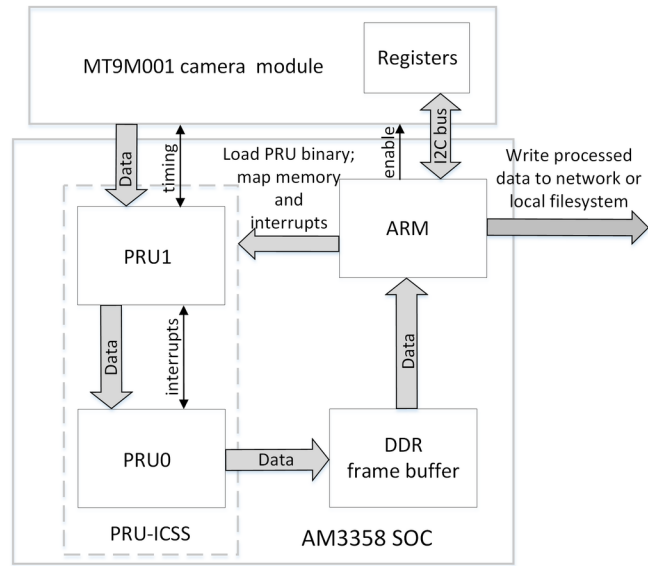
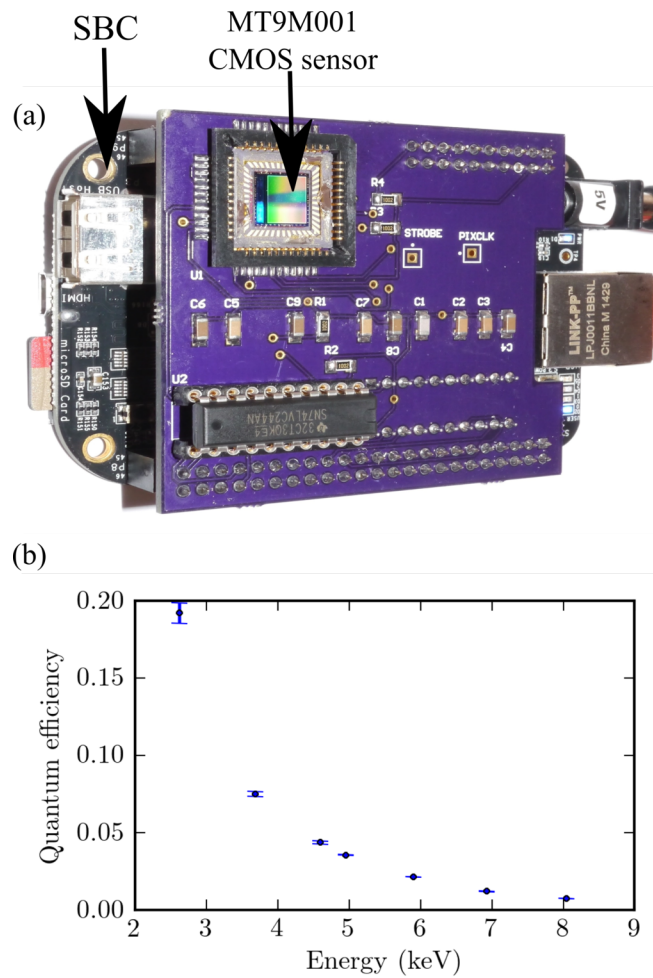


Figure 7.2: (a) An image of the camera, and (b) the camera's quantum efficiency in single-photon counting mode as a function of x-ray photon energy, as established by comparison with a commercial Si drift detector. The glass cover of the CMOS sensor has been removed to allow direct x-ray detection.



Multiple steps in processing are all performed on the SBC, and processed data is stored on the SBC's SD card before transfer to the control workstation. An exposure sequence accumulates the sum of all individual frames as a single image. Additionally, a spectrum is generated by binning the number of pixels per ADC channel. The finest energy resolution requires operating the sensor in the low-intensity single photon counting (SPC) regime where the mean period between photons incident on a given pixel is significantly larger than the frame time. Only x-ray events for which the entire charge cloud is concentrated in a single pixel are incorporated into the spectrum; this filtering step, which we refer to as cluster rejection, is well-established as necessary for optimal performance in pixel detectors used for SPC spectroscopy^{13, 19}.

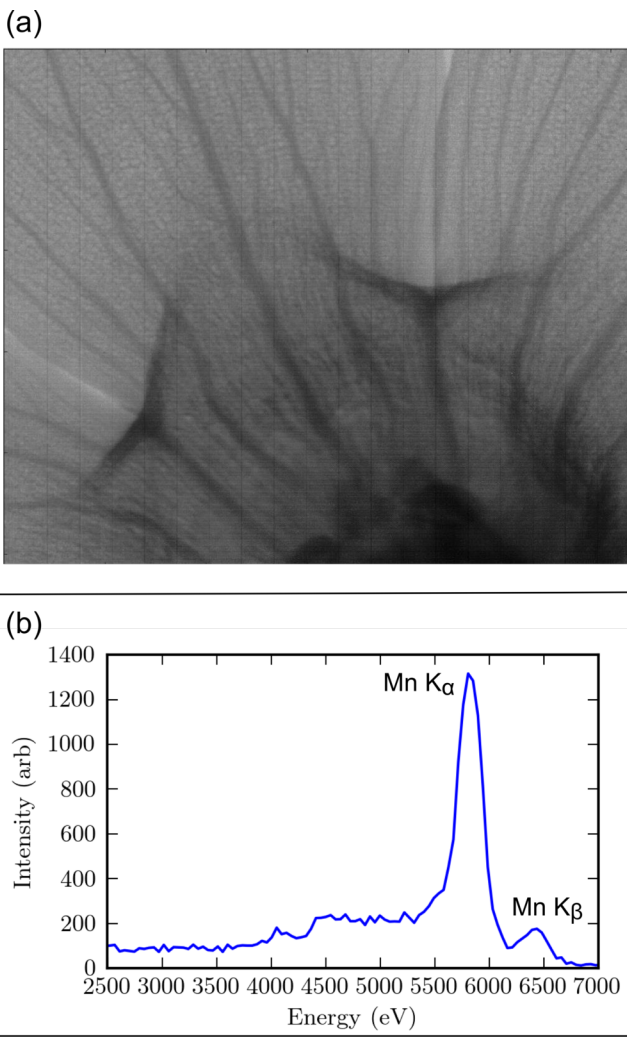
In cluster-rejection mode the sensor's saturation rate is 100,000 photons per second, but this can improved ~3-fold by resolving the aforementioned memory bottleneck. The quantum efficiency (QE) of the detector was characterized by measurement of the K -shell fluorescence spectra of chlorine, calcium, and several transition metals. This was done using a low-power laboratory x-ray tube source to excite $1s$ core holes of these elements in various solid samples. The intensity of resulting K_{α} and K_{β} emission registered by the detector was referenced to that recorded at the same position by a commercial Si drift detector (Amptek XR-100SDD) having known QE; results are presented in Fig. 2. Due to the small active layer thickness of the CMOS sensor, its quantum efficiency rapidly decreases from 19% at 2.6 keV (Cl K_{α} emission) to ~1% at 8.0 keV (Cu K_{α} emission). For imaging applications, such as use as a position-sensitive detector in wavelength-dispersive spectroscopy, it is clear that higher QE can be obtained by cluster identification, i.e., including information from events with some multipixel character. Our initial experience suggests a 50% increase in detected photon rate, but this requires further investigation. We expect that the QE will decrease below the Si K -edge because of the sudden increase in penetration length compared to the active layer thickness, but that some utility will remain below 1.5 keV. The present camera design is being modified for easier vacuum compatibility and the above issue will be investigated.

We now present detector performance in two representative applications. The radiograph

in Fig. 3 (a) demonstrates the sensor's use as an imaging detector, while Fig. 3 (b) presents a spectrum of Mn K -shell emission. No dark-field corrections are used here: the dark counts are negligible in this bin range. The FWHM of the sensor's energy response function at Mn K_{α} is 280 eV, approximately two times as large as in Fano noise-limited x-ray CCDs but still sufficiently small for the Mn K_{α} and K_{β} emission peaks to be resolved. The resolution generally scales as \sqrt{E} , where E is photon energy, for example showing 190 eV resolution at Cl K_{α} and 330 eV at Cu K_{α} . The spectrum's background below the Mn K_{α} peak energy is due to incomplete collection of charge from photon events, even after filtering for single-pixel events.

The camera's good QE below 4 keV suggests that few-keV x ray spectroscopy, whether in direct detection or as the position sensitive detector in a wavelength-dispersive instrument⁹⁻¹¹, would be a particularly favorable venue. In this regime, the smaller pixel dimension of CMOS sensors similar to the MT9M001 is a significant advantage relative to conventional x-ray CCDs, as it enables the combination of short working distance, high collection solid angle, and high energy resolution.^{10, 20-22} Additionally, such CMOS sensors' much smaller (1% or under) cost, while not in itself a technical innovation, makes them promising candidates for disposable direct-detection spectrometers in laser plasma experiments, for high-resolution radiography in educational (instructional) settings, , and for versatile coverage of special scattering angles in synchrotron studies.

Figure 7.3: (a) Radiograph of a flower petal. The grayscale is a representation of raw incident intensity. Improved spatial resolution would be achieved by selection of single-pixel events¹⁴. (b) X-ray emission spectrum of a Mn metal foil excited by a low-power laboratory x-ray tube source. The spectrum is based only on nominally single-pixel events.



7.4 Conclusions

We have reported the development of a flexible and surprisingly effective x-ray camera platform composed of standard commercial components merged with custom electronics that can be readily ordered from commercial prototyping services. The observed performance suggests an interesting range of future applications at photon energies of a few keV. This includes two aggressive possibilities: (1) large-area spectroscopic detectors formed by multiplexing large numbers of our cameras to reach net spectroscopic count rates useful for studies at the highest-intensity synchrotron beamlines or at x-ray free electron lasers, and (2) disposable detectors for use in the EMP-rich environments of laser plasma experiments.

7.5 Acknowledgments

: This work was supported by the U.S. Department of Energy, Basic Energy Sciences under Grant No. DE-FG02-09ER16106 and also by the Office of Science, Fusion Energy Sciences and the National Nuclear Security Administration thought Grant No. DE-SC0008580. We thank Bryan Venema for assistance with board assembly and for many useful discussions.

7.6 References

1. K. Koyama, et al., Publications of the Astronomical Society of Japan **59** (sp1), S23-S33 (2007).
2. P. Lechner, R. Hartmann, P. Holl, G. Lutz, N. Meidinger, R. H. Richter, H. Soltau and L. Strder, Nuclear Instruments and Methods in Physics Research Section A: Accelerators, Spectrometers, Detectors and Associated Equipment **509** (1–3), 302-314 (2003).
3. A. Stefanescu, et al., Nuclear Instruments and Methods in Physics Research Section A: Accelerators, Spectrometers, Detectors and Associated Equipment **624** (2), 533-539 (2010).
4. S. R. Nagel, et al., Review of Scientific Instruments **83** (10), 10E116 (2012).
5. G. R. Plateau, et al., Physical Review Letters **109** (6), 064802 (2012).
6. E. J. Gamboa, C. M. Huntington, M. R. Trantham, P. A. Keiter, R. P. Drake, D.

S. Montgomery, J. F. Benage and S. A. Letzring, Review of Scientific Instruments **83** (10), 10E108 (2012).

7. I. Ordavo, et al., Nuclear Instruments and Methods in Physics Research Section A: Accelerators, Spectrometers, Detectors and Associated Equipment **654** (1), 250-257 (2011).

8. M. Stampanoni, G. Borchert, P. Wyss, R. Abela, B. Patterson, S. Hunt, D. Vermeulen and P. Regsegger, Nuclear Instruments and Methods in Physics Research Section A: Accelerators, Spectrometers, Detectors and Associated Equipment **491** (1–2), 291-301 (2002).

9. S. Huotari, F. Albergamo, G. Vank, R. Verbeni and G. Monaco, Review of Scientific Instruments **77** (5), 053102 (2006).

10. S. Huotari, G. Vanko, F. Albergamo, C. Ponchut, H. Graafsma, C. Henriet, R. Verbeni and G. Monaco, Journal of Synchrotron Radiation **12** (4), 467-472 (2005).

11. M. Kavi, M. Budnar, A. Mhleisen, F. Gasser, M. itnik, K. Buar and R. Bohinc, Review of Scientific Instruments **83** (3), 033113 (2012).

12. J. Hoszowska, J. C. Dousse, J. Kern and C. Rhme, Nuclear Instruments and Methods in Physics Research Section A: Accelerators, Spectrometers, Detectors and Associated Equipment **376** (1), 129-138 (1996).

13. L. Servoli, D. Biagetti, D. Passeri and E. S. Gattuso, Journal of Instrumentation **5** (07), P07003 (2010).

14. F. Nachtrab, T. Hofmann, M. Firsching, N. Uhlmann and R. Hanke, Nuclear Science Symposium Conference Record (NSS/MIC), 2009 IEEE, pp. 1636-1639.

15. D. W. Lane, Nuclear Instruments and Methods in Physics Research Section B: Beam Interactions with Materials and Atoms **284**, 29-32 (2012).

16. K. Abe, et al., Nuclear Instruments and Methods in Physics Research Section A: Accelerators, Spectrometers, Detectors and Associated Equipment **400** (2), 287-343 (1997).

17. A. D. Falcone, D. N. Burrows, Y. Bai, M. Farris, R. Cook and S. Bongiorno, Optical Engineering and Applications **6686**, pp. 668602-668606.

18. G. Seidler, D. Mortensen, A. Remesnik, J. Pacold, N. Ball, N. Barry, M. Styczinski

and O. Hoidn, Review of Scientific Instruments **85** (11), 113906 (2014).

19. B. R. Maddox, H. S. Park, B. A. Remington and M. McKernan, Review of Scientific Instruments **79** (10), 10E924 (2008).

20. J. I. Pacold, et al., Journal of Synchrotron Radiation **19** (2), 245-251 (2012).

21. B. A. Mattern, G. T. Seidler, M. Haave, J. I. Pacold, R. A. Gordon, J. Planillo, J. Quintana and B. Rusthoven, Review of Scientific Instruments **83** (2), 023901 (2012).

22. B. Dickinson, G. T. Seidler, Z. W. Webb, J. A. Bradley, K. P. Nagle, S. M. Heald, R. A. Gordon and I. M. Chou, Review of Scientific Instruments **79** (12), 123112 (2008).

Chapter 8

A COLOR X-RAY CAMERA FOR 2 – 6 KEV USING A MASS-PRODUCED CMOS SENSOR

Oliver R. Hoidn¹, William M. Holden¹, and Gerald T. Seidler^{1,*}

¹Physics Department, University of Washington, Seattle WA 98195-1560

(*) seidler@uw.edu

8.1 *Abstract*

We report here the development of an x-ray camera for 2 – 6 keV photons using mass-produced sensors and commercial control electronics. This instrument has several favorable characteristics for advanced x-ray spectroscopy studies in the laboratory, at synchrotron light sources, at x-ray free electron lasers, or using pulsed x-ray sources such as for laser plasma physics research. These characteristics include fine position and energy resolution for individual photon events; high saturation rates; easy user maintenance for damaged sensors; and software for real-time processing. We present results that evaluate this camera for use as an alternative to traditional energy-dispersive solid-state detectors, such as silicon drift detectors, and also illustrate its use in a dispersive x-ray emission spectrometer that has recently been reported elsewhere (Holden, et al., 2017).

8.2 *Introduction*

The capabilities of a variety of x-ray techniques at the synchrotron, x-ray free electron laser (XFEL) and university-scale laboratory are heavily dependent on the characteristics of the x-ray detectors with which they are implemented. One technological regime of interest is that of pixel area detectors combining spectroscopic and spatial resolution with features such

as high readout rate, large collection solid angle, and hardness to ionizing radiation and electromagnetic pulses (EMPs). The advent of time-resolved spectroscopy with pulsed photon sources, such as x-ray free electron lasers (XFELs), where it is often necessary to collect large numbers of signal photons quasi-instantaneously and with repetition rates exceeding 100 Hz, has greatly expanded the need for this class of detectors. Similar needs are also present in laser-plasma physics, where entire spectra for fluorescence, x-ray band thermal emission, or inelastic scattering must often be collected in truly single-pulse experiments.

While there is an impressive effort aimed at either improvement of existing state-of-the-art technology or *de novo* development of new ideas for truly advanced high-performance detectors, there is another route that requires consideration. Highly mass-produced, commercial multipixel sensors intended for primary use at optical wavelengths are, by the standards of x-ray science, already stunningly advanced sensors. For example, recent advances in the performance of mass-produced CMOS image sensors, including readout rates above 200 Mpix/second and optical-wavelength quantum efficiencies exceeding 80%, significantly increases their potential for scientific applications. The direct application of such sensors to the x-ray regime is limited mainly by the fact that their small pixel thicknesses lead to greatly decreased quantum efficiency for hard x-rays. That being said, the use of CMOS image sensors in the x-ray regime has been explored in prior literature, which has established them as viable spectroscopic imaging detectors having a favorable combination of low cost (a consequence of chip-level integration of all sensor functions), high framerates, and improved radiation hardness relative to comparable charge coupled devices (CCDs). ¹⁻⁴. By ‘spectroscopic’, we mean that the camera output contains sufficient information for determination of both the energy and position of a photoabsorbed x-ray—such devices are often referred to as ‘color x-ray cameras’.

In a prior publication we presented an x-ray camera platform for the 2-6 keV photon energy range based on a legacy CMOS image sensor, the Aptina MT9M001. Here, we introduce a new camera that incorporates a modern back-illuminated CMOS sensor with significantly improved readout rates and finer spectral and positional resolution compared

to the previous model. We find an energy resolution of \sim 150 eV at 2 keV with saturation rates above 10^6 /s at \sim 80 Hz frame rate. These spectroscopic benefits are complemented by a spatial resolution of 2.9 m and real-time processing of all results, but are constrained by a \sim 65% quantum efficiency at 2 keV that decreases to below 20% at 5 keV.

This manuscript continues as follows. First, in section II, we describe the commercial hardware, and its modification used in the present instruments, and also the new software package that has been developed to support real-time spectral analysis or real-time energy-windowed imaging. A key point here is that it is not only the sensor, but also the entire camera read-out system that is commercially available because of the high demand for extreme low-light sensitivity for, e.g., amateur astronomy. Next, in section III, we present results and discussion, demonstrating the cluster-binning methods and also both energy-dispersive and photon-counting modes for the camera. This includes representative data from a wavelength-dispersive spectrometer whose design has recently been described elsewhere.⁵ Finally, in section IV we conclude and provide future directions.

8.3 II. Experimental

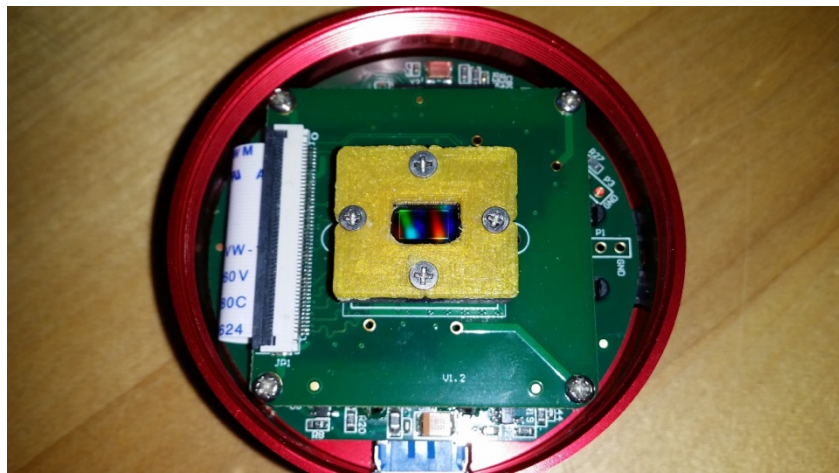
8.3.1 II.A. Hardware

The hardware consists of a commercial amateur astronomy camera (ZWO Company) based on the Sony IMX290, a back-illuminated CMOS image sensor with a rolling shutter, pixel pitch of 2.9-m, pixel grid of 19361096, and maximum framerate of 170 fps. The sensor features high sensitivity and dynamic range, with a 12-bit A/D converter and readout noise of 1e- at maximum analog gain. The choice of vendor and model was driven by the manufacturer's provision of a software API allowing straightforward configuration and access to the sensor's uncompressed video stream; notably, however, other manufacturers offer products with similar feature sets.

We have modified the camera in two ways. First, the main camera board has been reworked by removing the IMX290 sensor and replacing it with a custom IC socket (Andon

Electronics). This was done to more easily allow sensor replacement if radiation damage occurred. Second, the sensor itself has been modified by removal of the glass cover (Pacific X-Ray). A photo of the resulting camera is shown in Fig. 8.3.1. The yellow plastic part holding down the sensor is a simple clamp used to press the sensor against the socket contact pads.

Figure 8.1: Photograph of the modified camera. The original commercial product has been reworked to install an IC socket for the sensor and to remove the glass cover of the sensor.



8.3.2 II.B. Software

Charge separation generated by an x-ray photon absorbed in the active layer of a sensor pixel results in a signal with expectation value proportional to the photon's energy. In the simplest case, wherein the entire charge cloud from an x-ray absorption event is concentrated in a single pixel, the detecting pixel has intrinsic sensitivity to the energy of the incident x-ray photon. In the majority of events, however, the charge cloud spreads over a cluster of several adjacent pixels.^{3, 4} We have found that, in order to optimize the camera's quantum efficiency (QE) and spectroscopic sensitivity, it is essential to use this prior information to recover the energy and position of each detected photon on an event-by-event basis. To do this we perform a “breadth-first” search⁶ of every frame to identify sets of connected pixels

with ADC values above a user-specified signal threshold. For each cluster thus identified, the signal is summed over all member pixels and the event's position is inferred from the cluster's center of mass. This technique is similar to event-reconstruction algorithms used for the same purpose in prior literature, with the difference that we place no constraint on the size and shape of signal clusters³. The sensor's low noise floor (under 1 e- per pixel) (*cite datasheet. Can't find anything about the citation format for datasheets under the AIP style guide*) allows the use of an aggressively low threshold level, resulting in a high level of signal.

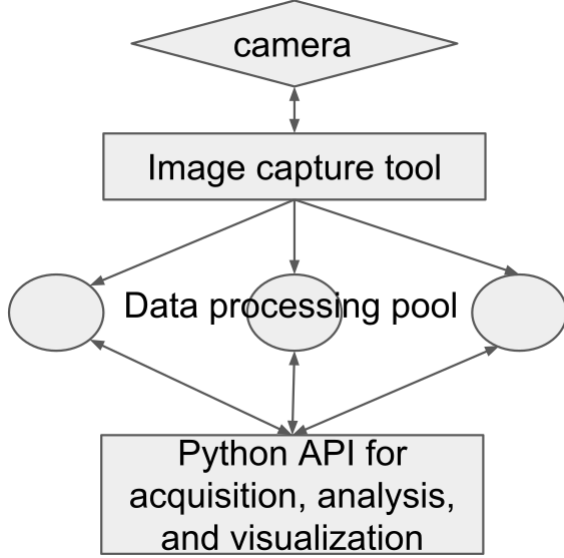
To implement the above analysis while avoiding the prohibitively large quantity of disk storage that offline processing demands, we developed a real-time data processing pipeline; the general framework for this pipeline is shown in Fig. 8.3.2. It consists of a collection of several software components communicating with one another over ZeroMQ sockets. First, a customized version of the open source image capture program oaCapture controls the camera's readout, allowing the user to configure the camera's gain and per-frame exposure time. Event reconstruction, which requires the computational throughput of multiple CPU cores, is done by a pool of worker processes collecting frames from the capture application in round-robin fashion. The resulting filtered frames from this parallel pipeline are aggregated on a sink node that communicates with an API component that, in turn, provides users with high-level functions for acquiring and visualizing pre-processed camera data.

8.4 III. Results and Discussion

In this section we address four aspects of the camera operation and performance: the cluster algorithm, energy dispersive operation, quantum efficiency, and finally single-photon counting mode for spectroscopically-constrained imaging. First, a magnified view of a small region of a captured image is presented in Fig. 8.4, where single-photon signal clusters are readily identifiable. The distribution of cluster sizes is strongly skewed; the largest clusters contain more than 10 pixels, while the mean number is 2.1.

Second, when operated as a spectroscopic sensor, the camera's user-visible output is a

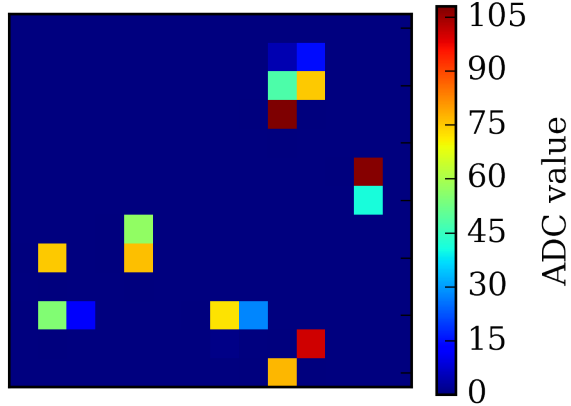
Figure 8.2: Diagram of camera data processing pipeline.



histogram, summed over all frames, of number of events binned by per-event signal. This is demonstrated in Fig. 8.4 (top panel), which shows the direct-illumination spectrum of a laboratory x-ray tube source. The dominant components of the signal are the tube's continuous bremsstrahlung spectrum and Rh L-shell emission from the anode. Two detector artifacts are also visible. First, a peak at the energy of Si K is generated by Si fluorescence photons emitted in the sensor that propagate far enough from their originating interaction sites to be registered as separate events. Second, the escape of Si fluorescence from the absorption sites of Rh L photons creates echos of the Rh L peaks (termed escape peaks) that are downshifted by 1.74 keV, the energy of Si K. We find that the camera's energy resolution at the energy of P K is 150 eV (Fig. 8.4 bottom panel), somewhat inferior to SDD's at this energy but still sufficient for many applications.

Third, the quantum efficiency (QE) of the detector was characterized by measurement of the K-shell fluorescence spectra of several elements, using a low-power laboratory x-ray tube source to excite 1s core holes in each measured sample. The intensity of resulting K and K⁺ emission registered by the detector was referenced to that recorded at the same position by a

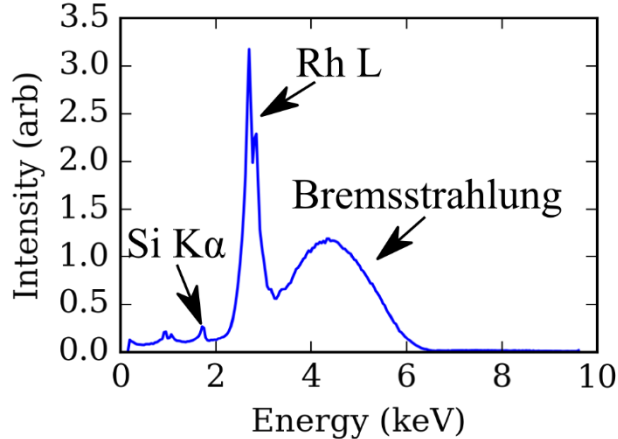
Figure 8.3: Representative cropped region of a camera frame during direct illumination by a Rh anode x-ray tube source operating at 6 kV bias voltage, with the camera detecting 2×10^6 photons/s at an 80 Hz frame rate.



commercial Si drift detector (Amptek XR-100SDD) having known QE. Results are presented in Fig. 8.4; we note a maximum QE of 60% at the energy of P K, a more than two-fold improvement over our previous camera.⁴ Under uniform illumination from Rh x-ray tube (?) at 6 kV accelerating potential, the observed count rates have only minimal deviations from linearity at count rates up to 2×10^6 photons per second 80 Hz frame rate (see Fig. 8.4) – an impressive performance that is higher than the typical saturation rate of commercial silicon drift detectors. The lower count rates for the CMOS camera compared to the SDD are a consequence of the camera’s lower quantum efficiency at higher photon energies.

Finally, the camera’s combination of high saturation count rates and small pixel dimension makes it a strong fit as a position-sensitive detector in compact dispersive x-ray emission spectrometer designs. In such an application the camera’s spectroscopic sensitivity may be employed for background rejection (i.e., for rejection of photons with energies outside a pre-specified range), thus minimizing the need for shielding from stray scatter. Holden et al. have demonstrated this advantage in a novel compact dispersive refocusing Rowland (DRR) spectrometer design with a 10 cm-Rowland circle that incorporates the camera as its

Figure 8.4: Energy dispersive spectrum from direct illumination of the camera by a Rh anode x-ray tube source operating at 6 keV bias voltage. The ADC channel at the peak of the Rh L emission contains counts. See the text for discussion.



position-sensitive detector (Fig. 8.4). The spectrometer's small dimensions, which are enabled in part by the camera's fine spatial resolution, give it a large collection efficiency which results in count rates in laboratory studies (using low-power x-ray tube sources) comparable to those at a third-generation synchrotron insertion device. The instrument has thus far been demonstrated in the university-scale laboratory and at the synchrotron; its potential use at the Linac Coherent Light Source (LCLS) is currently being investigated, especially as the sensor frame rate can likely be matched to the 120 Hz repetition rate of that XFEL.

Figure 8.5: Camera count rate as a function of incident photon intensity, controlled via current provided to an x ray tube source directly illuminating the camera (blue). We compare to the same curves for a commercial SDD with pulse shaping times optimized for count rate (orange) and energy resolution (green). The camera’s saturation count rate is a factor of approximately 10 higher than the SDD’s. The low efficiency of the camera is due to the high flux at higher photon energies, see Figures 8.4 and 8.4.

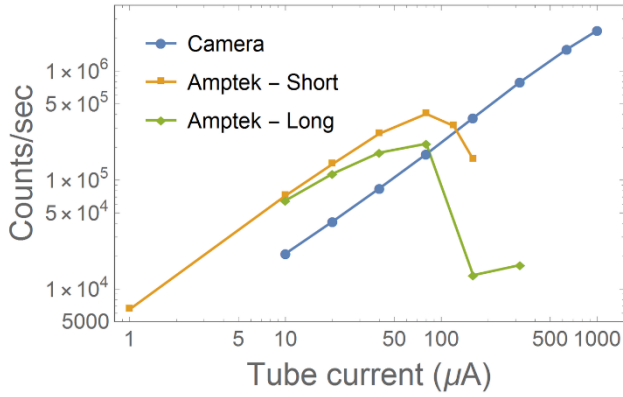


Figure 8.6: The camera’s quantum efficiency as a function of x-ray photon energy, as established by comparison with a commercial Si drift detector.

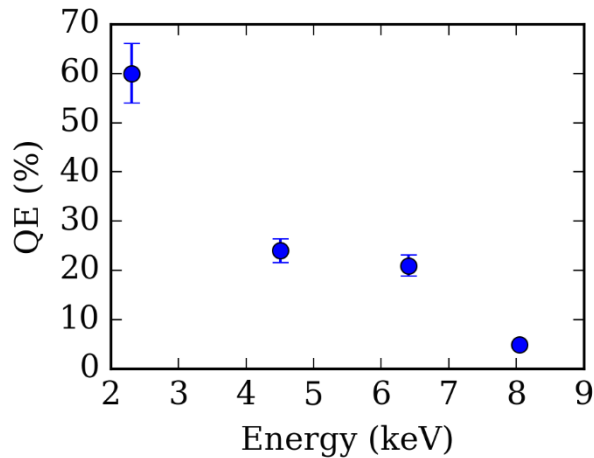
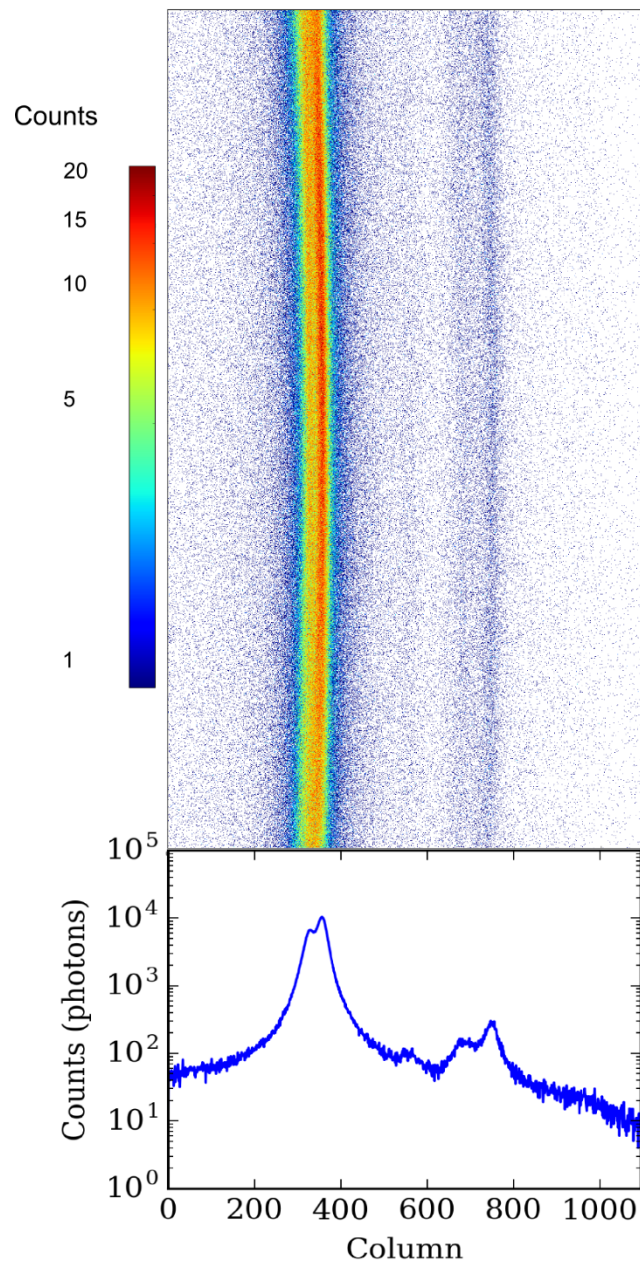


Figure 8.7: Image of the sensor's output when serving as the position-sensitive area detector in a DRR spectrometer.⁵ The signal shown is a S k alpha spectrum. In order to reduce the background level, the camera was configured to reject all events with photon energies outside of the spectrometer's bandwidth



8.5 IV. Conclusions and Future Directions

In conclusion, we have reported the development of a quite capable x-ray camera based on a mass-produced consumer product. The observed performance suggests a range of potential applications as a high-speed spectroscopic detector with fine spatial resolution and adequate quantum efficiency in the 2 - 6 keV photon energy range. Among these applications, we have demonstrated effective use of the camera as a position-sensitive detector in a novel high-performance compact dispersive spectrometer.

8.6 References

Chapter 9

REAL-TIME ANALYSIS TOOLS FOR THE LCLS

A significant drawback of current XFELs, compared to synchrotron light sources, is that they are capable of providing photons to only one endstation at a time. As a result they are vastly oversubscribed, and beamtime is granted in small allocations through highly competitive selection processes. Experimental teams therefore have strong incentives to make the most efficient possible use of beam time. Focusing on the specific case of the LCLS, the high power of the XFEL source (and its 120 Hz repetition rate) facilitates rapid completion of experiments by making very high data collection rates possible. However, fully taking advantage of high data throughput is a problem unto itself, as experiments cannot be fully scripted in advance; it is in practice necessary to make rapid evaluations based on measurement of beam conditions (which, in two-color mode, can be strongly variable), the statistical quality of incoming data, and tentative physical interpretations in the incoming data. This feedback often guides important decisions, such as beam tuning and the motion of samples and detectors.

With the goal of addressing this problem we have developed a software package for real-time analysis and visualization of data in XFEL experiments at the LCLS. The software is implemented using Photon Science Analysis (psana), the internal data analysis framework at the LCLS, and can be run in distributed fashion over hundreds of cores. (cite Damiani et al. 2016). It attempts to enable a more effective analysis workflow than currently available to LCLS users, excluding those doing specialized experiments of well-established types for which there already exist tailored software packages (such as Cheetah for serial femtosecond crystallography). (cite Barty et al).

This chapter describes a Python API that provides high-level analysis and visu-

alization functions that directly implement common analysis operations, and can serve as building blocks more complex custom ones. The API is optimized for use through the Jupyter notebook, and it leverages the rich interactive plotting features available in that environment.

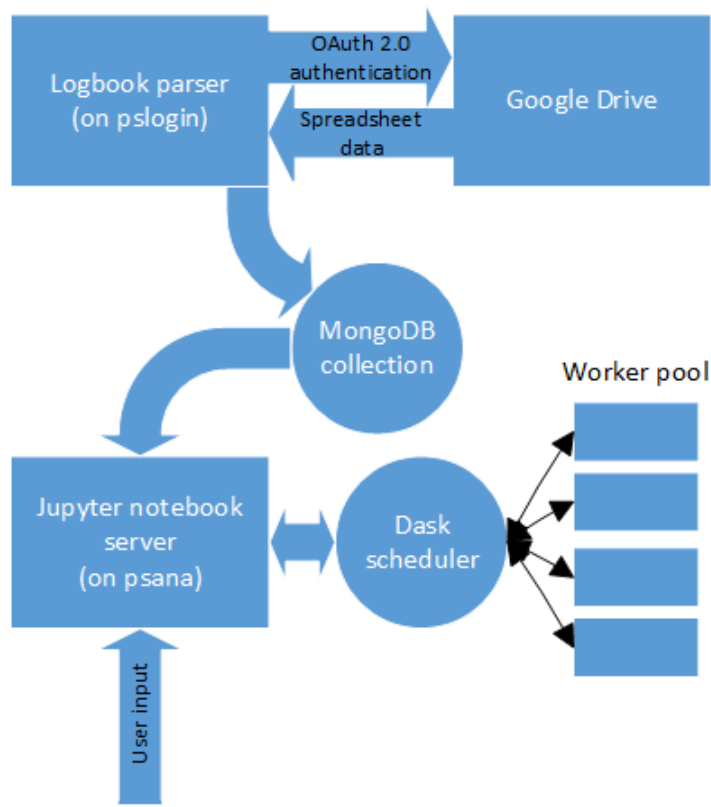
Though it will not be discussed in detail, we note the existence of a second interface to the same analysis framework, consisting of a web app that provides a more user-friendly graphical interface (in exchange for reduced flexibility). This interface was independently developed by Ryan Valenza from the Seidler group.

9.1 Integration of Logging and Analysis

The psana API associates every LCLS pulse (referred to as an event) with two integers, a run number and event number. (cite Damiani et al. 2016) A run contains a consecutive sequence of events; the maximum number of events in a run is determined by a 17 bit 360 Hz ‘fiducial’ counter that the LCLS timing system distributes to each detector. The association of run/event number combinations to LCLS pulses is in practice further constrained by endstation-specific software and instrumental details: at the Matter of Extreme Conditions beamline (MEC), for example, performing a two-dimensional sample raster involves interruptions between horizontal rows, which in turn requires the run number to be incremented at the beginning of each row.

Because the LCLS DAQ system does not allow the association of events with user-provided metadata, LCLS users must maintain separate experimental logs in which, for each run number and range of event numbers, they record information related to sample type, beam conditions, and other relevant experimental parameters. In the vast majority of cases, users’ analysis scripts directly expose psana’s data access API, requiring them to explicitly specify datasets in terms of lists of run numbers. To do this the user must manually look up and transcribe information from the experimental logbook, an operation that becomes time-consuming (and potentially error-prone) when frequently repeated, as it usually must be.

Figure 9.1: Diagram summarizing the analysis software's architecture.



In response, we've made a step to unify the workflows for experimental logging and analysis. We've defined a simple query language with which the user can construct datasets defined by matches to metadata attributes recorded in the experimental logbook. The implementation is described in Fig. 9.1; briefly, it consists of a daemon (i.e. application component) that accesses data from standard-formatted Google Drive spreadsheets tied to users' personal Google accounts. This daemon parses spreadsheet data into a graph structure associating run numbers with metadata column values and constructs datasets (i.e., sets of run numbers)

by parsing user-provided queries on those column values.

9.2 Interactive Distributed Computing

A second feature of the software is the simplified fashion in which it leverages the LCLS computing cluster. To do real-time analysis during beam runs it is typically necessary to scale one's workload over tensor hundreds of CPU cores. This is typically done with a batch processing workflow, where command lines for launching parallel analysis scripts are submitted to the LCLS's Platform Load Sharing Facility (LSF) (cites), which schedules them for execution on nodes of the cluster. Once a batch job is complete, users typically run a second (non-distributed) program to load and visualize the output data. The time that elapses between submission of a batch job and when it begins running is typically on the order 10 seconds or more, assuming an empty job queue. The separation between the steps of submitting an analysis batch job and loading and viewing its results introduces a delay as well, because the user must manually intervene at two points in the analysis pipeline. These two factors give a batch-processing-based workflow significant overhead.

Our software package offers a significant improvement in this respect: the backend of the analysis API distributes calculations over the LCLS cluster transparently, with no need for the user to submit batch jobs or otherwise steer the parallel computation in any way. To implement this we use the parallel computing library Dask (cite Rocklin). Dask consists of several components, one of which is a dynamic task scheduler optimized for computational workloads. Its valuable features, in our context, are its ability to dispatch work to a pool of worker processes in intelligent fashion (with awareness of task dependencies and data locality) and with flexibility and fault tolerance (allowing for the dynamic addition, as well as removal, of worker processes). From the point of view of interactive computation, its most important feature is that it implements the same synchronous semantics as an equivalent single-threaded program. Fig. (cite figure) illustrates the role of Dask's distributed scheduler within our analysis software's overall architecture.

9.3 API features

The last component of our package is a library of API functions for analyzing and visualizing data. These are in part tailored to MEC, the location of both our LCLS beam runs, but are for the most part generally applicable to other endstations. The API heavily leverages features of the browser-based Jupyter notebook, including interactive Javascript-based plots.

The API provides standard analysis routines for spectroscopy and X-ray powder diffraction. Miscellaneous diagnostic tools are included for, e.g., viewing the readout of area detectors (per-event or averaged over all events in a dataset) and generating histograms or scatter plots of event-by-event signal incident on arbitrary detectors. Most of these functions adopt a general functional programming style that allows the user to alter their behavior, using them as building blocks in more complex, customized applications. For instance, all analysis API calls accept, as optional arguments, user-defined functions for event rejection that take a detector datum as input and return a boolean. A more specialized example of the functions-as-arguments pattern is the histogram API call. In its most basic usage, this function takes an area detector identifier and one or more datasets as arguments, and returns an interactive figure containing histograms of per-event integrated signal on the detector. In a more sophisticated usage, the user could pass in a keyword parameter consisting of a function that, for example, integrates signal over a subregion of the area detector’s 2D data array, instead of its entirety.

Our software package is under continued development and will be used in future LCLS experiments of the Seidler group. We plan to also shortly make it available to other LCLS users.

Figure 9.2: Jupyter notebook screen capture demonstrating a simple example of the API’s usage. First a dataset is defined via a query matching all run numbers between 200 and 210 for which the recorded value for the XFEL transmission is 0.11. Two metadata attributes of the resulting dataset are then printed. In the last line of input, we call the API function `datashow.show`, which takes a list of datasets (in this case containing the single defined dataset) and an area detector identifier (in this case ‘si’, the identifier for a downstream silicon spectrometer monitoring the XFEL spectrum) and displays the average of detector readouts over all events. This data was collected at LCLS beam run LK20.

```
In [13]: from dataaccess.nbfuctions import get_query_dataset as query
from dataaccess.datashow import show

ds = query('runs 200 210 transmission 0.11');
print [(attr, ds.get_attribute(attr)) for attr in ['transmission', 'runs']]

show([ds], 'si');

[('transmission', 0.11), ('runs', [206])]
```

